Motion Correction in Compressively Sampled Dynamic MR Imaging

By

Muhammad Bilal

Reg. No. 50-FET/PHDEE/S12

A dissertation submitted to I.I.U. in partial fulfillment of the requirements for the degree of

DOCTOR OF PHILOSOPHY

Department of Electrical Engineering
Faculty of Engineering and Technology
INTERNATIONAL ISLAMIC UNIVERSITY
ISLAMABAD
2019

DEDICATED TO

My Teachers

and Family

CERTIFICATE OF APPROVAL

Title of Thesis: Motion Correction in Compressively Sampled Dynamic MR Imaging

Name of Student: Muhammad Bilal

Registration No: 50-FET/PHDEE/S12

Accepted by the Department of Electrical Engineering, Faculty of Engineering and Technology, International Islamic University, Islamabad, in partial fulfillment of the requirements for the Doctor of Philosophy degree in Electronic Engineering.

Prof Dr. Muhammad Amir _____
Dean FET IIUI

Dr. Suheel Abdullah Malik _____
Associate Professor, Chairman
DEE FET IIUI

Prof. Dr. Aqdas Naveed Malik (Internal Examiner) _____
V.P. Higher Studies & Reseach, IIUI.

Prof. Dr. Tanveer Ahmed Cheema (External Examiner - I) _____
Chairman School of Engineering & Applied Sciences
Isra University, Islamabad.

Dr. Muhammad Usman (External Examiner -II) _____
Senior Director
NESCOM, Islamabad.

Dr. Jawad Ali Shah (Supervisor) _____
Department of Electrical Engineering
International Islamic University, Islamabad.

Prof. Dr. Ijaz Mansoor Qureshi (Co-Supervisor) _____
Department of Electrical Engineering
Air University, Islamabad

19th April, 2019

Abstract

Magnetic Resonance Imaging (MRI) is a non-invasive but slow imaging modality for studying different anatomical and functional aspects of human body. However, it is difficult for a patient to remain motionless during the slow MR acquisition process. The subject motion is one of the main hurdles in MRI due to the fact that the respiratory motion is faster compared to acquisition process resulting in ghosted and blurry recovered images. Cardiac and abdominal MR imaging is mostly affected by respiratory motion. In this thesis, compressive sensing (CS) based new approaches are developed to tackle the respiratory motion in cardiac and abdominal MRI examination.

The cost function used by CS based MR recovery algorithms include l_1-norm penalty to exploit the transformed domain sparsity of the acquired MR data. The initial part of dissertation presents a comparison of surrogate functions used to approximate the l_1-norm penalty. The experimental work shows that the hyperbolic tangent based function outperforms its competing function in the recovery of static MR images for different acceleration rates and various Gaussian noise levels. Based on these findings, an iterative thresholding algorithm utilizing hyperbolic tangent based l_1-norm approximation is developed to recover free breathing dynamic MR images from sub-sampled *k*-space data. A block matching algorithm, known as Adaptive Rood Pattern Search (ARPS) is then used to estimate and correct respiratory motion among the recovered images.

In the next part, an adaptive thresholding parameter utilizing the MR data statistics is derived and used in wavelet domain shrinkage to recover both static and dynamic MR images. A novel iterative shrinkage thresholding (IST) algorithm based on the derived

adaptive parameter is also proposed. Results show that the MR recovery using adaptive threshold is more effective in the presence of motion as compared to fixed threshold value.

The final part presents the reduction of motion artifacts in the recovery of under-sampled abdominal and liver dynamic contrast enhanced (DCE) MR images using data binning and low-rank plus sparse (L+S) decomposition. In the data binning, radial k-space data is acquired continuously using golden-angle radial sampling pattern and grouped into various motion states or bins. The respiratory signal for binning is extracted directly from radially acquired *k*-space data. A compressed sensing (CS)-based L+S matrix decomposition model is then used to reconstruct good quality DCE MR images. The proposed techniques are validated using simulated and clinical MRI data.

List of Publications

[1]. **Bilal, M**., Ahmed, A.H., Shah, J.A., Kadir, K. and Ayob, M.Z., 2017, September. Comparison of L 1-norm surrogate functions used for the recovery of MR images. In Engineering Technology and Technopreneurship (ICE2T) Malaysia, 2017 International Conference on (pp. 1-4). IEEE.

[2]. **Bilal, M**., Shah, J.A., Qureshi, I.M. and Kadir, K., 2018. Respiratory Motion Correction for Compressively Sampled Free Breathing Cardiac MRI Using Smooth-Norm Approximation. International journal of biomedical imaging, 2018.

[3]. **Bilal, M**., Shah, J.A., Qureshi, I.M. and Ahmed, A.H., 2018. Motion Adaptive Wavelet Thresholding for Recovery of Compressively Sampled Static and Dynamic MR Images. Applied Magnetic Resonance, pp.1-15.

[4]. **Bilal, M.,** Anis, H., Khan, N., Qureshi, I., Shah, J. and Kadir, K.A., 2019. Reduction of Motion Artifacts in the Recovery of Under-sampled DCE MR Images Using Data Binning and L. BioMed Research International, 2019.

[5]. Ikram, S.; Shah, J.A.; Zubair, S.; Qureshi, I.M.; **Bilal, M**. Improved Reconstruction of MR Scanned Images by Using a Dictionary Learning Scheme. Sensors 2019, 19, 1918.

The research work presented in this dissertation is based on the first four publications.

Acknowledgments

In the name of Allah (SubhanahuWaTa'ala), who is the most gracious and the merciful. I would like to thank Allah for giving me strength and patience to complete this research work. Peace and blessings of Allah be upon His last Prophet Muhammad (Sallulah-o-Alaihihe-Wassalam) and all his Sahaba (Razi-Allah-o-Anhu) who dedicated their lives for Dawah and spread of Knowledge.

I am truly grateful to my supervisor Dr. Jawad Ali Shah, whose inspiration, ideas and efforts make it possible for me to complete my higher studies. He has been a role model for me and many others in teaching, research and other aspects of life. I would also like to thank my co supervisor Prof. Dr. Ijaz Mansoor Qurshi for his support during my research work.

I offer my sincere thanks to my colleagues Dr. Abdul Haseeb Ahmed, Dr. Muhmmad Waseem Khan, Engr. Haris Anees, Engr, Engr shahid Ikram, Muhammad Muzzammil, Engr. Rehan and Engr. Sharjeel Abid Butt for their never ending support and for their useful discussions during last few years. I would like to acknowledge the support of International Islamic University Islamabad Pakistan for providing me full fee waiver during the PhD studies. I would like to acknowledge and express my gratitude to British Malaysian Institute (BMI) University of Kualalumpur Malaysia for their financial support to conduct my research.

I am really grateful to my father, mother, sisters and brothers for their love and support throughout my life. I am also very thankful to my wife for her patience, encouragement and prayers during every stage of my PhD degree. Finally, I am thankful to my kids, whose innocent gestures were source of inspiration for me.

(Muhammad Bilal)

Table of Contents

List of Figures

List of Tables

List of Abbreviations

AP Anterior Posterior

ARPS Adaptive Root Pattern Search

CT Computed Tomography

CA Contrast Agent

CS Compressed (or compressive) Sensing (or sampling)

dB Decibel

db4 Daubechies-4

DCE Dynamic Contrast Enhancement

DCT Discrete Cosine Transform

DFT Discrete Fourier Transform

DWT Discrete Wavelet Transform

FFT Fast Fourier Transform

FH Foot Head

FID Free Induction Decay

FOV Field of View

FOCUSS FOCal Underdetermined System Solver

fMRI Functional Magnetic Resonance Imaging

IFFT Inverse Fast Fourier Transform

ISNR Improved-Signal-to-Noise Ratio

IST Iterative Shrinkage Thresholding

LMS Least-mean-square

LR Low Right

RF Radio Frequency

RIP Restricted Isometry Property

SSF Separable Surrogate Functional

SSIM Structural Similarity Index

SNR Signal-to-Noise Ratio

MAP Maximum a posteriori

MEMC Motion Estimation and Motion Correction

MRI Magnetic Resonance Imaging

MSE Mean Square Error

PCD Parallel Coordinate Descent

PET Positron Emission Tomography

pdf Probability density function

POCS Projection Onto Convex Set

PSNR Peak Signal-to-Noise Ratio

ROI Region of Interst

RPCA Robust Principle Component Analysis

TV Total Variation

ZF Zero-Filling

Chapter 1

Introduction

Magnetic resonance imaging (MRI) is a non-invasive and non-ionizing medical imaging technique to provide human diagnostic images. Provision of multi-planar and high contrast images with excellent tissue resolution makes MRI a better choice than X-rays and computed tomography (CT). However, MRI is a slow imaging technique resulting in lengthy examination time as compared to other imaging modalities. In the claustrophobic environment of MR scanner, for a patient or even for a healthy volunteer, it is difficult to remain stationary during MRI examination. Long scanning time makes MRI sensitive to motion and requires a compromise between spatial and temporal resolution in dynamic MR imaging.

In Cardiac MRI, a single slice of heart at different cardiac phases is repeatedly imaged through many cardiac cycles. To generate a good quality CINE i.e. a short movie of all cardiac phases of a single slice, data acquired from all cardiac cycles must be combined. However, in the presence of breathing motion, this combination produces blur and ghosting effects because data acquired for a specific cardiac phase during a heart cycle at distinct respiratory position produces data inconsistency.

Dynamic contrast enhancement (DCE) MRI provides a measurement of T_1 changes in tissues over time after the intravenous bolus of contrast agent (CA) which produces strong intensity variations over time. The DCE technique relies on the monitoring of images

during uptake and wash out of contrast agent. The complete process of DCE-MRI (uptake and washout of CA) takes several minutes and it is difficult for a patient to remain still during the scan process. In free breathing, the data acquired at distinct respiratory states produce inter-frame misalignment and the resulted recovered images are contaminated with motion artifacts. The continuous CA intensity change is another challenge along with respiratory motion in free breathing DCE MRI. To generate MR images with a reasonable accuracy, intensity variation and respiratory motion must be distinguished and separated from each other before applying any image reconstruction method.

Since its invention, MRI has substantially improved in acquisition speed and image quality. To speed up the imaging process, faster data collection was implemented by improved hardware, faster pulse sequences and efficient sampling trajectories. Currently, basic physical and physiological constraints limit the faster data collection. Due to this limit, researchers worked out methods that produce images with good quality from reduced amount of sampled data. One method is a parallel imaging with multiple receiver coils that provide complementary information about the imaging object [1]. Compressive sensing [2, 3] is another technique used in recent past to speed up the MR data acquisition process. It recovers the MR images from less number of acquired samples using inherent redundancy or sparsity of MR data [4-6]. Sampling below the Nyquist rate introduces random noise like artifacts in the recovered images. These artifacts become more severe if the accelerated scanning process performed in the presence of different body motions including involuntary movements, cardiac and respiratory motion, gastrointestinal peristalsis, vessel pulsation, and blood and CSF flow. These motions are normally observed during the imaging of brain, heart, abdominal and liver etc. Application of CS to the biomedical MR

imaging in the presence of different types of motions require extra steps in the recovery algorithms. The recovered image quality can be improved by incorporating some prior information related to the dynamics of the underlying data. Moreover, better results can be obtained by using some adaptive parameters that changes their values according to the dynamics of imaging parts.

Algorithms that tackle respiratory motion by incorporating motion related priors with adaptive parameters in the reconstruction process for cardiac CINE and abdominal DCE MRI are presented only in this thesis.

1.1 Dissertation contribution

The primary objective of this thesis is to tackle respiratory motion in cardiac CINE and abdominal DCE MR imaging. Motion based efficient reconstruction algorithms are developed to produce images with reasonable accuracy. The proposed recovery algorithms are based on the iterative shrinkage methods that are well suited for large dimensional signals. These algorithms accomplish sparse MR image recovery by solving $l_1 - l_2$ norm mixed optimization problem. The proposed methods have been analyzed using recovered images qualitatively and in terms of different assessment parameters such as Peak signal to noise ratio (PSNR), Structural similarity index measurement (SSIM), correlation and sharpness index (SI). Contributions of this dissertation can be summarized as follows

1. The l_1-norm is not differentiable everywhere. Initially in this thesis, two continuous surrogate functions that approximate the l_1-norm penalty are compared, and it is concluded that due to better approximation at the origin,

multi-parameter hyperbolic tangent function is better for static and dynamic MR images as compared to other function normally used in the literature.

2. A novel framework for the recovery of highly under sampled free breathing cardiac MR images. A two-step approach is adopted for the reconstruction of dynamic MR images. In the first step, free breathing cardiac phases without motion estimation are recovered from under-sampled k-space data. Next, inter-frame motion between the reconstructed cardiac phases is calculated using ARPS to improve the image estimates iteratively. Multi-parameter hyperbolic tangent function as an approximation of the l_1-norm penalty is used in the gradient descent algorithm to recover dynamic MR images. The adjustable parameters of the l_1-norm approximation provide an extra benefit, as it can be adjusted to reflect the changing statistics of dynamic MR images.
3. During the solution of $l_1 - l_2$ norm mixed optimization problem, there is a tradeoff parameter that defines the share of l_1 and l_2 norms in the solution. This parameter is normally fixed valued and selected empirically. The next contribution in this dissertation is the development of new iterative shrinkage thresholding algorithm and the derivation of an adaptive threshold parameter using MAP estimator. The statistics of under-sampling noise and MR image in the wavelet domain is used to make the parameter adaptive. The proposed algorithm adaptively updates the threshold value, used in shrinkage function, for the estimation of MR images. Results show that the MR recovery using adaptive threshold is more effective in the presence of motion as compared to fixed threshold value.

4. Respiratory motion in abdominal and liver DCE MRI is dealt in the next section of the thesis. To distinguish intensity changes from respiratory motion in DCE MRI, data binning process is used as a preprocessing method for CS based L+S decomposition method. For data binning, motion detection and extraction of a breathing signal is performed by exploiting the self-navigation property of golden angle radial sampling. A CS-based L+S decomposition algorithm is then used for each bin to recover images free from motion and under-sampling artifacts. As compared to the CS-based conventional L+S (CL+S) decomposition method, the pre-processed L+S method provides improved results in a free breathing environment for abdominal and liver DCE MRI.

Different quality assessment parameters like algorithm convergence rate, peak PSNR, SSIM and image SI are used for the comparison of proposed techniques with other methods. For simulated data magnetic resonance extended Cardiac-Torso (MRXCAT), simulation software for cardiac cine MRI, is used to generate breath held and free breathing cardiac cine MRI data. The real MRI data for brain and heart is taken from St. Mary's Hospital London and University of Southern California, Los Angeles, USA respectively. The DCE MRI data for liver and abdominal is taken from Center for Advanced Imaging Innovation and Research (CAI^2R), Department of Radiology, New York University School of Medicine, New York, USA.

1.2 Thesis organization

This dissertation has been organized as follows

Chapter 2 describes the physics involved in MRI and mechanism for generating MR signal (*k*-space data). The reconstruction of MR images from acquired data is also introduced and

discussed as inverse problem. Advanced MR recovery methods related to this dissertation are described followed by the introduction of DCE MRI.

Chapter 3 introduces the problem of motion in MRI. It presents a brief description of cardiac CINE and abdominal DCE MR imaging in the presence of respiratory motion followed by current techniques used to deal with the respiratory motion.

Chapter 4 presents initially a comparison of surrogate functions, used in CS-based optimization problem. The best-chosen surrogate function is then used in the newly proposed method for dynamic MR imaging in the presence of respiratory motion. The results for simulated and in-vivo data along with discussion is presented at the end of chapter.

In chapter 5, an adaptive regularization parameter based on MAP estimator is derived. It is followed by a new iterative algorithm based on adaptive parameter for static and dynamic MR images.

Chapter 6 discusses a new methodology for the reconstruction of accelerated DEC MR images in the presence of respiratory motion. Improved results for real MR data sets, by combining L+S matrix decomposition and data binning, are given at the end of chapter

Chapter 7 provides the concluding remarks about the current research followed by some future directions of research.

Chapter 2

MRI: Data Acquisition and Reconstruction

This chapter discusses the MRI data acquisition and reconstruction process. The basic physics and imaging principles for MRI modality are generally introduced with the focus upon the information related to this thesis. It also describes the reconstruction as inverse problem and some recent advance methods for MR images recovery. Details regarding MRI basics can be found in [7-9].

2.1 Data acquisition in MRI

MRI is a non-invasive imaging modality. Its scanner uses magnetic fields and radio frequencies to generate the images of body organs. Nuclear Magnetic Resonance (NMR) is the basic physical phenomena used in MRI. It exploits the atom's basic property of intrinsic angular momentum also called spin. This momentum generates magnetic field (magnetic moment) in atomic nuclei with odd number of protons or neutrons. The most important atom with only one proton is hydrogen due its large existence in human body water and lipids. MRI exploits the magnetic moment of hydrogen atom for generating images. In MRI examination process, three types of magnetic fields involved in imaging are:

1. ***Static magnetic field $\boldsymbol{B_0}$***: In the absence of external magnetic field i.e. B_0, the random orientation of the hydrogen atom produces zero magnetic moment. However, the

spin of hydrogen nuclei (protons) will align with externally applied static magnetic field B_0. The alignment will be either up (parallel) or down (antiparallel) with respect to B_0. The antiparallel state has slightly greater energy as compared to parallel state and very less protons adopt antiparallel state. The exact ratio of parallel and antiparallel protons depends upon the strength of applied magnetic field and temperature[10] and can be found by Boltzmann statistics. This difference in alignment will produce a net magnetic moment X_0, having the same direction as B_0, and is called longitudinal magnetic field. The concept is shown in Fig. 2-1. The external field B_0, measured in units of Tesla (T), is extremely uniform and strong normally 1.5 T or 3.0 T, 50000 times stronger than earth's field.

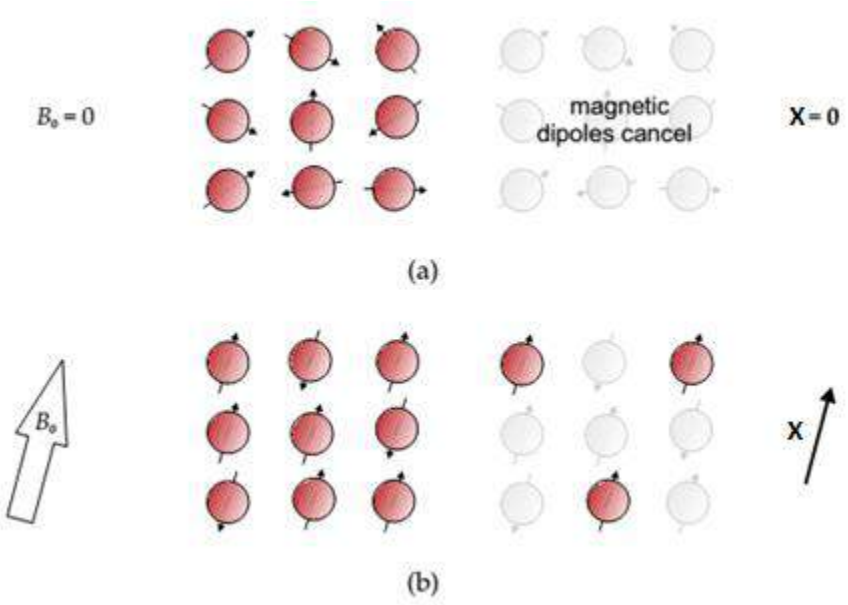

Fig. 2-1 Hydrogen atoms magnetic moment a) Without application of external field b) with application of external field

2. Radio frequency excitation magnetic field B_1: The net number of proton spins in up and down state is normally very small, and hence generate very small magnetic field X_0 of the order of micro Tesla. To generate a strong and measurable field from aligned protons, another external magnetic field B_1 is applied for a short time. The frequency of B_1 is

normally in the range of radio frequency (RF) and its duration is very brief. It is called RF pulse. The application of B_1 (RF pulse) tilts the magnetization vector by an angle alpha towards the plane perpendicular toX_0. The flip angle alpha (α) depends upon the strength and pulse duration of B_1. The idea is shown in Fig. 2-2.

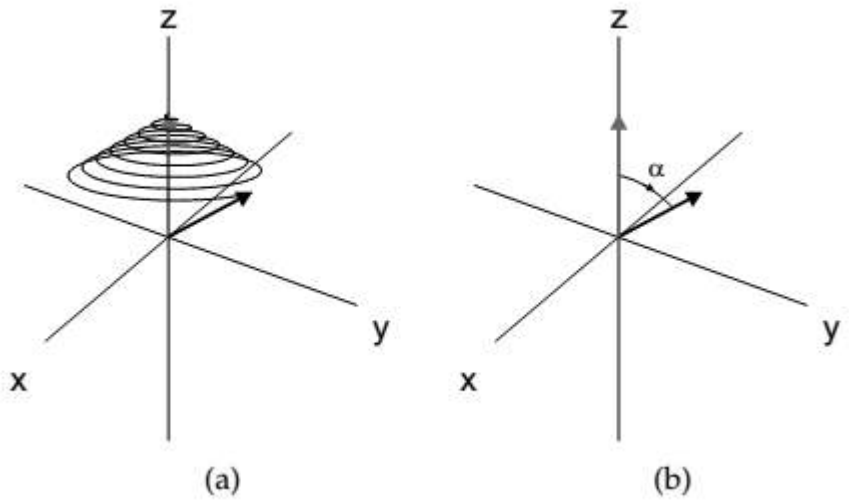

Fig. 2-2 Effect of RF pulse on magnetization vector X_0

The aligned protons precess around the axis of B_0 due to these RF pulses. The precession frequency of proton will be same as the RF signal and is called Larmor frequency and its value is approximately 63.9 *Mhz* for 1.5T MRI machine. The magnetization vector has two components X_z, the longitudinal component, and X_{xy} transverse component. At the removal of RF pulse, the magnetization vector component X_z and X_{xy} experiences an exponential decay with time T_1 and T_2 respectively. These relaxation times depend upon the structure and composition of body tissues. The decaying magnetic components result in decreasing signal strength over time. This phenomenon, known as free induction decay (FID), produces voltages in the RF receiving coils and used for MR imaging.

3. Spatially varying magnetic field gradient: The RF coils receive electromagnetic signal, containing the information about the local tissues, without the spatial source of the signal. In MRI, the process of connecting generated signal to its spatial location is known as spatial encoding. Three gradient coils generating magnetic gradient G with linearly varying magnitude in x, y and z (G_x, G_y, G_z) direction are used for spatial encoding. Variation in gradient components i.e. G_x, G_y and G_z enables MR scanners to produce images in sagittal, cornel and axial directions respectively. The interaction between these fields is normally depicted by a timing diagram, called pulse sequence diagram. Three types of spatial gradients known as slice selection G_z, phase encoding G_y and frequency encoding G_x are used in pulse sequence of MRI and shown in Fig. 2-3

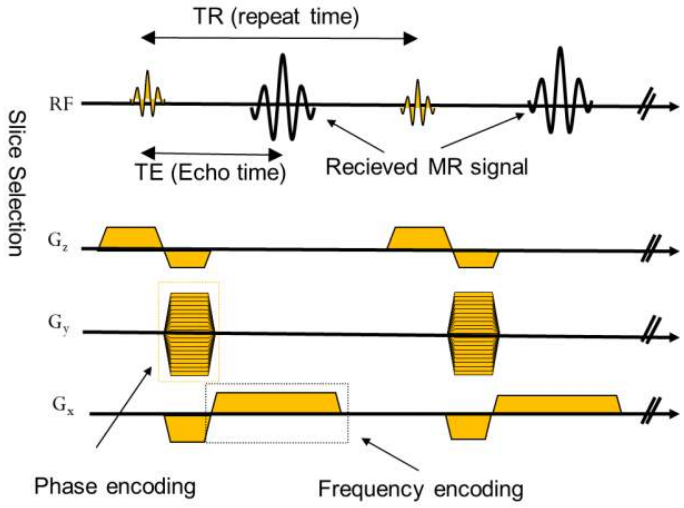

Fig. 2-3 Timing diagram used in spatial encoding for different gradients.

The spatial encoding starts with the slice selection. It involves the selection of a sub volume (slice) from a three-dimensional object by setting the gradient magnitude, transmitting RF pulse frequency and bandwidth. Different slice locations and widths can be achieved by changing these parameters. After the selection of a slice with some specific thickness, the

applied signal will be localized to that slice. Now the scanner records the two-dimensional distribution of magnetization. Spins at different special location with different precession rate can be achieved by varying additional gradients along the selected slab, so that individual contributions of protons can be measured.

In the phase encoding process, a constant gradient G_y in y direction is applied for a brief period. It will change the precession frequency linearly in the selected slab. On the removal of G_y, the Larmour frequency returns to a fixed value, producing different phases to the spatial locations of signal along y axis. Number of phase encoding levels directly affects the spatial resolution of MR images. Similarly in the frequency encoding process, a constant gradient G_x in x direction will change the Larmour frequency along x axis linearly. This process will create a linear relationship between frequency and special location of signal along this direction.

2.2 Image reconstruction

This section shows how to obtain magnetic resonance based image of the human organ from the data acquired during an MR examination. The process of MR imaging from *k*-space data is not a straight forward operation. For generating final image, samples obtained after the application of RF pulses are sorted in a raw matrix known as *k*-space. To fill up the *k*-space, the pulse sequence discussed above is repeated after every TR (repetition time) seconds. Each point with unique phase and frequency in *k*-space belongs to a specific special location in the selected slice. The MR signal acquired using spatial encoding can be represented as Fourier transform of magnetization

$$S(\boldsymbol{k}) = \int X_0(\boldsymbol{r}) exp(-2\pi i \boldsymbol{k}.\boldsymbol{r}) d\boldsymbol{r} = \mathcal{F}\{S(\boldsymbol{k})\} \tag{2.1}$$

Where the magnetization $X_0(\boldsymbol{r})$ represents the spatial domain image, and $\boldsymbol{k}$ is a vector position in the Fourier domain of the $X_0(\boldsymbol{r})$. This (2.1) shows that the MR scanners give a Fourier encoded images. Hence the image can be reconstructed by taking inverse Fourier transform $X_0(\boldsymbol{r}) = \mathcal{F}^{-1}\{S(\boldsymbol{k})\}$, which is normally done with fast Fourier transform (FFT) [11]. Fig. 2-4 shows the *k*-space and the original MR image of human brain obtained at St. Mary's Hospital London using 1.5 Tesla GE HDxt scanner with an eight-channel head coil and a gradient echo sequence with the following specifications: TR/TE=55/10 msec, FOV =20 cm, bandwidth=31.25 KHz, slice thickness= 3 mm, flip angle= 90°, matrix size=256×256.

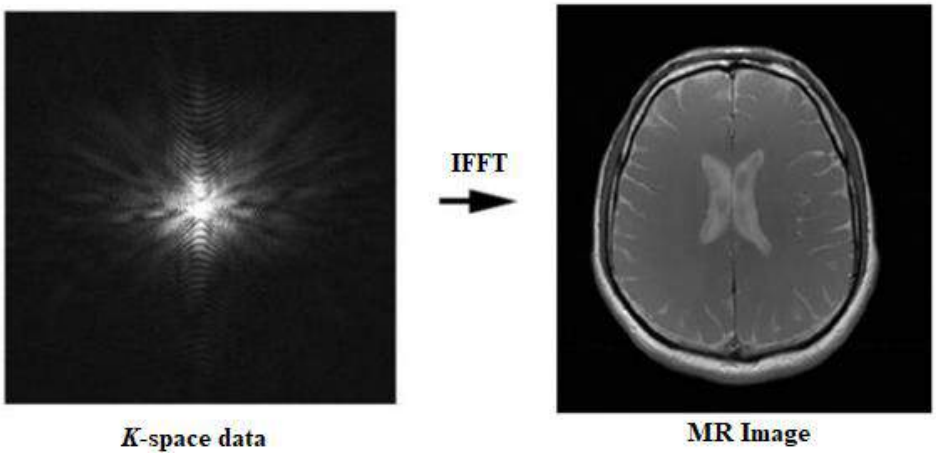

Fig. 2-4 *k*-space and MR image

However, to implement (2.1) we need infinite number of *k*-space samples which is practically not feasible. To perform the MR scan in a reasonable time, finite and discrete number of *k*-space samples must be acquired. The discrete version of (2.1) can be obtained using Dirac comb function as follows.

$$S(\boldsymbol{k}_n) = S(\boldsymbol{k})\mathrm{III}(\mathrm{k}) = \mathrm{S}(\mathbf{k})\sum_{n=-\infty}^{+\infty}\delta\,(\mathbf{k} - \mathrm{n}\boldsymbol{\Delta}_{\boldsymbol{k}}) \qquad (2.2)$$

Where $\boldsymbol{\Delta}_{\mathrm{k}}$ represents the distance between the samples. Using the convolution theorem, the reconstructed image can be represented as follows:

$$X_0(\boldsymbol{r_n}) = \frac{1}{\Delta_k}\sum_{n=-\infty}^{+\infty} X_0(\boldsymbol{r} - \frac{n}{\Delta_k}) \tag{2.3}$$

It can be seen from (2.3) that the MR image can be reconstructed from limited number of samples with a scaling and periodicity factor of $\frac{1}{\Delta_k}$. For the MR image, field of view (FOV) depends upon the spacing between the samples i.e. Δ_k. Doubling the distance between uniform k-space samples will cause the replicas of image to overlap with each other. This effect is called aliasing and will decrease the FOV to half of the original [12]. Effect of under sampling is shown in Fig. 2-5

2.3 MRI data recovery as inverse problem

MR image recovery problem can be formulated as a linear inverse problem. using the quadrature rule, the discrete version of integral given in (2.1), defined for a FOV ranging from $-\mathrm{r}_{\max}$ to $+\mathrm{r}_{\max}$, can be written in finite sum form[13]:

$$\int_{-r_{max}}^{+r_{max}} X_0(r)\exp(-2\pi i\mathbf{k}.\mathbf{r})\mathrm{d}\mathbf{r} \approx \sum_{j=1}^{n} X_0(\mathbf{r}_j)\exp(-2\pi i\mathbf{k}.\mathbf{r}_j)\Delta\mathbf{r} \tag{2.4}$$

The (2.4) represents a system of linear equations given by

$$\mathbf{y} = \mathbf{F}\mathbf{x} \tag{2.5}$$

where **y** is the *k*-space data acquired during MR examination, **F** is the Fourier operator and **x** corresponds the image to be recovered. (2.5) shows that the MR image can be reconstructed by inverting the system of linear equation. It is like to solve a linear problem of the type $\mathbf{b} = \mathbf{A}\mathbf{x}$, where **A** is equivalent to the known Fourier operator, vector **b** is same

as *k*-space acquired data and it is also known and unknown vector **x** belongs to the recovered image.

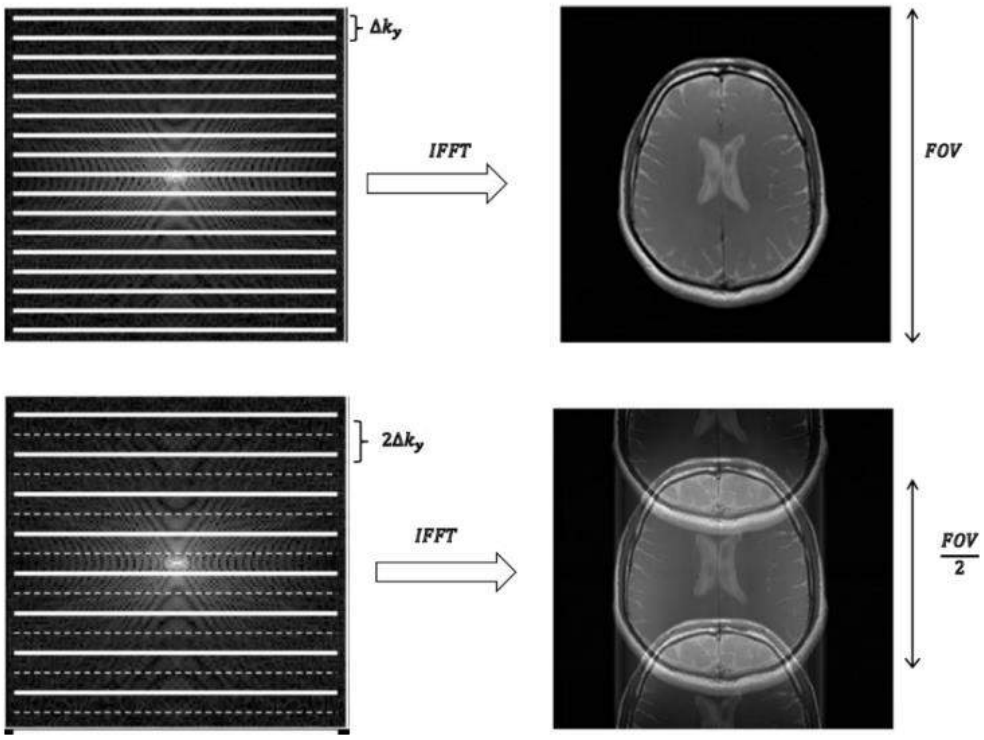

Fig. 2-5 Aliasing effect of uniform under sampling

The invertibility of a system is said to be well-posed if it satisfies Hadamard conditions which are the existence, uniqueness and stability of the solution. Existence of the solution is a rare problem in MR recovery due to operator consistency. However, MR image recovery from limited number of samples (underdetermined system of equations) does not fulfill the uniqueness or stability condition. Hence the perfect recovery from discrete samples of *k*-space is not possible. However, for some appropriate conditions and using some prior information, an approximate version of original image with very minute differences can be generated. Use of prior information to cater non-uniqueness and instability is called the regularization process.

2.3.1 Inverse problem solution

The previous discussion shows that, the MR image can be reconstructed by solving the system of linear equations given in (2.5). Practically, the unknown image $\mathbf{x}$ canbe found by minimization of the residual energy that is:

$$f(\mathbf{x}) = min_{\mathbf{x}} \|\mathbf{Fx} - \mathbf{y}\|_2^2 \tag{2.6}$$

Where ($\mathbf{Fx} - \mathbf{y}$) is the residual or error term.

The minimum of $f(\mathbf{x})$, found by setting its derivative to zero i.e. $\nabla f(\mathbf{x}) = 0$, can be given as:

$$\mathbf{x} = (\mathbf{F^H F})^{-1} \mathbf{F^H y} \tag{2.7}$$

Where H shows the conjugate transpose. Finding $(\mathbf{F^H F})^{-1}$ is not always computationally easy; however using iterative methods provides fast solutions. Gradient decent method is simple iterative method but conjugate gradient(CG)[14] another iterative method, provides more efficient solution to the above problem.

2.3.2 Inverse problem stability

Different strategies are available to improve the stability of an invertible linear system. One approach is preconditioning. Another approach for stabilization is to use regularization term, based on prior information. For example, Tikhonov regularization is normally used for noise suppression and can be given as

$$f(\mathbf{x}) = min_{\mathbf{x}} \|\mathbf{Fx} - \mathbf{y}\|_2^2 + \lambda \|\mathbf{x}\|_2^2 \tag{2.8}$$

Where λ is a Lagrange multiplier that controls the balance between the error energy term $||\mathbf{Fx} - \mathbf{y}||^2$ and the regularization term $||\mathbf{x}||^2$. The close form solution to this problem can be given as:

$$\mathbf{x} = (\mathbf{F^H F} + \boldsymbol{\lambda} \mathbf{I})^{-1} \mathbf{F}^{\mathrm{H}} \mathbf{y} \tag{2.9}$$

Sparsity regularization, an alternative stability method, minimizes the number of non-zero elements in either image domain or in some transform domain. To implement this regularization, the assumption is that the image can be represented by small number of non-zero values i.e. image must be compressible. Optimization problem, formulated with sparsity regularization, can be given as follows:

$$f(\mathbf{x}) = min_{\mathbf{x}} \|\mathbf{Fx} - \mathbf{y}\|_2^2 + \lambda \|\mathbf{\Psi x}\|_0 \tag{2.10}$$

Where $\mathbf{\Psi}$ operator transforms the MR image into sparse domain and $||.||_0$ (l_0-norm) is the pseudo-norm that measures the sparsity of image. Due to combinatorial nature, implementation of l_0-norm is computationally intractable i.e. NP-hard. In the most practical situations, compressively sampled MR images can be recovered effectively using l_1-norm instead of l_0-norm [15, 16]. The minimization problem with l_1-norm can be given as:

$$f(\mathbf{x}) = min_{\mathbf{x}} \|\mathbf{Fx} - \mathbf{y}\|_2^2 + \lambda \|\mathbf{\Psi x}\|_1 \tag{2.11}$$

Like l_0-norm, l_1-norm also promotes sparsity in the solution [17]. By computing the derivative and setting it equal to zero gives the following solution:

$$(2\mathbf{F^H F x} + \boldsymbol{\lambda} \mathbf{\Psi^H W \Psi})\mathbf{x} = 2\mathbf{F^H y} \tag{2.12}$$

The l_1-norm is a discontinuous function and its derivative at the origin does not exist. Defining $|x| = \sqrt{x^H x + \mu}$ then the diagonal matrix **W** has elements:

$$w_i = \sqrt{(\mathbf{\Psi x})_i^H (\mathbf{\Psi x})_i + \mu}$$

where $0 < \mu \lll 1$ and i denotes the diagonal index. (2.12) corresponds to a nonlinear system, since **W** depends on **x**. Nonlinear optimization problems can be solved with alternative methods like projection onto convex sets (POCS) [18, 19] or the nonlinear Conjugate Gradient [20], for instance.

2.4 Advance reconstruction methods

This section discusses some advanced MR image recovery methods like parallel imaging and compressed sensing reconstructions.

2.4.1 Parallel imaging

Parallel Imaging is commonly used in clinical MRI. Currently it is implemented with an acceleration factor ranging from 2 to 4 times. As discussed in section 2.1, to avoid aliasing, at least two times more samples of *k*-space date are required to generate an alias-free image. Larger Δ_k will make the operator **A** under determined and alias-free image reconstruction will be impossible. This situation is like the accelerated acquisition in which every other line of *k*-space is acquired, and for a fixed FOV, the reconstructed image will not be alias-free. These under sampling artifacts can be removed by adding some additional equations to the linear system.

MR scanner uses multiple receiving coils to receive the MR signal from different body organs. Parallel imaging uses the spatial information of these receiving coils to reconstruct the alias free images. MR Signal equation (2.1) with coils spatial sensitivity can be given as

$$S_j(\mathbf{k}) = \int C_j(\mathbf{r}) X_0(\mathbf{r}) \exp(-2\pi i \mathbf{k}.\mathbf{r})\, d\mathbf{r} = \boldsymbol{\mathcal{F}}[\boldsymbol{C_j}(\mathbf{r})\boldsymbol{X_0}(\mathbf{r})] \tag{2.13}$$

where $C_j(\mathbf{r})$ represents the complex sensitivity map for j^{th} coil. The corresponding linear system in matrix form is:

$$\mathbf{y} = \mathbf{AFCx} \tag{2.14}$$

Where $\mathbf{A}$ is a logical matrix that under samples the *k*-space data, i.e. the sampling pattern, $\mathbf{F}$ is the Fourier operator and $\mathbf{C}$ is a diagonal matrix with the coil sensitivity map. (2.14) represent the famous formulation of SENSitivity Encoding (SENSE) reconstruction [1, 21]. The inversion of encoding matrix denoted by $\mathbf{E} = \mathbf{AFC}$ is an easy task for Cartesian sampling pattern. However, for complex sampling patterns, iterative methods for inversion will be required.

In parallel imaging, the sensitivity maps are normally estimated during MR examination. calibration scan [1] for estimating sensitivity maps is one approach. Another way is to estimate the sensitivity maps from the central part of *k*-space data itself [22, 23].The above discussion about parallel image in from SENSE point of view. Other common approaches for parallel imaging are SMASH [24],GRAPPA [25] and SPIRiT [26] which uses the information of multiple coils enforce the same information in a different way. In the recent past a famous method has been introduced, based on prior information of MR image structure, and is known as compressed sensing.

2.4.2 Compressed sensing

Compressed sensing or sampling (CS) [3, 27] is a method that speed up the MR examination process by exploiting the prior information about the MR data. Under some certain conditions, CS can violate the Nyquist criterion and can recover the MR images from under sampled *k*-space data [2, 27]. The idea of reconstruction is closely related to

the denoising of sparse images [16], where the images can be recovered with a reasonable accuracy. To implement CS, three basic requirements are: sparsity of image in pixel or in some transform domain, random under sampling scheme and some nonlinear recovery technique [4, 6, 27]. The random under sampling converts the CS recovery problem to denoising because this type of sampling generates the noise like artifacts instead of aliasing. Noise-like artifacts can be generated with any sampling pattern which samples the central part of *k*-space heavily as compared to the rest of *k*-space region. This type of sampling is called variable density random under sampling (VDRU) [4]. Fig. 2-6 shows different sampling patterns and their corresponding recovered images. It can be seen in this figure that various sampling patterns produce different effects in reconstructed images.

Image reconstruction using l_1-norm constraint is equivalent to the denoising operation. CS recovery with l_1-norm regularization can be written as:

$$\hat{\boldsymbol{x}} = min_{\mathbf{x}} \|\mathbf{Fx} - \mathbf{y}\|_2^2 + \lambda \|\boldsymbol{\Psi}\mathbf{x}\|_1 \tag{2.15}$$

Where $\boldsymbol{\Psi}$ transforms the image into some sparse domain**.** It may be an identity matrix for sparse images in pixel domain like angiograms. Other famous sparsifying transform are wavelet, discrete cosine and temporal Fourier transform [28-30]. Recently different dictionaries [31, 32] have also been used to transform the MR image into some domain where the image can be represented with small number of coefficients.

2.5 Dynamic contrast enhanced (DCE) MRI

MRI examination provides images with enough contrasts, so the healthy and unhealthy tissues can be differentiated easily. However, some tissues characteristics are not

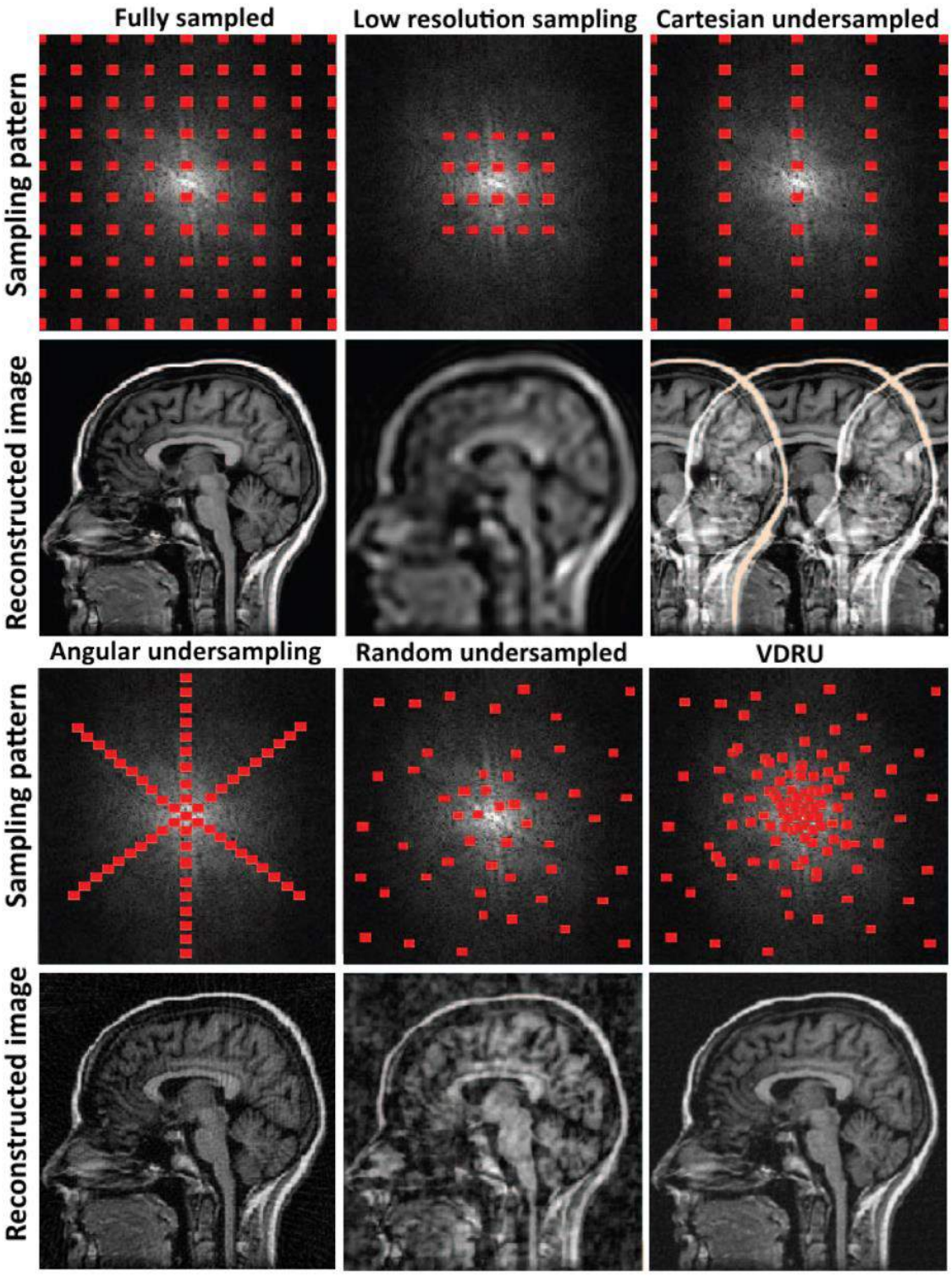

Fig. 2-6 Different (schematic) sampling patterns in *k*-space produce different effects in the reconstructed images. Cartesian under sampling produced image replicas, structured angular under sampling presents more incoherent" streaking" artifacts,

random under sampling produces incoherent aliasing with ”cloud-like” artifacts, variable density random undersampling (VDRU) produces noise-like aliasing. Adapted from[4]

refelected by the tissue relaxation coefficients e.g. tumors manifest excessive formation of blood vessels (vascularization) due to their uncontrolled growth. The vessel walls may be upset in case of malignant tumors and necrotic tissues and causes an escape of vessel contents in the neighboring tissues. Effects of this leakage can be observed with a help of some chemical, called contrast agent (CA), which changes the value of relaxation coefficients of blood and vessels. The concentration of contrast agent, injected as bolus, varies with time and causes a decrease or increase in signal intensity. Hence the differential diagnostic and tumor staging can be detected using the uptake rate of contrast agent.

Two methods are in used for contrast enhanced perfusion. One is dynamic susceptibility contrast (DSC) MRI[33] and other is dynamic contrast enhancement (DCE) MRI [34]. Both techniques use gadolinium (Gd) as a CA. In DSC high concentration of CA is used and mostly utilized for brain perfusion in neuro imaging. DCE MRI enables the measurement of T1 changes in tissues over time after the intravenous bolus of CA. It is mostly used as a bio marker in oncology and for the diagnosis of different diseases [35, 36]. The DCE technique relies on the monitoring of images during uptake and wash out of the low concentration of contrast agent (CA). The relationship of pixel intensities and CA concentration is acquired over time. A pharmacokinetic model based on pixel intensities, CA concentration and time variation is used to generate kinetic parameter values that may be correlated with the characteristics of tissues [37].

2.6 Robust principle component analysis (RPCA)

Robust principle component analysis (RPCA) or L+S matrix decomposition is an improved version of classical principle component analysis (PCA). It decomposes the given matrix into low-rank matrix L, containing small non-singular values, and sparse matrix S having few non-zero entries. The decomposition can only be possible if both L and S matrices are incoherent[38, 39]. The main objective of RPCA is to reconstruct L and S matrices from excessively corrupted and sub-sampled data M. RPCA has been successfully applied in video surveillance, facial recognition and dynamic medical imaging. In these applications, slowly changing back-ground is modeled by L matrix and the fore-ground changes are modeled by S matrix. Solution of the following problem gives L+S matrix decomposition.

$$min\|\boldsymbol{L}\|_* + \lambda\|\boldsymbol{S}\|_1 \qquad s.t. \;\; \mathbb{M} = \boldsymbol{L} + \boldsymbol{S} \tag{2.16}$$

where $\boldsymbol{S}$ represents sparse matrix, $\boldsymbol{L}$ is the low rank matrix and $\mathbb{M}$ is the Casorati matrix.$\|L\|_*$ is the nuclear norm, $\|\boldsymbol{S}\|_1$ is the l_1-norm , and λ is a balancing parameter that defines the share of the l_1-norm relative to the nuclear norm.

2.8 Performance assessment parameters

The quality of recovered medical images is assessed using standard assessment parameters like PSNR, correlation, sharpness index and SSIM. The PSNR and MSE of the results is calculated using following equations

$$PSNR\ in\ dB = 10Log_{10}(MAX_c)^2/MSE \tag{2.17}$$

$$\text{MSE} = \frac{1}{z \times z}\sum_{i=0}^{Z-1}\sum_{j=0}^{Z-1}(P_{ij} - R_{ij})^2 \tag{2.18}$$

Where MAX_c is a maximum pixel value of the current image having dimensions of $Z \times Z$, P_{ij} and R_{ij} are pixels being compared with current and reference images.

Sharpness index (SI), a measuring parameter based on image sharpness is given as [40]

$$SI(x) = -log\phi\left(\frac{\mathbb{m}-TV(x)}{v}\right) \tag{2.19}$$

Where $\mathbb{m} = \mathbb{E}[(TV(x))]$ is the expected value of the total variation of the recovered image I, $v = \mathbb{V}[(TV(x))]$ is the corresponding variance, and φ is the normal distribution tail as given in[40].

Structural similarity index measurement (SSIM) measure the similarity between two images x and $\hat{x}$. Its maximum value is 1 showing that both images are completely similar and it is calculated using following relationship.

$$SSIM(x,\hat{x}) = \frac{(2\Omega_x\Omega_{\hat{x}}+C_1)(2\sigma_{x\hat{x}}+C_2)}{(\Omega_x^2+\Omega_{\hat{x}}^2+C_1)(\sigma_x^2+x_{\hat{x}}^2+C_2)} \tag{2.20}$$

Where $C_1$and C_2 are constants that depends on the dynamic range of the images. Ω_x and $\Omega_{\hat{x}}$ shows the mean values while σ_x^2 and $\sigma_{\hat{x}}^2$ denote the variances of the original and reconstructed image respectively. $\sigma_{x\hat{x}}$ is the covariance between of original and recovered image.

2.7 Summary

In this chapter the MRI data acquisition and MR image generation process is discussed. The basic physics of MRI is presented with the observation that the MR scanner records the Fourier encoded signals. Image recovery is performed by solving linear system of equations. Fast imaging techniques like parallel imaging and compressed sensing along with DCE MRI and RPCA is discussed at the end of chapter.

Chapter 3

Problems of Respiratory Motion in Dynamic MRI

Non-invasive imaging modality, MRI, produces high resolution anatomical details of different human organs. The examination process to acquire the MRI data takes several minutes and it is difficult for a person under the test to remain stationary. Different types of patient motions like bulk motion, respiratory motion, cardiac movement and blood flow produces artifact in the final reconstructed MR image. In this chapter we will discuss the effects of respiratory motion only and specifically for the abdominal and cardiac MR imaging. This chapter also serves as literature review, discusses different solutions to mitigate the motion effects in the MR images.

3.1 Cardiac CINE imaging

Cardiovascular magnetic resonance (CMR) has slow development due to its dynamic nature and effects of subject motions. However due to development of fast algorithms and advancement in hardware, CMR has now widely used in different application like Valvular heart disease, Congenital heart disease, Myocardial ischemia, Myocardial Infarction, Cardiomyopathy etc. In these applications of CMR, the major source of blurring and ghosting is cardiac and respiratory induced motion. These motions are discussed with details in next sections.

3.1.1 Cardiac induced motion

The human heart, responsible for blood taking and pumping, is composed of four chambers: the left and right atrium and left and right ventricle. The artia size is smaller as compared to ventricle and act as a receiving chamber of blood through blood receiving veins. The ventricles are larger and stronger pumping chamber that pump out the blood to the human body. Blood pumping function is a periodic process with compression (systolic) and expansion (diastolic) phases. The systolic phase lasts approximately 400ms and diastolic phase remains for a time ranging from 200 to 800ms [41]. Detail discussion of cardiac induced motion is given in [42-44]. Strong longitudinal and rotational components along with scaling have been observed in the reconstructed images. Osamet. al [45] presents the study of cardiac induced coronary motion for breath hold condition and showed the anterior posterior (AP) motion, foot-head (FH) motion and left-right (LR) motion. The motion amplitude in the right coronary artery (RCA) is typically twice the amplitude in the left coronary artery (LCA).

3.1.2 Dealing with cardiac induced motion

Electrocardiogram (ECG), a method to observe the cardiac electrical activity, is used to fix the cardiac-induced motion. ECG signal provides different functional and structural information of the heart. From cardiac induced motion point of view, ECG records the main events of cardiac activity which includes P-wave, QRS complex, T-wave. P-wave represents the atrial systole, QRS complex represents start of ventricle systole and T wave shows the rest of ventral systole. The approximately smooth section after T-wave represents diastolic phase. This portion is normally taken for data acquisition because the

heart is relatively less motion for long period of time. ECG signal with cardiac activities is shown in Fig. 3-1.

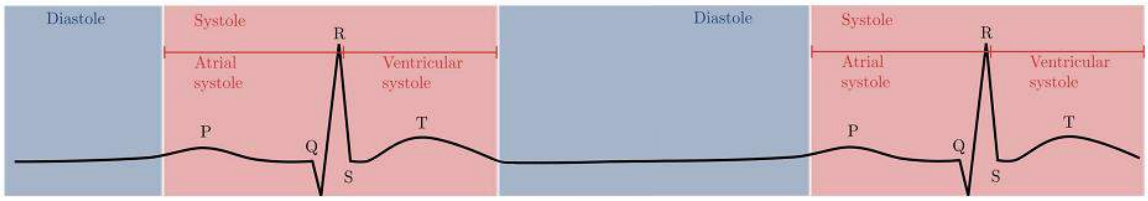

Fig. 3-1 ECG wave form of the cardiac cycle

Cardiac triggering is one method to deal cardiac-induced motion. Periodic motion of heart allows splitting the data acquisition in multiple heart cycles. The subset of data is acquired in a specific window of time less than 100 ms and is applied in the diastolic phase due to the minimal heart motion. The time from R wave to the start of data acquisition is known as trigger delay and it is patient dependent [46]. A major limitation of this technique is the variation in heart beating frequency [47]. Cardiac gating is another method to resolve cardiac induced motion. In this technique, the continuously acquired cardiac phases are labeled with the help of ECG signal and grouped retrospectively to generate CINE image of heart [48].

Fig. 3-2 depicts a comparison between cardiac triggering and gating. a) shows that the motion effects are very less after the mid of diastole i.e. after 750ms. b) Cardiac phases are acquired continuously and numbered according to its heart phase. These techniques are very useful to deal with the cardiac induced motion. However, residual motion effects can be observed even after the use of gating and triggering due to some motion during diastole phase. Cardiac induced motion effects in diastole phase mainly depends upon the size of acquisition window [13]. It can be suppressed using smaller acquisition window and periodic nature of heart cycle and hence rarely corrected.

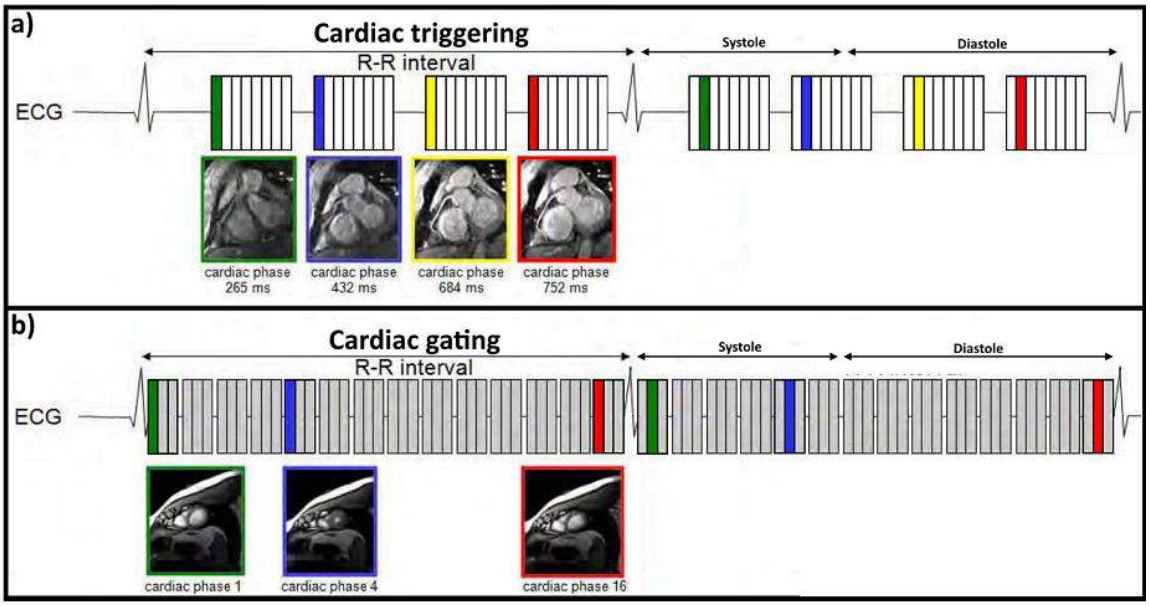

Fig. 3-2 A comparison between cardiac triggering and gating.

3.1.3 Respiratory induced Motion

Motion due to respiration and its effects on the heart has been studied from a long time. The early studies, conducted using X rays modality, showed the FH cardiac motion was approximately half of the diaphragmatic motion [49]. After many years, same effects of respiratory motion on heart in FH direction was observed for MRI and [50] showed that FH cardiac motion is 0.6 of the diaphragmatic motion in MRI. For free breathing conditions, Non- rigid components of motion have been observed in the recent studies in FH, AP and LR [51, 52]. Respiratory motion is more challenging as compared to cardiac motion. The reason is its unpredictable periodic behavior and unavailability of simple models to describe its complex nature and magnitude.

3.2 Abdominal DCE MR imaging

In 1980, the first abdominal MRI examination was performed to diagnose the liver abnormality. Currently the abdominal MRI produces the images of high quality for liver, biliary system, adrenal glands, kidneys, bowel and all related vascular system. Now a day, MRI is preferable imaging modality in clinical routine to image the liver [53]. The contrast in MR images are based on T1 and T2 relaxation coefficients which can be varied by injecting a CA as in the case of DCE MRI. The pre and post contrast images are used to indicate the presence of lesions by detecting the dark and bright areas in the MR image. DCE MRI consists of three phases: pre-contrast phase, arterial phase and post-contrast phase. Current clinical routine is to perform the whole process in breath held condition. Initially the images are taken without CA injection i.e. pre-contrast scan. This phase is followed by CA injection. Waiting for a predefined delay of approximately 15 to 20 seconds after CA injection, the arterial phase images are acquired [54]. In the last phase, after short delay the post contrast images are acquired. The Fig. 3-3shows different phases of Liver DCE MRI.

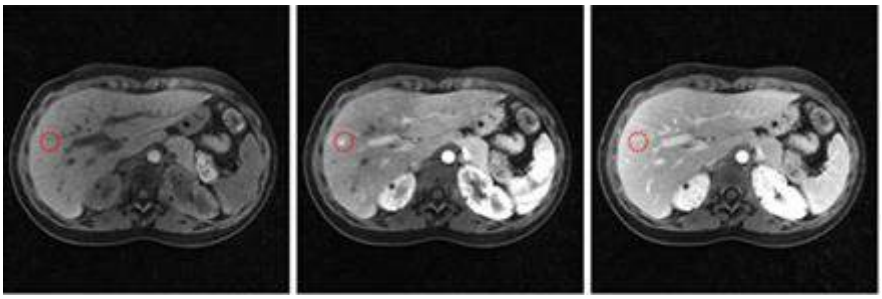

(a) (b) (c)

Fig. 3-3 DCE MRI liver phases. Representing a) pre-contrast b) arterial and c) post contrast.

3.2.1 Abdominal respiratory motion

The complete process of DCE-MRI (uptake and wash out of CA) takes several minutes and it is difficult for a patient to remain still during the scan process. Like other applications of MRI, different types of motion including respiratory motion, heart beat etc. affects DCE-MRI also. The *k*-space lines obtained in distinct respiratory motion states produce inter-frame misalignment and the resulted recovered images are blurry and ghosted [55, 56]. The motion effects are greatly depends upon patient's location[57], breathing depth and varies between different subjects[58]. Respiratory motion is caused by contraction of the diaphragm and expansion of rib cage muscles [59]. During normal breathing, FH motion of the diaphragm has been reported to be in the range of 10-30 mm [60, 61], with AP and LR motion approximately 5 and 6 times smaller, respectively [62]. Motion in the lung away from rigid structures has been measured to be approximately 12 mm in FH, with approximately 2 mm in both LR and AP[63] . Left and right kidney presented average motions of 11 and 13 mm in FH (respectively),4.4 and 6.1 mm in AP, 1.7 and 1.4 mm in LR according to the study in [64]. The same study also evaluated spleen and liver motion: 13 and13 mm (respectively) in FH, 5.0 and 5.2 in AP, 2.5 and 2.1 in LR.

3.3 Literature review

The most common solution to respiratory motion artifacts is the acquisition of data in multiple breath held conditions. [65, 66] discusses the cardiac MR imaging and [67] discusses liver DCE MR imaging with breath hold condition. However, breath hold is not possible in all case especially for aged and pediatric patients. Moreover, it is difficult to acquire the multiple breath hold data at the same respiratory state and it leads to registration

problems [68]. This method also suffers from a typical blood signal due to compromise of normal physiology[69].

Respiratory gating is another technique to reduce respiratory motion effects in free breathing condition i.e. without breath holding [70, 71]. The data is acquired at some specific respiratory state (normally end expiration) using a 5mm or small gating window to reduce the motion effects. The disadvantage of respiratory gating is the decrease in scan efficiency. The scan time may increase from 30% to 50% in this technique [72]. Respiratory gating technique depends upon the respiratory motion state, normally observed through some external monitoring device like respiratory bellows [70] or extracted from MR data using navigators [72, 73]. Real time MRI [74, 75] has been used for cardiac CINE imaging under free breathing condition but with a compromise on spatial and temporal resolution. Radial sampling, less sensitive to the motion, can be used in free breathing at the expense of increase scan time and mathematical complexity[76, 77]. The major advantage of radial sampling is the extraction of navigator signal using the repeatedly sampled k-space center[78]. Navigator signals are used for the estimation of motion in MR images. Image navigator is a recent method to estimate the motion from the real time low resolution images of heart [79, 80].

Respiratory motion correction is another way to handle the motion effects in the acquired data. In this technique the data is acquired in the presence of motion and motion artifacts are then removed from the reconstructed images using motion estimation and correction methods. CS with different sparsifying transform has been successfully combined with various motion correction techniques to reduce the motion artifacts [81, 82]. Image registration methods for rigid and non-rigid body motion have been applied for cardiac

perfusion imaging, cardiac cine[83, 84] and abdominal DCE MRI analysis [85]. These methods exploit the high acceleration rate capability of compressed sensing for the recovery of dynamic MRI.

Otazo et. al. [83] proposed one dimensional translational respiratory motion correction. Usman et. al. [84] introduced a reconstruction scheme for dynamic cardiac MRI by incorporating general motion framework directly into CS reconstruction. Their method uses data binning and intensity based non-rigid registration algorithm for estimating respiratory motions. Ahmed et. al. [84] proposed a CS based motion correction in the free breathing environment with multiple constraints. This method uses demon based registration to estimate the motion between reference and other respiratory states.

Inter-frame motion estimation and compensation for time varying features of images has been used in video compression standards [86, 87]. These standards are based on different block matching algorithms [88] for motion estimation and compensation. Similar to video compression, dynamic MR images can be predicted by exploiting temporal redundancies between the images. Asif et al. proposed an algorithm, MASTeR [89] for the breath held condition, based on inter-frame motion to recover different cardiac MR images. MASTeR uses motion adaptive transform that models temporal sparsity using inter-frame motion estimation. k-t FOCUSS [89] also uses inter-frame motion estimation and compensation with a fixed reference frame during the image recovery process for breath held cardiac cine MRI.

In DCE MRI, the contrast agent produces strong intensity variations over time. This intensity change is another challenge along with respiratory motion in free breathing DCE MRI. To generate a good quality MR image, intensity variation and respiratory motion

must be distinguished from each other before using registration based methods or CS based L+S decomposition method. L+S decomposition (also known as the robust principle component analysis) is a recently used technique for CS-based dynamic MRI. It represents the dynamic MR images as a superposition of a slowly varying background component and a rapidly changing foreground dynamic component [90]. Gao et al. [91] proposed a combined approach of CS and L+S decomposition for the recovery of retrospectively sub-sampled cardiac cine data and a series of diffusion-weighted images. Otazo et.al [90] applied L+S decomposition to recover accelerated dynamic cardiac perfusion and free breathing DCE MR images. They recovered the final images by combining CS and L+S decomposition without any pre-processing step for respiratory motion.

3.4 Summary

In this chapter we discuss the respiratory motion effects in cardiac and DCE MR imaging. The previously proposed solutions like breath hold, cardiac gating and motion estimation and correction to mitigate respiratory motion effects in cardiac imaging are discussed. Combination of CS and L+S decomposition to mitigate the respiratory motion in DCE MRI is also discussed at the end of chapter.

Chapter 4

Recovery of Compressively Sampled Free Breathing Dynamic MR Images Using L_1-Norm Approximation

The medical advantages of MRI were observed since its beginning in 1971. Currently, MRI provides clinical information of all human organs with the main limitation of long examination time that result in motion during scanning process. Motion during MR scanning is the major source of artifacts in the recovered images. Removal of these artifacts from acquired MR data set is an evolving area with a great potential for new research fields. As discussed in previous chapter, different motion correction schemes have been proposed to remove or reduce the motion artifacts. The reconstruction of MR images can be further improved by investigating different algorithmic and functional aspects of these schemes. In this chapter, we aim to focus on a new algorithm and functional approximation of penalty terms for motion estimation and correction, which gives better results as compared to existing schemes.

4.1 Introduction

The first section provides a comparison of surrogate functions, used to approximation the l_1-norm penalty in the optimization problem. Convergence rate of nonlinear conjugate gradient algorithm with backtracking line search is investigated for the two surrogate functions. Structural similarity index (SSIM) for different acceleration rates, Gaussian noise levels in MR images and root mean square error (RMSE) for recovered MR images

is calculated. Simulation results for hyperbolic tangent function, used as a surrogate function for l_1-norm, show improved convergence rate, low RMSE and better SSIM. The parameters are evaluated for different sampling factors as well as for various Gaussian noise levels.

In the second section a novel framework is proposed for the recovery of cardiac MR images in the presence of free breathing motion. To recover motion free dynamic MR images, a step wise methodology is adopted. Compressively sampled MR images are recovered initially by solving an optimization problem using gradient descent algorithm. The l_1-norm based regularizer, used in optimization problem, is approximated by a hyperbolic tangent function. ARPS algorithm is then exploited to estimate and correct respiratory motion among the recovered images. The framework is tested for free breathing simulated and in-vivo 2D cardiac cine MRI data. Simulation results show improved SSIM, peak signal to noise ratio (PSNR) and mean square error (MSE) with different acceleration factors for proposed method as compared to CS-free breathing without motion estimation and correction (MEMC). Experimental results also provide a comparison between k-t FOCUSS with MEMC, another recovery technique for dynamic MR images, and the proposed method.

4.2 Surrogate functions for l_1-norm penalty

To use the efficient algorithms based on gradient of cost function for getting optimum solution, l_1-norm needs to be continuous everywhere. In literature, this type of problem is normally solved by approximating the discontinuous function. Reference [92] uses Gaussian function and sigmoid function for smooth approximation of l_0-norm. Jawad et.

al [93] and Lustig et. al [4] used continuous surrogate functions, given in (4.1) and (4.2), as an approximation for absolute value in l_1-norm to solve non-differentiability problem.

$$|x|_1 \approx \beta x \tanh(\gamma x) \tag{4.1}$$

$$|x|_1 \approx \sqrt{x^* x + \mu} \tag{4.2}$$

Where x^* represents the conjugate of x and β, γ and μ are the variable parameters for better approximation. Comparison is based on algorithm convergence time, SSIM and RMSE for under-sampled MR images. Multi-parameter surrogate function, hyperbolic tangent given in (4.1), performs better and is more robust for noise compared to the function given in (4.2). Nonlinear conjugate algorithm with back tracking line search given in [4] is used with both approximations to solve l_1-minimization problem.

4.2.1 Surrogate functions comparison

A surrogate function used as an approximation should satisfy two conditions [94]

1. Function $f(x)$ must be smooth and continuous to calculate the gradient of cost function.
2. Function $f(x)$ must be bounded between 0 and 1 for the normalized values of x.

Magnified view of the approximation quality comparison, defined in (4.1) and (4.2) at the origin, is shown in Fig. 4-1. This part of figure is taken from combined graph drawn for the interval [-1, 1]. Other parameter values are set as follows: γ=20, β=1 and μ = 1x10^{-6}. It can be observed that both approximations are close to l_1-norm but tangent hyperbolic function is exactly zero at the origin for given value of γ while other function has a minimum value approaches to μ not to zero. Hence the minimum value for approximation

is violated by the function given in (4.2) and hyperbolic tangent function has a better approximation for l_1-norm.

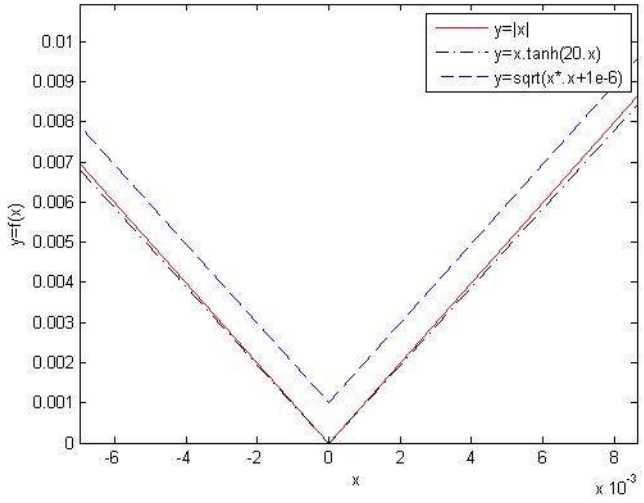

Fig. 4-1Comparison of magnified view at origin for two approximate surrogate functions and |x|.

4.2.2 Simulation setup and results

To compare both function, a volunteer brain image data set with nonlinear conjugate algorithm discussed in [4] is used for all simulations. Variable density function is used to under sample the data and 39 % *k*-space samples are used in the MR images recovery process. Original brain image and sampling pattern used in [4] is shown in Fig. 4-2. To sparsify the MR images, Daubechies-4(db4) wavelet is used as sparsifying transform.

4.2.3 Convergence rate comparison for MR images.

In first simulation, we compare the convergence rate of algorithm for both functions. The parameter values for algorithm and approximate function are chosen as follows: λ=0.005, γ=4 and μ= $1x10^{-15}$

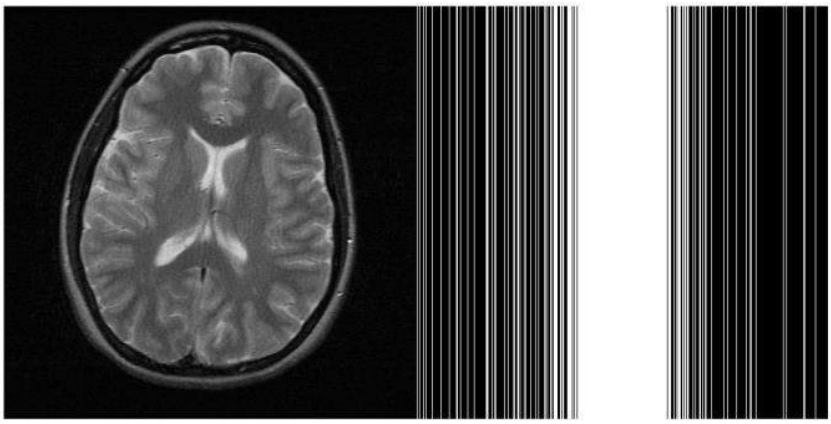

Fig. 4-2 Original brain image and corresponding sampling pattern

Fig. 4-3 show that algorithm with hyperbolic tangent function converges fast and to low RMSE value as compared to other function. These results are obtained by varying γ values to produce fast convergence along with optimum values of RMSE.

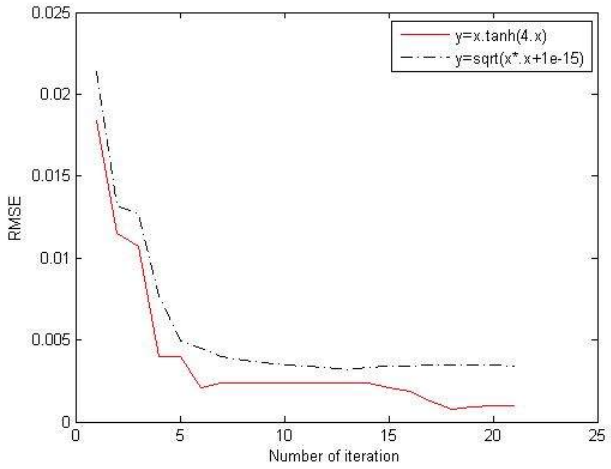

Fig. 4-3 Convergence comparison for both surrogate functions in terms of RMSE

4.2.4 Performance comparison for surrogate functions in the presence of noise

In this experiment MR images, corrupted by different level of zero mean Gaussian noise, are recovered. Recovery process is performed using both surrogate function. SSIM is used

as a comparison measure. The parameter values for algorithm and approximate function are chosen similar as in simulation 1. Fig. 4-4 shows the SSIM versus noise variance for each surrogate function. It can be seen that for all noise variances hyperbolic tangent function outperforms the function in (4.2)

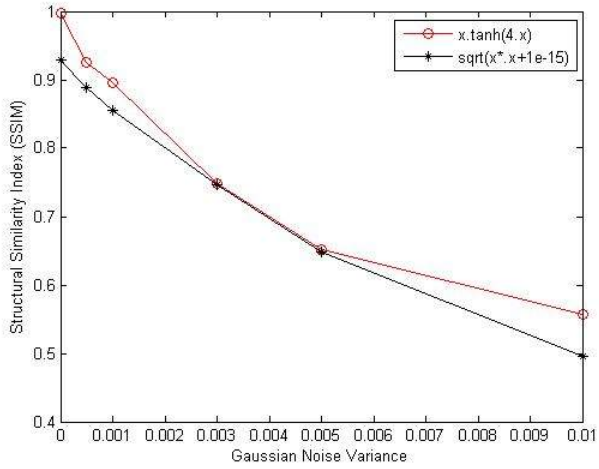

Fig. 4-4 Robustness comparison for surrogate functions against Gaussian noise

4.2.5 Performance comparison for surrogate functions for different acceleration rates

In third simulation, performance of both surrogate functions is compared for different acceleration rates. Fig. 4-5 represents the better recovery for hyperbolic tangent function at all acceleration rates in terms of SSIM. This improved result is intuitive since there is a strong connection between under-sampling and Gaussian noise denoising [4]. Under-sampling introduces a noise with Gaussian noise properties. As mentioned above, hyperbolic tangent function outperform in Gaussian noise, so it is better for different under-sampling factors also as compared to function in (4.2).

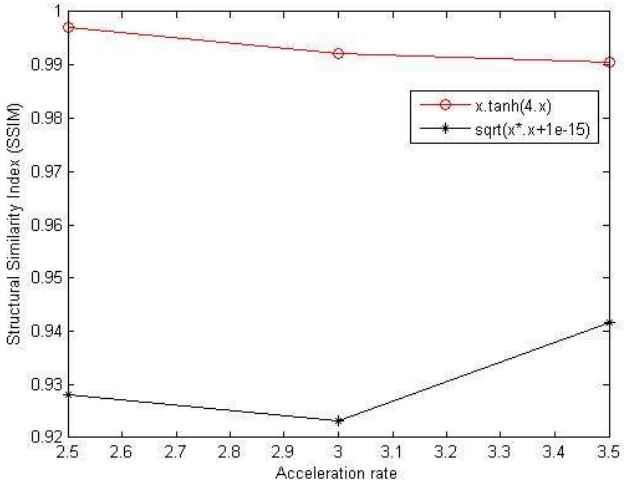

Fig. 4-5 Performance comparison of surrogate functions for acceleration rates of 2.5, 3 and 3.5

4.3 Free breathing cardiac MR images recovery using Hyperbolic Tangent function

In this section a novel framework is proposed for the recovery of highly under sampled free breathing cardiac MR images. The proposed technique is divided into two steps. The first step recovers cardiac images by solving an optimization problem using gradient descent algorithm. The penalty term in the cost function is approximated by the tangent hyperbolic function. The second step estimates and correct the respiratory motion using ARPS algorithm. Use of hyperbolic tangent function along with motion compensated residual in the cost function improves the final results.

4.3.1Free breathing imaging model and CS

Free breathing down sampled k-spaced data corrupted by motion states d=1, 2, 3 …. D for cardiac phase n =1, 2, 3…..N is mathematically given as

$$\boldsymbol{y}_n = \sum_{d=1}^{D} \boldsymbol{A}_{d,n} \boldsymbol{F}\boldsymbol{x}_{d,n} = \sum_{d=1}^{D} \boldsymbol{\Phi}\, \boldsymbol{x}_{d,n} \quad (4.3)$$

Where $\boldsymbol{x}_{d,n}$ is a two dimensional complex MR image vector of length T representing a cardiac phase n at respiratory state d. $\boldsymbol{F}$ is a Fourier operator that transform an image to k-space. $\boldsymbol{A_d}$ is a random variable density under sampling mask, different for all respiratory states and $\boldsymbol{\Phi} = \boldsymbol{AF}$ is a sensing matrix. $\boldsymbol{y}_n$ is a combined k-space measurement vector of length C for n^{th} cardiac phase acquired for all respiratory positions. A single cardiac phase n at respiratory state d in a specific heart cycle can be given as

$$\boldsymbol{y}_{d,n} = \boldsymbol{A}_{d,n}\boldsymbol{F}\boldsymbol{x}_{d,n} = \boldsymbol{\Phi}\boldsymbol{x}_{d,n} \tag{4.4}$$

The reduction or acceleration factor for MR images is given by $R = T/C$. By increasing R, the system in (4.3) becomes highly underdetermined. As discussed in chapter 2, compressed sensing solves such under-determined system of equations effectively to recover MR images.

4.3.2 Smooth l_1-norm approximation

CS algorithms recover sparse signals or images by solving the l_1-norm regularized optimization problem such as given in (2.15) and gradient descent algorithm for solving the optimization problem with wavelet based penalty term. Non-differentiability of the l_1-norm at origin excludes the usage of mostly optimization approaches for the solution. As discussed in section 4.1, two approximation functions have been used in literature given by (4.1) and (4.2).

The results discussed in section 4.1 depicts that the function in (4.2) provides better results since it approximates the absolute value more accurately and provides extra flexibility of adjusting the slope at the origin with the proper selection of γ and makes it more suitable for dynamic images. The proposed iterative algorithm uses the following approximation

for the l_1-norm penalty

$$\|\boldsymbol{x}\|_1 \approx \sum_{i=1}^{T} x_i \tanh(\gamma x_i) = \sum_{i=1}^{T} \alpha\,(x_i) \tag{4.5}$$

Where $\alpha(x_i) = x_i tanh(\gamma x_i)$. The update equation for the algorithm, derived using the steepest descent method for a sparse vector $\boldsymbol{x} \in \mathbb{R}^{\boldsymbol{T}}$is:

$$\boldsymbol{x_{i+1}} = \boldsymbol{x_i} - \eta \nabla f(\boldsymbol{x_i}) \tag{4.6}$$

Where η is positive valued step size, and -∇ is the gradient operator that differentiates the cost function $f(\boldsymbol{x})$ at i^{th} iteration. During each iteration, shrinkage given in (4.7) is applied in the wavelet domain after (4.6) to reconstruct the MR images.

$$T_\lambda(x) = \max\{|x| - \lambda, 0\}\,.\,sgn(x) \tag{4.7}$$

Where λ is a threshold parameter. By incorporating the approximation$\|\boldsymbol{x}\|_1 \approx \sum_{i=1}^{T} \alpha\,(x_i)$, the cost function can be written as

$$f(\boldsymbol{x}) = \frac{\mathbf{1}}{\mathbf{2}} \|\boldsymbol{\Phi x} - \mathbf{y}\|_{\mathbf{2}}^{\mathbf{2}} + \lambda \sum_{i=1}^{T} \alpha(x_i) \tag{4.8}$$

The gradient of the cost function is easy to compute:

$$\nabla f(\boldsymbol{x}) = \boldsymbol{\Phi}^{\boldsymbol{T}}(\boldsymbol{\Phi x} - \mathbf{y}) + \lambda \sum_{i=1}^{T} \alpha'(x_i) \tag{4.9}$$

with

$$\alpha'(x_i) = tanh(\gamma x_i) + \; x_i \gamma (1 - tanh^2(\gamma x_i)) \tag{4.10}$$

4.3.3 Respiratory motion based dynamical system

Two main problems with free breathing cardiac MRI are:

1. Blurring artifacts are generated by the combination of *k*-space samples for the same cardiac phases at different respiratory states.

2. The combination of *k*-space data in free breathing decreases the sparsity level.

Inter-frame motion is used to estimate the respiratory states between the same cardiac phases. Video standards MPEG, H.264 [86, 87] have successfully exploited inter-frame motion for compression. In the dynamic MRI images, pixels are not significantly displaced in the neighboring frames. Pixel locations can be predicted using inter-frame motion estimation. Temporal redundancy among the frames is advantageous for the prediction of pixel locations. Let $\boldsymbol{x}_{d,n}$ and $\boldsymbol{x}_{d,n+1}$ are images having n^{th} cardiac phases at respiratory states d and $d+1$ respectively. The pixel values of $\boldsymbol{x}_d$ at location (a, b) is closest to the pixel values at $(a + \Delta a, b + \Delta b)$in $\boldsymbol{x}_{d+1}$. The displacement of all pixels in $\boldsymbol{x}_{d,n}$ from (a, b) to $(a + \Delta a, b + \Delta b)$ in $\boldsymbol{x}_{d+1,n}$is represented by motion vectors $(\Delta a, \Delta b)$. According to [3], cardiac phase $\boldsymbol{x}_{d,n}$ at d^{th} respiratory state can be generated from the cardiac phase $\boldsymbol{x}_{d+1,n}$at $(d+1)^{th}$ respiratory state by the following equation

$$\boldsymbol{x}_{d,n} = \boldsymbol{M}_{d+1,n}\boldsymbol{x}_{d+1,n} + \boldsymbol{m}_{d,n} \tag{4.11}$$

Where $\boldsymbol{M}_{\boldsymbol{d+1,n}}$is a backward transformation that uses information about the physical changes between two data sets of the same cardiac phases. The motion compensated residual $\boldsymbol{m}_{d,n}$is computed by taking the difference between predicted and compensated image. Using the transformation $\boldsymbol{M}_{\boldsymbol{d+1,n}}$, a motion dependent linear system can be written by combining (4.3) and (4.11) as follows

$$\boldsymbol{y}_n = \sum_{d=1}^{D} \boldsymbol{A}_{d,n}\boldsymbol{F}\boldsymbol{x}_{d,n} \tag{4.12}$$

$$\boldsymbol{m}_{\boldsymbol{d,n}} = \boldsymbol{M}_{\boldsymbol{d+1,n}}\boldsymbol{x}_{\boldsymbol{d+1,n}} - \boldsymbol{x}_{\boldsymbol{d,n}} \tag{4.13}$$

To recover the cardiac phases $\boldsymbol{x}_{d,n}$, we solve (4.12 and 4.13) by exploiting sparse structure in $\boldsymbol{m}_{d,n}$, and $\boldsymbol{x}_{d,n}$. The process of complete high-resolution image generation is shown in Fig. 4-6.

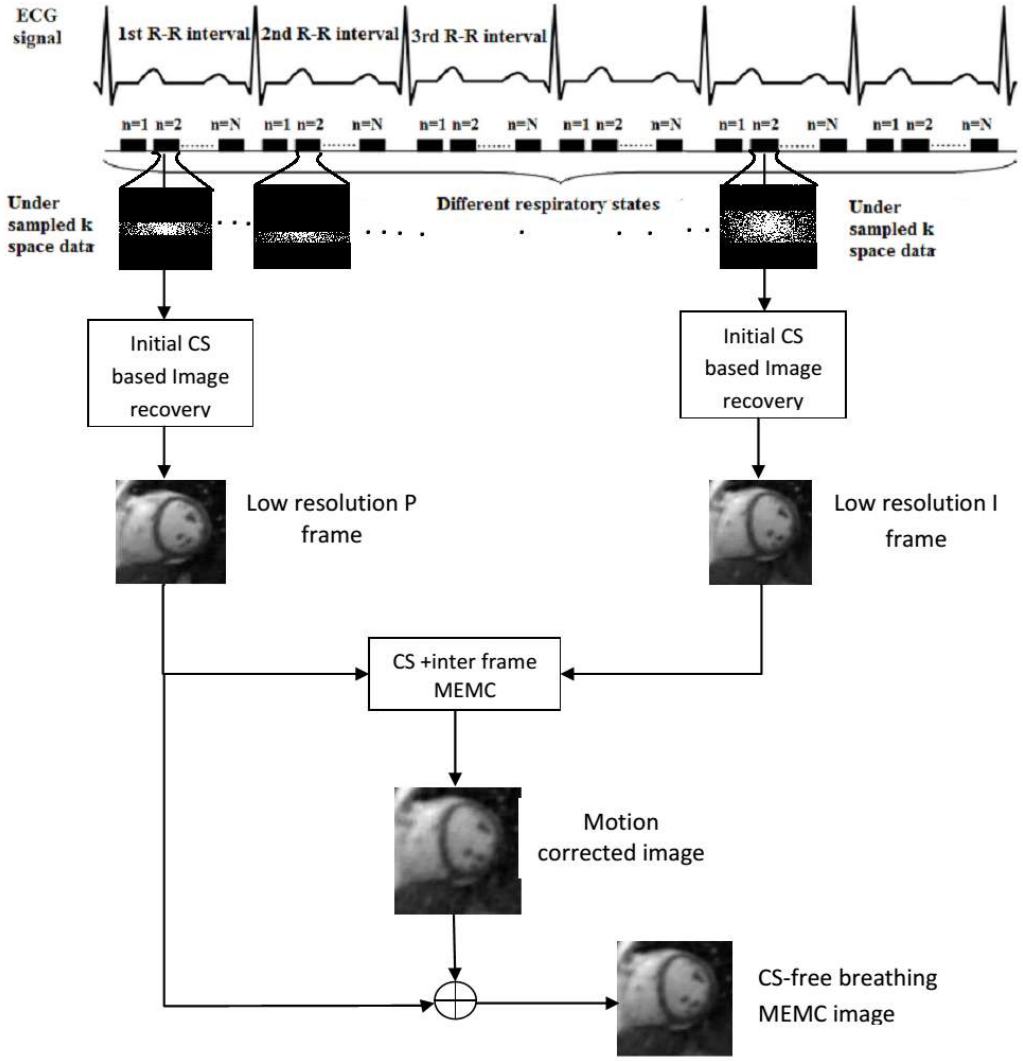

Fig. 4-6 A presentation of initial CS recovery and CS-MEMC recovery steps of the proposed method.

For simplicity, only two heart phases with different respiratory states are shown with six heart beats and *N* cardiac phases. Low resolution *P* and *I* frames are generated by primarily CS. Using ARPS block matching algorithm; motion is estimated and corrected to produce

a motion corrected image. The CS-free breathing MEMC image is generated by combining a low-resolution *P* frame and motion corrected image. The data is acquired in segmented fashion because MRI is a slow imaging modality. During the data scanning process, limited *k*-space samples are recorded at each heart phase in all cardiac cycles. To simulate this condition, each cardiac phase at different respiratory states is multiplied with different sampling matrix $\boldsymbol{A}_{d,n}$

4.4 Cardiac image recovery

A two-step approach is adopted to recover motion free cardiac phases.

4.4.1Initial CS reconstruction

In 1st step, images with motion effects are reconstructed from under sampled *k*-space data independently. For the recovery of dynamic cardiac images, the iterative algorithm of Fig. 4-7 optimizes the cost function given in (4.9) with the approximation given in (4.5). Wavelet based soft threshold is used for the recovery of the N^{th} cardiac phase for each respiratory state. Doubeaches-4 (db4) wavelet is used to exploit the transformed domain sparsity.

4.4.2Inter-frame motion estimation and correction (MEMC)

In the 2nd step inter-frame motion estimation and correction is performed from a pair of CS recovered images, and divided into two sub steps

a. *Motion estimation*: Exploit initially CS reconstructed images to estimate or refine inter-frame motion and the motion transformation $\boldsymbol{M}$ as follows**.** Cardiac phase in the 1st R-R ECG interval is taken as a *P* frame (frame to be predicted) and cardiac phases in subsequent R-R intervals as an *I* frame (reference frame). The *P* and *I* frame is borrowed

terminology from video compression. To estimate the motion between the 2nd cardiac phase of the 1st and 4th R-R interval, for example, we take the 2nd cardiac phase of the 1st interval as a *P* frame and the 2nd cardiac phase at different respiratory state in the 4th R-R interval as an *I* frame.

b. *Motion correction:* After finding motion vectors using ARPS block matching algorithm, we generate the corrected image from *I* frame and with the help of motion vectors. For the refinement of motion corrected image, solve the following optimization problem written for (4.12 and 4.13).

$$\min_{\boldsymbol{x}} f(\boldsymbol{x}_{d,n}) \coloneqq \left\|\boldsymbol{\Phi x}_{d,n} - \boldsymbol{y}_{d,n}\right\|_2^2 + \lambda\left\|\boldsymbol{m}_{d,n}\right\|_1 \tag{4.14}$$

Where $\boldsymbol{m}_{d,n}$is given in (4.13) and its l_1-norm approximation is

$$\left\|\boldsymbol{m}_{d,n}\right\|_1 = \sum_{e=1}^{E}(m_{d,n})_e \tanh\left(\gamma(m_{d,n})_e\right) \tag{4.15}$$

At the final step we generate the image of 2nd cardiac phase by combining P frame and motion corrected image to get an image with high temporal and spatial resolution.

4.4.3 Proposed algorithm

Steps involved in the reconstruction of MR motion corrected images are given in Fig. 4-7

INPUTS

$\boldsymbol{y}_{d,n}, \boldsymbol{y}_{d+1,n}$ **:** *k*-space data

$\boldsymbol{F}$: Fourier Operator

$\boldsymbol{\Psi}$ **:** Sparsifying transform operator

λ = 0.005, η = 0.9, Maxiter = 50

OUTPUT

$\boldsymbol{X}_{d,n}$: Motion corrected final image

INITIALIZATION

$\hat{\boldsymbol{x}}_{d,n} = \boldsymbol{F}^{-1}\boldsymbol{y}_{d,n}, \qquad \hat{\boldsymbol{x}}_{d+1,n} = \boldsymbol{F}^{-1}\boldsymbol{y}_{d+1,n}$

INITIAL CS BASED RECOVERY

Step 1: For $i = 1$: Maxiter

Step 2: Update $\boldsymbol{x}_{d,n}^{i+1} = \hat{\boldsymbol{x}}_{d,n}^{i} - \eta \nabla f\left(\hat{\boldsymbol{x}}_{d,n}^{i}\right)$

Step 3: Shrinkage: $\hat{\boldsymbol{x}}_{d,n}^{\boldsymbol{i+1}} = \boldsymbol{\Psi}^{-1}\left\{T_{\lambda}\left(\boldsymbol{\Psi}\boldsymbol{x}_{d,n}^{i+1}\right)\right\}$(Using (4.9))

Step 4: End (i) Return $\boldsymbol{x}_{d,n}$

Repeat step 1 to 4 for recovery of $\boldsymbol{x}_{d+1,n}$

MOTION ESTIMATION AND COMPENSATION

Step 5: For j=1:*Maxiter* do

If j=1

Step 6: Find motion compensated image $\hat{\boldsymbol{x}}_{d,n}^{\boldsymbol{j}}$ for $\boldsymbol{x}_{d,n}$ and $\boldsymbol{x}_{d+1,n}$

Else

Step 7: Refine motion between $\hat{\boldsymbol{x}}_{d,n}^{\boldsymbol{j}}$ and $\boldsymbol{x}_{d+1,n}$

End (Else)

Step 8: Update $\boldsymbol{x}_{d,n}^{j+1} = \hat{\boldsymbol{x}}_{d,n}^{j} - \eta \nabla f\left(\hat{\boldsymbol{x}}_{d,n}^{j}\right)$

Step 9: Shrinkage: $\hat{\boldsymbol{x}}_{d,n}^{\boldsymbol{j+1}} = \boldsymbol{\Psi}^{-1}\left\{T_{\beta}\left(\boldsymbol{\Psi}\boldsymbol{x}_{d,n}^{j+1}\right)\right\}$(Using (4.9))

End (j) Return refined image $\ddot{\boldsymbol{x}}_{d,n}$

Step 10: $\boldsymbol{X}_{d,n} = \ddot{\boldsymbol{x}}_{d,n} + \boldsymbol{x}_{d,n}$

Fig. 4-7 Proposed algorithm

4.4 Simulation and results

The proposed method was tested on simulated data generated by the MRXCAT framework [95], and on fully sampled, free-breathing, cine MRI data. The recovered images for CS-free breathing motion corrected was compared with CS-free breathing images and with CS-breath held images. All CS images were recovered in MATLAB (R2012a, MathWorks Inc., Natick, MA) using the proposed hyperbolic tangent based surrogate function to solve the non-differentiability problem of the l_1-norm penalty. In the Gradient decent algorithm,

step size η in an update equation was chosen empirically. Parameter values used in the algorithm are $\lambda = 0.005$, $\eta = 0.9$ and $\gamma \geq 10$. The same values for λ, η and γ were used for initial CS reconstruction and for the final inter-frame motion estimation and compensation.

The Structural similarity index (SSIM) [96], peak signal to noise ratio (PSNR) and mean square error (MSE) given in chapter 2 was used for quantitative comparison between CS-free breathing reconstruction with and without motion correction. The ARPS block matching algorithm was used for inter-frame respiratory motion estimation between the reference image and the current image. Diastolic, middle of systolic and diastolic and systolic heart phases at different respiratory states were used for both simulated images and clinical data.

The MRXCAT, a Matlab software for numerical simulation of cardiac MRI, is used for generating free breathing and breathe held images. For the MRXCAT, the following parameters were used: reconstruction matrix size: 256 × 256, 24 cardiac phases in the presence of respiratory motion, with an image resolution of 1×1×1 mm^3, TE=1.5ms, TR=3ms and flip angle = 60^o. In real free breathing cardiac cine MRI, fully sampled ECG-gated data was acquired on a Philips 1.5 T scanner (b-SSFP). Reconstruction matrix size: 256 × 256, 6 cardiac cycles with 24 cardiac phases in each cycle and an image resolution of 2.5×2.5×8 mm^3 was used.

For comparison of proposed method with k-t FOCUSS we used following data: a short-axis MRI scan was acquired using a GE 1.5T twin speed scanner (R12M4) with a 5-element cardiac coil and a FIESTA/Fast CARD cine SSFP sequence. Scan parameters were selected as follows: TE: 2.0 ms, TR: 4.1 ms, flip angle: 45◦, FOV: 350 × 350 mm, slice thickness:

12 mm, 8 views per segment, 224 phase-encoding lines, 256 read-out samples, and 16 temporal frames. To emulate the estimation of sensitivity maps from a pre scan, we acquired a separate scan (which we assume to be a pre scan) with identical scan parameters and estimated sensitivity maps as follows: Half of the (high frequency) *k*-space samples from each coil were removed from the pre scan via a smoothing filter followed by an inverse Fourier transform to obtain smoothed images for each coil. To estimate the sensitivity maps, we divided each smoothed coil image by the sum of squares of all coil images.

The acquired data were retrospectively under-sampled for acceleration rates $R = 2$ (50% samples), 3 (33% samples) and 8 (12.5% samples) using variable-density random under-sampling method. Sampling masks for different acceleration rates are shown in Fig. 4-8. The sampling mask randomly selects more samples from the low frequencies of the *k*-space data and fewer samples from the high frequencies of the *k*-space data.

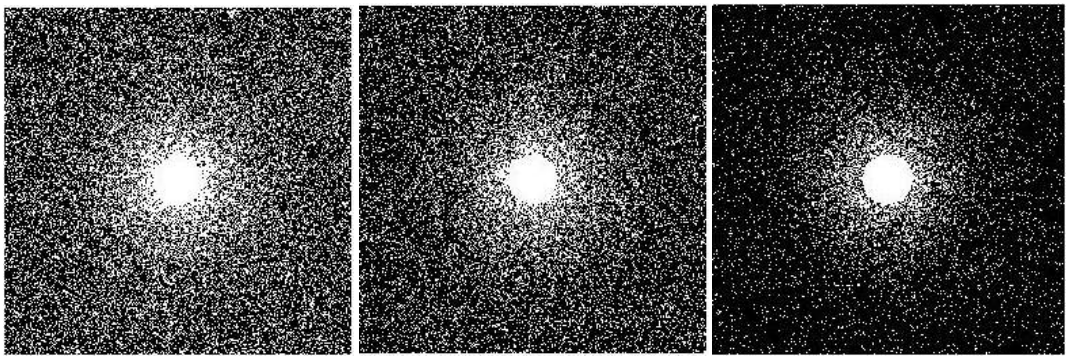

(a) **(b)** (c)

Fig. 4-8 Variable density sampling patterns for different acceleration rates (*R*) a) $R = 3$, b) $R = 4$, c) $R = 8$

Fig. 4-9 provides a comparison of the CS-free breathing motion corrected (CS+MEMC), CS-free breathing (CS+no MEMC) and breath held for the short axis MRI images

generated from the MRXCAT simulation software at the acceleration rate 2 and 8. Fig. 4-9(a) illustrates frame 1, 5 and 12 out of 24 frames in a sequence, produced from fully sampled breath held *k*-spaced data. Most of the changes occur in the heart region, enclosed in the white box in (a), and is taken as a region of interest (ROI). Fig. 4-9(b) shows the ROI, specifying left and right ventricles with endocardium and epicardium. Fig. 4-9(c) and (e) shows proposed method recovery (CS+MEMC) at the acceleration rates 2 and 8, respectively. Fig. 4-9 (d) and (f) represents the difference between breath held and estimated images for the proposed method. Fig. 4-9(g) and (i) show CS+no

MEMC at the acceleration rates 2 and 8, respectively. Fig. 4-9 (h) and (j) represents the difference between breathe held and estimated images with CS+no MEMC. Images recovered by the proposed method shows significant improvement as compared to the image recovery without MEMC at both acceleration rates. Motion artifacts like ghosting and blurring can be seen in Fig. 4-9(g) and (i) pointed by the black arrows. The Proposed method eliminated ghosting and blurring effects and achieved high spatial and temporal accuracy as shown in Fig. 4-9(c) and (e). The elimination of motion artifacts provides sharp endocardium and epicardium borders. This sharpness is very important in the clinical interpretation of ventricular dynamics. The improved recovery of the proposed method is also evident from difference images. Fig. 4-10 presents the comparison of the proposed method and CS+no MEMC for the short axis MRI images at the acceleration rate 3 and 8. Fig. 4-10(a) illustrates complete data set of a diastolic, middle of diastolic and systolic and systolic frames in a sequence, produced from clinically observed fully sampled k-spaced data.

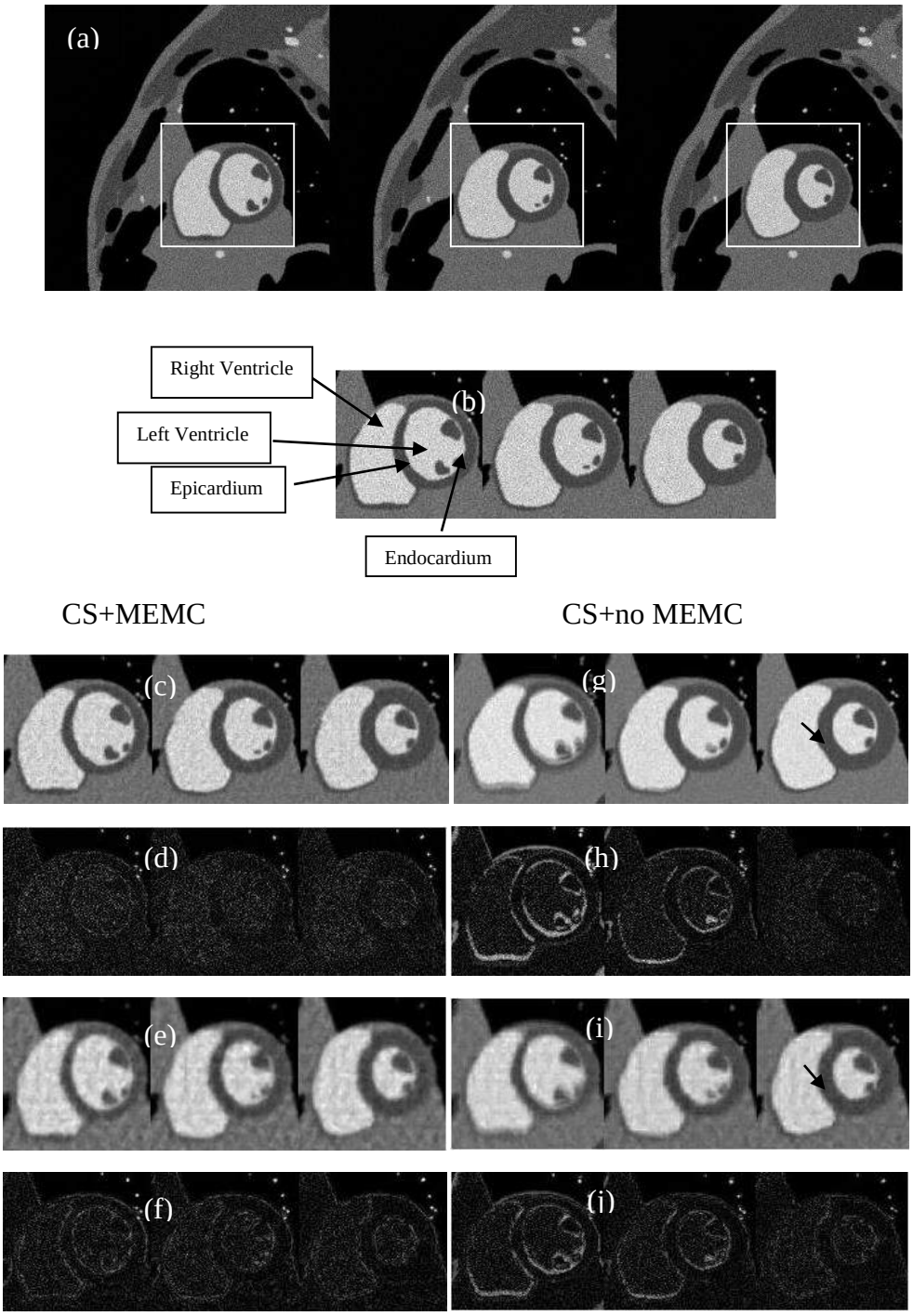

Fig. 4-9 Comparison of recovered images with and without respiratory motion estimation for simulated data: frames 1, 5 and 12 (left to right).**a)** Gold standard images from full k-space breath held data. **b)** Spatial region of interest (ROI). **Left column**: **c)** Reconstruction using the proposed technique (CS+MEMC) at $R = 2$**d)** Difference between estimated image (c) and (b).**e)** Reconstruction using the proposed technique (CS+MEMC) at $R = 8$. **f)** Difference between estimated image (e) and (b). **Right**

column: g) Reconstruction with CS+no MEMC at $R = 2$.**h)** Difference between estimated image (g) and (b).**i)** Reconstruction CS+no MEMC at $R = 8$. **j)** Difference between estimated image (i) and (b).

Fig. 4-10(b) shows the ROI, enclosed in rectangular box in (a), representing left, right ventricle and epicardium and endocardium. Fig. 4-10(c) and (e) shows the proposed method recovery at acceleration rates 3 and 8, respectively. The results of CS-free breathing without MEMC at acceleration rates 3 and 8 are illustrated in Fig. 4-10(g) and (i) respectively. The systolic phase recovered by proposed method in (c) and (e) is very close and clear to fully sampled ROI in (b) as compared in (g) and (i) where the images are not only ghosted and blurred, the heart walls are also displaced from their true location. Sharpness of epicardium and endocardium is also prominently visible in images recovered through proposed method. Fig. 4-11 illustrates the comparison of the proposed method (CS+MEMC) and k-t FOCUSS with MEMC for the short axis MRI dataset at acceleration rate 4. Fig. 4-11(a) shows frames 1, 13, and 10 (from left to right) out of the 16 frames in the sequence, calculated from the fully sampled breath held *k*-space data. Using k-space tutorial [97], motion-corrupted images are generated from the short axis MRI dataset. Fig. 4-11(b) present proposed technique reconstructions at acceleration rates 4. The results for k-t FOCUSS with MEMC at acceleration rates 4 is presented in Fig. 4-11(c). The proposed method reconstruction shows significant improvement and less random noise than k-t FOCUSS with MEMC reconstruction. Furthermore, k-t FOCUSS with MEMC reconstructions contain motion artifacts (visible with bright regions), while the proposed method reconstructions are much cleaner.

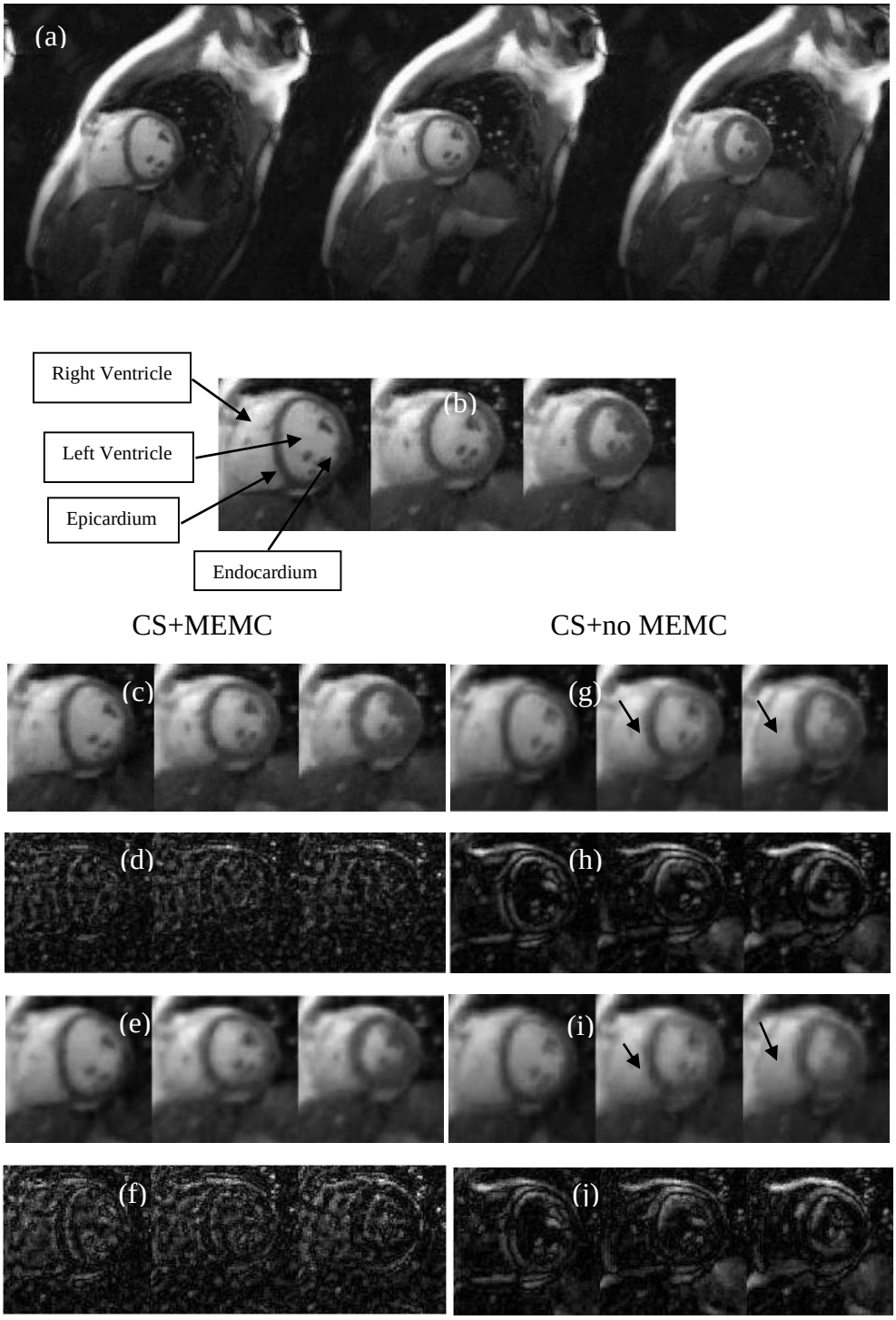

Fig. 4-10 Comparison of recovered images with and without respiratory motion estimation for clinical data: frames diastolic, middle of diastolic and systolic and systolic (left to right). **a)** Gold standard images from full *k*-space data. **b)** ROI. **Left column**: **c)** Reconstruction using the proposed technique (CS+MEMC) at $R = 3$ **d)** Difference between estimated image (c) and (b). **e)** Reconstruction using the proposed technique (CS+MEMC) at $R = 8$. **f)** Difference between estimated image (e) and (b) **Right**

column: g) Reconstruction with CS+no MEMC at $R = 3$. **h)** Difference between estimated image (g) and (b).**i)** Reconstruction CS+no MEMC at $R = 8$. **j)** Difference between estimated image (i) and (b).

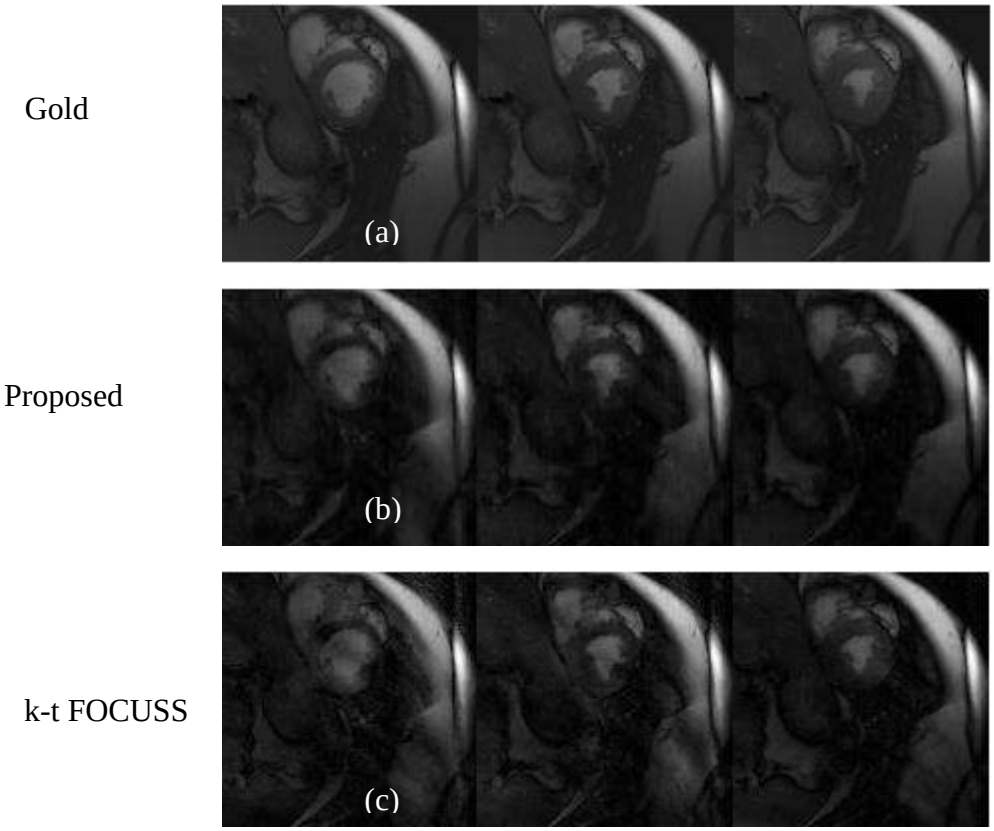

Fig. 4-11 Comparison of recovered images in pixel domain for proposed method and k-t FOCUSS with MEMC data at a acceleration rate of 4.**a)** Fully sampled breath held k-space data **b)** Recovered images with proposed method **c)** Reconstructed images for k-t FOCUSS with MEMC

Table 4.1, Table 4.2, and Table 4.3 provides a comparison of the proposed method and k-t FOCUSS for performance metrics such as SSIM, PSNR and MSE. The numerical values of metrics for selected frames 1, 10 and 13 show that the proposed method outperforms k-t FOCUSS with MEMC.

Table 4.1 SSIM Comparison for proposed method and k-tFOCUSS with MEMC

Technique	Diastolic(Frame #1)	Systolic (Frame #10)	Middle(Frame #13)
Proposed Method	0.7319	0.8687	0.8260
k-t FOCUSS	0.7004	0.8368	0.7302

Table 4.2 PSNR (db) Comparison for proposed method and k-t FOCUSS with MEMC

Technique	Diastolic(Frame #1)	Systolic (Frame #10)	Middle(Frame #13)
Proposed Method	29.9443	34.2610	31.1526
k-t FOCUSS	25.4316	32.3289	26.2374

Table 4.3 MSE Comparison for proposed method and k-t FOCUSS with MEMC

Technique	Diastolic(Frame #1)	Systolic (Frame #10)	Middle(Frame #13)
Proposed Method	0.001	3.7488e-4	7.6690e-4
k-t FOCUSS	0.002	5.8494e-4	0.0024

A plot for PSNR at different acceleration rates for CS-free breathing and CS-free breathing motion corrected is shown in Fig. 4-12. It is drawn for recovered images shown in Fig. 4-10. Dashed lines denote PSNR over the ROI and the solid line shows over the entire image. The curves show that CS-free breathing motion corrected (proposed method) is far better than the CS-free breathing at all acceleration rates for both the full reconstruction and the reconstructions of ROI. Even at higher acceleration rate like 12, PSNR for ROI is 4db better in CS-free breathing with MEMC as compared to CS-free breathing without MEMC.

To show how the recovered images, with and without MEMC are similar to the fully sampled images, we used SSIM. A plot for SSIM at different acceleration rates for CS-free breathing and CS-free breathing motion corrected is shown in Fig. 4-13. The plot is drawn for clinical data of Fig. 4-10. Solid lines denote SSIM over the ROI and dashed line shows

over the entire image (Full image). The curves illustrate that the images recovered with the proposed method are more similar to a gold standard as compared to CS-free breathing without MEMC at all acceleration rates.

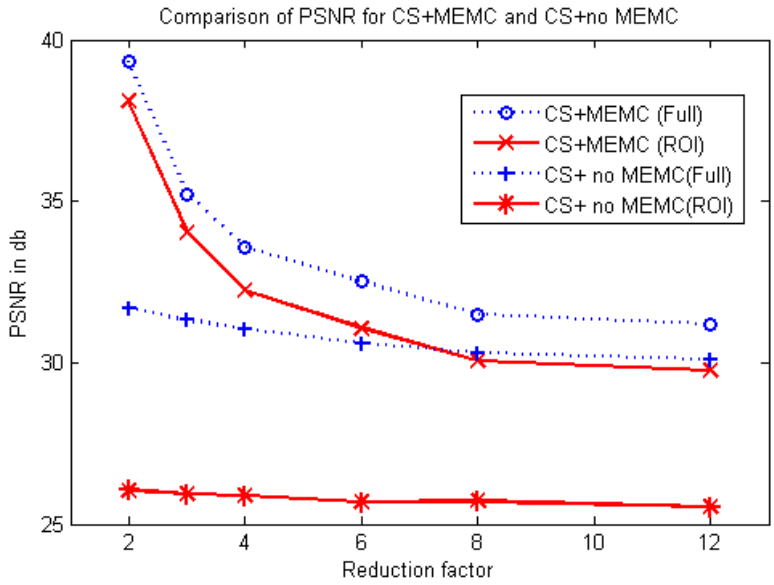

Fig. 4-12 Performance comparison of PSNR at different acceleration rates for CS-free breathing (CS+no MEMC) and CS-free breathing motion corrected (CS+MEMC). Dashed lines depict PSNR over the full image and solid lines shows PSNR in the region of interest (ROI).

A plot for reconstruction mean square error (MSE) at different acceleration rates for CS-free breathing and CS-free breathing motion corrected is illustrated in Fig. 4-14. The plot is drawn for clinical data of Fig. 4-10. Solid lines denote MSE over the ROI and dashed line shows over the entire image. The curves illustrate that images recovered with proposed method have smaller MSE in comparison with CS-free breathing without MEMC at all acceleration rates for both entire region and ROI.

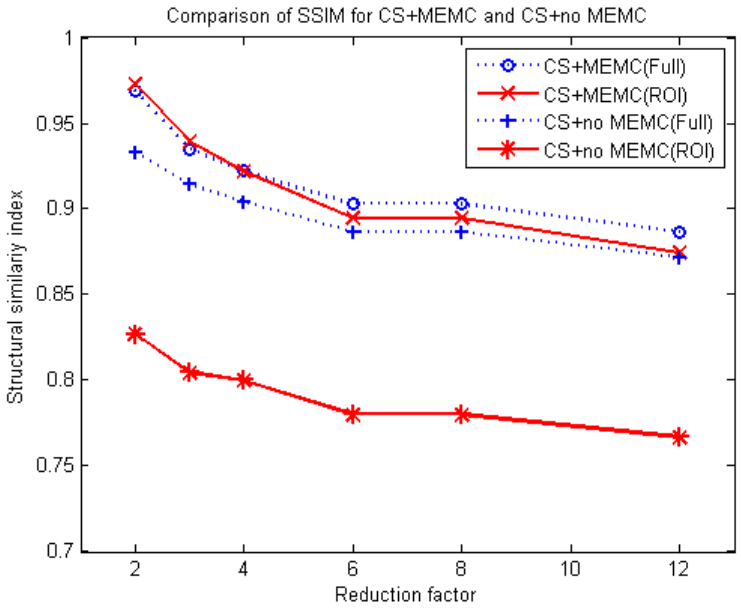

Fig. 4-13 Performance comparison of SSIM at different acceleration rates for CS-free breathing without MEMC and CS-free breathing with MEMC. Dashed Lines depicts SSIM over the full image and solid lines shows SSIM in the region of interest (ROI).

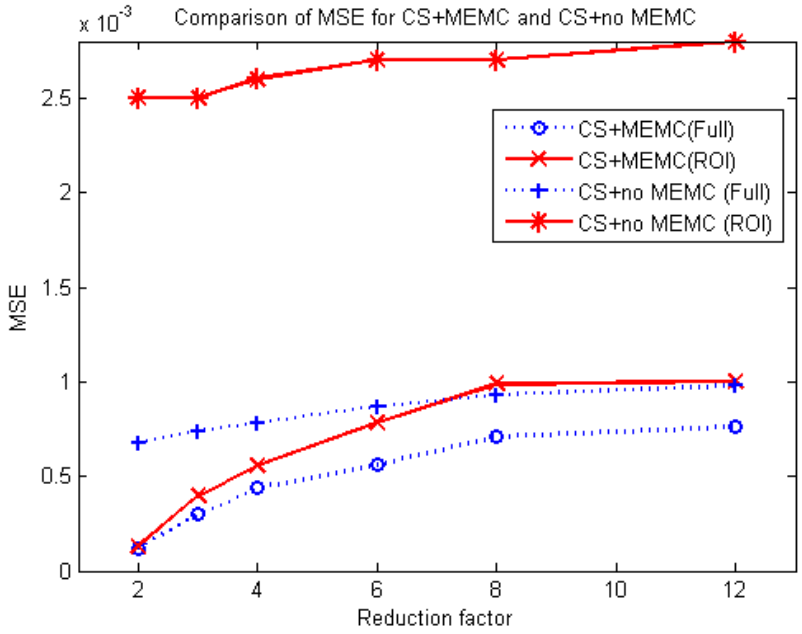

Fig. 4-14 Performance comparison of MSE at different acceleration rates for CS-free breathing and CS-free breathing motion corrected. Dashed Lines depicts MSE over the entire region and solid lines with MSE in the region of interest (ROI).

4.5 Summary

First section of the chapter presented a comparison of surrogate functions used to approximate the absolute value function used in l_1-norm. Simulation results show hyperbolic tangent function shows robustness in noisy environment and performs better for different acceleration rates since it yields improved image recovery in terms of SSIM. Fast convergence and lower RMSE is also observed for hyperbolic tangent function. Flexibility of varying parameters λ and γ is an extra facility to adjust the slop of function. The second section proposed a method for respiratory motion correction in ECG gated free breathing cardiac MRI. Inter-frame motion estimation was used to estimate the respiratory motion between the same cardiac phases, but at different respiratory states. The block matching algorithm was used for MEMC. A Gradient decent algorithm based on flexible l_1-norm approximation was used for the recovery of MR images free from motion artifacts and close to the true MR images. Standard metrics like SSIM, PSNR and MSE at different acceleration rates were observed superior for the proposed method as compared to the results obtained without MEMC and k-t FOCUSS

Chapter 5

Recovery of Compressively Sampled MR Images Using Motion Adaptive Wavelet Threshold

Iterative shrinkage algorithms like Parallel Coordinate Descent (PCD) and Separable Surrogate Functional (SSF) use wavelet threshold with uniform and empirically selected threshold values to recover the sub-sampled MR images. This chapter discusses a new idea of adaptive threshold for the reconstruction of compressively sampled static and dynamic MR images. The derivation of parameter as well as an iterative shrinkage algorithm based on derived threshold is presented in details. The threshold parameter continuously changes its value based on the dynamics of the MR images to be recovered. The algorithm and the derived adaptive threshold is experimentally tested for static and dynamic MR images with varying acceleration rates and it has been shown that it outperforms the fixed threshold value algorithm.

5.1 Introduction

Transformed domain sparsity and Fourier encoded nature of MR imaging makes MRI a possible candidate for the application of CS theory [4]. Algorithm development for the CS recovery of sub-sampled MR images is an active area of research in the sparse signal processing community. Reconstruction of MR images based on a nonlinear conjugate gradient and Bregman iteration method is discussed in[4, 98]. However, these algorithms are not feasible for real images with higher dimensions. Iterative shrinkage threshold (IST)

and fast IST[99, 100], another group of algorithms, efficiently recover MR images from under-sampled *k*-space data by minimizing a cost function given in (2.15) with the thresholding step as a main ingredient.

Use of threshold is a simple idea for denoising or equivalently for CS based reconstruction but selection of threshold parameter in algorithms is not an easy task. Different variants of IST [93, 101] use a fixed and uniform threshold values, selected empirically, in shrinkage step to recover MR images from wavelet coefficients. References [102-104] discuss image de noising using wavelet threshold and propose a spatially adaptive threshold value that is a function of noise and image statistics. Use of uniform threshold parameter does not provide the benefit of selecting important signal feature and rejecting noise coefficients simultaneously [103].

The IST algorithms [93, 105, 106] and the algorithm discussed in chapter 4 considers $S_\lambda(\boldsymbol{x})$, given in (4.7), with a fixed and empirically selected threshold parameter λ which is in appropriate for the following reasons:

1. The wavelet domain coefficients of images are peaked at zero but do not follow exactly Laplacian distribution.
2. Fixed λ is not appropriate for the images that are changing with time.
3. In a CS recovery problem, fixed λ needs to be changed for different acceleration rates to get better recovery results.

Flexible soft thresholding function[105], based on different adjustable parameters, solve the above problems up to some extent by changing the values of parameters. Another technique discussed in this chapter to solve the above mentioned problems in CS recovery

is to replace the fixed threshold value λ with an adaptive or data driven parameter that depends upon the statistics of wavelet coefficients.

5.2 Adaptive threshold

Exploiting the concept of denoising, based on adaptive wavelet thresholding [102, 103], the data driven threshold value λ_{adap} is derived using maximum a posterior (MAP) estimator as follows. Let the observed signal, in wavelet domain, is given as

$$\boldsymbol{r} = \boldsymbol{z} + \boldsymbol{v} \tag{5.1}$$

Where the random vectors $\boldsymbol{r} = \boldsymbol{\Psi}\mathbf{y}$ and $\boldsymbol{z} = \boldsymbol{\Psi}\mathbf{x}$ are the wavelet coefficients of the noisy observations and noise-free image respectively and$\boldsymbol{v} = \boldsymbol{\Psi}\boldsymbol{\varepsilon}$ with $\boldsymbol{\varepsilon}$ is independent and identically distributed $\mathcal{N}(0, \sigma^2)$ noise . Since $\boldsymbol{\Psi}$is orthogonal, $\boldsymbol{v}$ is also Gaussian and normally distributed. The (MAP) estimator for the random vector $\boldsymbol{z}$ is given by:

$$\hat{\boldsymbol{z}} = \operatorname{argmax}_{\boldsymbol{z}} p(\boldsymbol{z}|\boldsymbol{r})$$

Applying Baye's rule and ignoring $p(\boldsymbol{r})$, the MAP estimator takes the form:

$$\hat{\boldsymbol{z}} = \operatorname{argmax}_{\boldsymbol{z}} p(\boldsymbol{r}|\boldsymbol{z}) p_{\boldsymbol{z}}(\boldsymbol{z}) \tag{5.2}$$

Using simple mathematics starting with$p(\boldsymbol{r}|\boldsymbol{z}) = p_{\boldsymbol{v}}(\boldsymbol{r} - \boldsymbol{z})$ following expression is derived

$$= \operatorname{argmax}_{\mathbf{z}} \left[-\frac{\|\boldsymbol{r}-\boldsymbol{z}\|_2^2}{2\sigma_v{}^2} + g(\boldsymbol{z}) \right] \tag{5.3}$$

where $g(\boldsymbol{z}) = ln\, p_{\boldsymbol{z}}(\boldsymbol{z})$. Maximum of the cost function in (5.3) is obtained by differentiating the argument of (9) w.r.t. $\boldsymbol{z}$ and equating the result to zero that is

$$\frac{(r_i - \hat{z}_i)}{\sigma_v{}^2} + g'(\hat{z}_i) = 0,\ 1 \le i \le N \tag{5.4}$$

For a large class of natural and biomedical images, the wavelet domain coefficients are symmetrically distributed and are sharply peaked at the centre[107, 108]. In this paper we assume the distribution of transformed domain coefficients be Laplacian i.e.

$$p_z(z_i) = \frac{1}{\sqrt{2}\sigma_z} e^{\frac{\sqrt{2}}{\sigma}|z_i|}$$

gives $g'(\hat{z}_i) = -\frac{\sqrt{2}}{\sigma_z} sgn(\hat{z}_i)$. Solving (5.4) results in

$$r_i = \hat{z}_i + \frac{\sqrt{2}{\sigma_v}^2}{\sigma_z} . sgn(\hat{z}_i) \tag{5.5}$$

To find $\hat{z}_i$, solve (5.5) for $\hat{z}_i$ to get the nonlinear shrinkage:

$$\hat{z}_i(r) = S_\lambda(r) = \max\{|r| - \lambda, 0\} . sgn(r) \tag{5.6}$$

with λ, adaptive and data driven threshold, is given by the following relationship

$$\lambda = \frac{\sqrt{2}{\sigma_v}^2}{\sigma_z} \triangleq \lambda_{adap} \tag{5.7}$$

where σ_z is the standard deviation of an image in the wavelet domain, and σ_v is thestandard deviation of Gaussian like noise artifacts. The threshold parameter is data dependent and has an intuitive appeal. The normalized threshold parameter $\frac{\lambda_{adap}}{\sigma_v}$ has an inverse relationship with σ_z , the standarddeviation of $\boldsymbol{z}$, and direct relationship with σ_v , the noise standard deviation. When$\sigma_v/\sigma_z \ll 1$, the image features are much stronger than the noise, thusλ_{adap}/σ_v is chosen to be small to preservemost of the image features and remove some of the noise, and when$\sigma_v/\sigma_z \gg 1$, the noise dominates and the normalized threshold is chosen to be large to remove the noise. In this paper we used the shrinkage function in (5.6) for sparse signal recovery with the threshold parameter derived in (5.7).

5.3 CS-MRI and proposed algorithm

Different techniques like parallel imaging[1], reduction in repetition time (TR) and non-Cartesian sampling[4]with their own limitations have been used to reduce the MRI scan time. CS, an algorithmic reduced MR acquisition technique, exploits transformed domain sparsity for the recovery of under-sampled MR images. The sparsity of static and dynamic MR images can be observed as a sharp peak of coefficients in wavelet domain and is shown in Fig. 5-1 for brain and systolic heart phase. To recover a good quality image, CS technique requires: i) the image to be recovered has sparse structure in some transform domain ii) the under-sampling effect of *k*-space be incoherent in that transform domain iii) a nonlinear reconstruction procedure. In case of MRI, the CS reconstruction algorithm minimizes the following cost function, a modified version of (2.15)

$$f(\boldsymbol{x}) = \frac{1}{2}\|\mathbf{F}_{\boldsymbol{u}}\boldsymbol{x} - \boldsymbol{y}\|_2^2 + \lambda\|\boldsymbol{z}\|_1 \tag{5.8}$$

where $\mathbf{F_u}$ denotes the partial Fourier transform, $\boldsymbol{z} = \boldsymbol{\Psi x}$, and $\boldsymbol{y}$ is the under-sampled *k*-space data.

In CS, there is a strong connection between under-sampling and additive Gaussian noise. Random under-sampling of Fourier encoded images introduces noise in the linear reconstructed images that can be modeled by the Gaussian distribution. The actual down sampling noise depends on a sampling mask used for the under-sampling of MR image. For the variable density under-sampling mask used in our simulation, noise histogram (in pixel domain) is shown in Fig. 5-2. The error is obtained as follow

$$\boldsymbol{e} = \boldsymbol{x} - \hat{\boldsymbol{x}}$$

$\hat{\boldsymbol{x}}$ is the recovered or denoised image.

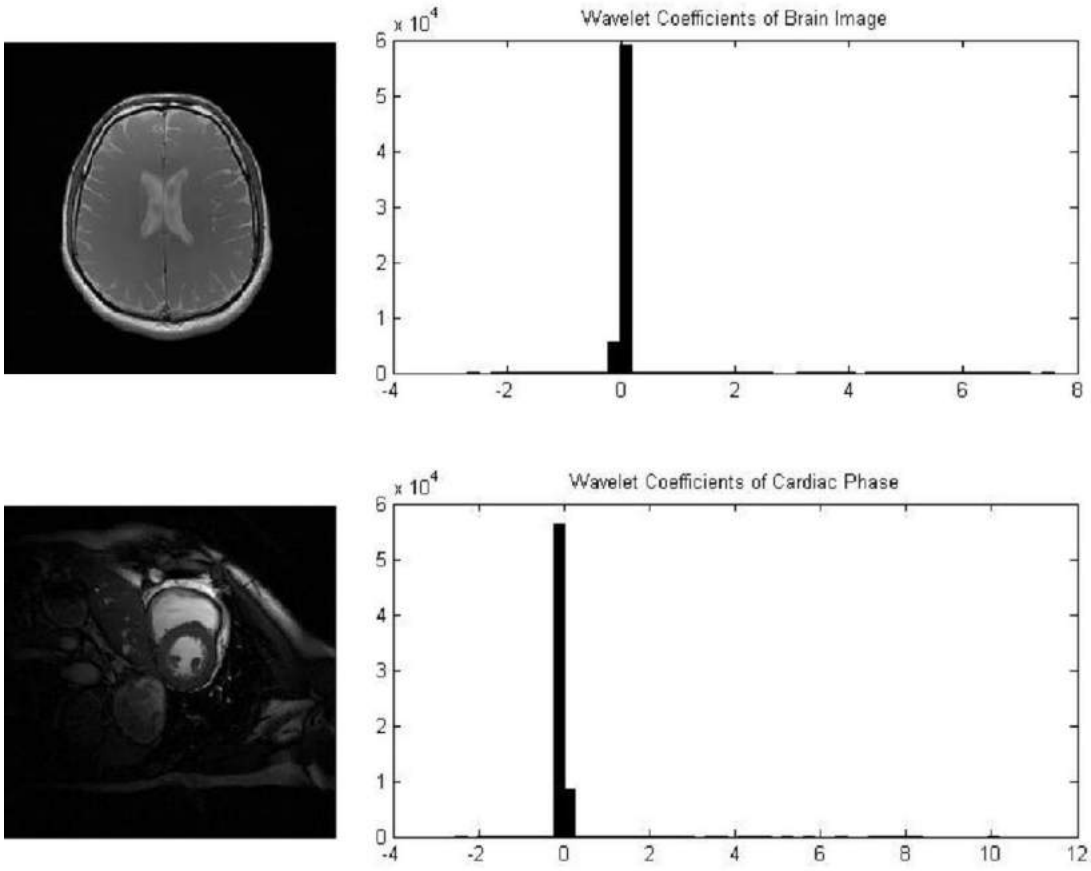

Fig. 5-1 Wavelet coefficients histograme for brain and systolic cardiac phase MR images.

Iterative shrinkage threshold (IST) algorithms improve reconstructed image quality iteratively from under-sampled k-space data with fixed threshold value. To cater for the problems due to fixed threshold parameter, the threshold value during iteration must be adaptively updated to reconstruct the best image. The proposed adaptive threshold parameter λ_{adap} can be used with any iterative shrinkage algorithm. In this article, however, we take iterative algorithm presented in [93] with the complete description given in Fig. 5-3. Inverse Fourier-transformed values, obtained from zero-filled k-space data, are used to initialize the algorithm. To improve the quality of images, the algorithm iteratively computes the Gradient of the cost function and applies the shrinkage in wavelet domain.

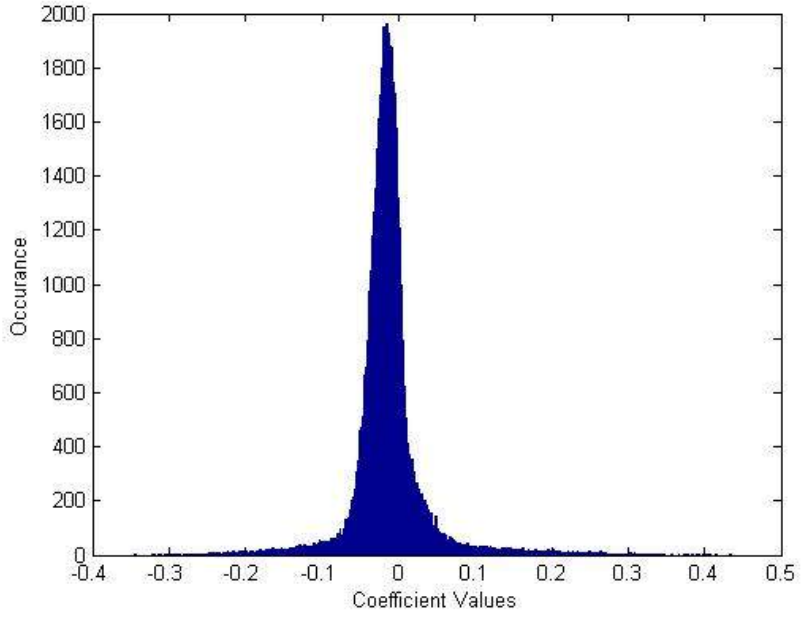

Fig. 5-2 Histogram of Gaussian like noise

Instead of using fixed and empirically selected threshold value, an adaptive threshold value derived in (5.7) is used in the algorithm.

Input: Under sampled *k*-space data $\mathbf{y} = \mathbf{\Phi x} \in R^M$, parameters η,$\gamma$and λ_{ini}, i_{max}

Output: Reconstructed image vector $\hat{\boldsymbol{x}} \in R^N$

Initialization: Select $\boldsymbol{x}_{ini} = \boldsymbol{F}^{-1}(\boldsymbol{y})$.where $\boldsymbol{F}^{-1}$ is inverse Fourier transform

$\boldsymbol{x}^{\mathbf{i}} = \boldsymbol{x}_{\mathbf{ini}}$

If i=0

$\lambda=\lambda_{ini}$, otherwise $\lambda=\lambda_{adap}$

Step-1 Find $\nabla f\left(x_l^i\right)$of (4.8) using (4.9)

Step-2 Compute x_l^{i+1}using (4.6)

Step-3 Compute wavelet coefficients of $\boldsymbol{x}_{ini}$ i.e $\boldsymbol{z}_{ini} = \mathbf{\Psi} \boldsymbol{x}_{ini}$

Step-4 Compute wavelet coefficients of $\boldsymbol{x}^{i+1}$i.e $\mathbf{z}^{i+1} = \mathbf{\Psi} \boldsymbol{x}^{i+1}$

Step-5 Compute the error $\boldsymbol{e} = \boldsymbol{z}_{ini} - \mathbf{z}^{i+1}$

Step-6 Compute noise power σ_v^2 using error $\boldsymbol{e}$

Step- 7 Compute $\sigma_{z^{i+1}}$ using $\mathbf{z}^{i+1}$

Step-8 Compute adaptive threshold i.e. $\lambda_{adap} = {\sigma_v^2}/{\sigma_{z^{i+1}}}$

Step-9 (Soft Thresholding in wavelet domain): Estimate Solution $\hat{\boldsymbol{x}}_{\boldsymbol{i}}$ using $\hat{\boldsymbol{x}}^{\boldsymbol{i}} = \boldsymbol{\Psi}^{-1} S_{\lambda}(\mathbf{z}^{i+1})$ where $S_{\lambda}(\mathbf{z}^{i+1})$ is given in (5.6)

Step-10 **(Repeat)**: For number of maximum iteration ($i_{\max}$)

Output: Reconstructed $\hat{\boldsymbol{x}} = \hat{\boldsymbol{x}}^{\boldsymbol{i}}$

Fig. 5-3 Proposed algorithm

The stopping criteria could be a fixed number of iteration and or some desired value of $\|\mathbf{F}_{\boldsymbol{u}}\boldsymbol{x} - \boldsymbol{y}\|_2^2$

5.4 Simulation results and discussion

The proposed algorithm and adaptive threshold value is tested for the recovery of a brain and cardiac MR data. In the first experiment, the proposed algorithm recovers a brain image data from partial Fourier coefficients (*k*-space data). The image is under-sampled by taking 12.5% samples from complete *k*-space data using variable density sampling pattern. To sparsify the MR image, doubechies-4 (db4) wavelet is used. To keep the acquired *k*-space samples unchanged, during iteration, a data-consistency step is incorporated in the algorithm. The image recovery process is completed using 25iterations of the algorithm. The parameter values of η=0.9 and γ= 50 are used and the adaptive threshold value is initially chosen as 0.023 and updated during each iteration. The fix threshold value of λ= 0.02, chosen for comparison, is same as taken in[93].

The Human brain image used in experiment acquired through 1.5 Tesla GE HDxt scanner with an eight-channel head coil and a gradient echo sequence at St. Mary's Hospital London. Other specifications were: matrix size = 256 x 256, flip angle = 90^o, slice thickness

= 3mm, bandwidth = 31.25 KHz, Field of view (FOV) = 20 cm, TR/TE =55/10 msec. The variable density sampling mask used in all simulation with an acceleration factor of 8and an original head MRI is shown in Fig. 5-4.

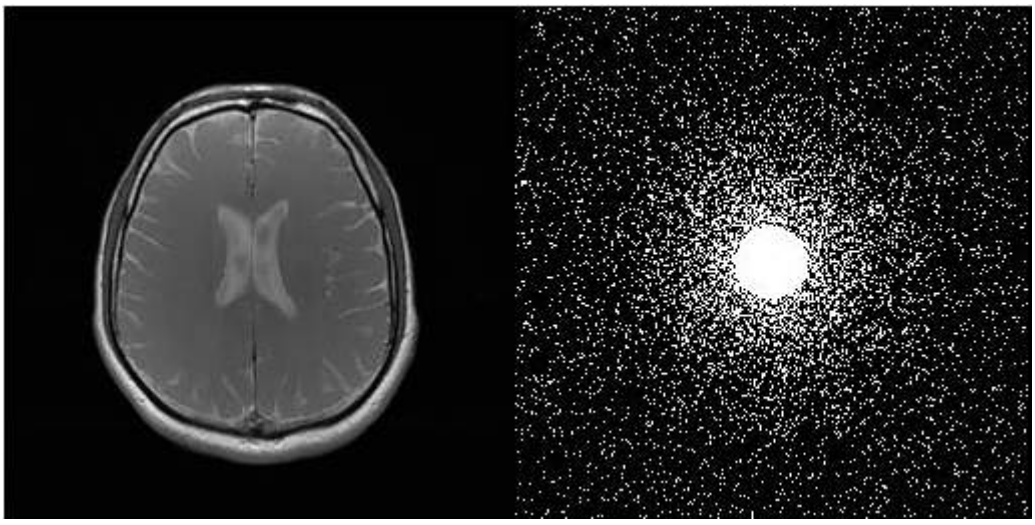

Fig. 5-4 Original head MRI with the variable density sampling pattern

Fig. 5-5 presents a comparison of the reconstructed image quality between proposed algorithm with the adaptive threshold parameter and an algorithm with fixed threshold parameter. It is clear from five times amplified difference between original and recovered images that the proposed algorithm recovers an image with the superior quality as compared to fixed threshold value based algorithm.

Fig. 5.6 provides a performance measurement plots for standard matrices of SSIM, PSNR and correlation of recovered brain MR images using proposed algorithm. A Similar under-sampling pattern and initial zero filled (ZF) image is

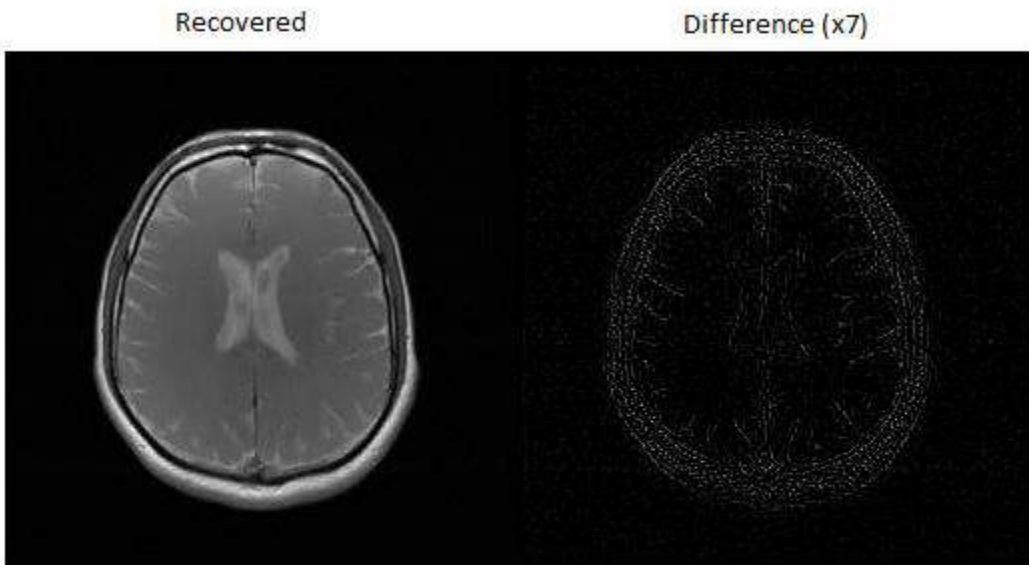

(a)

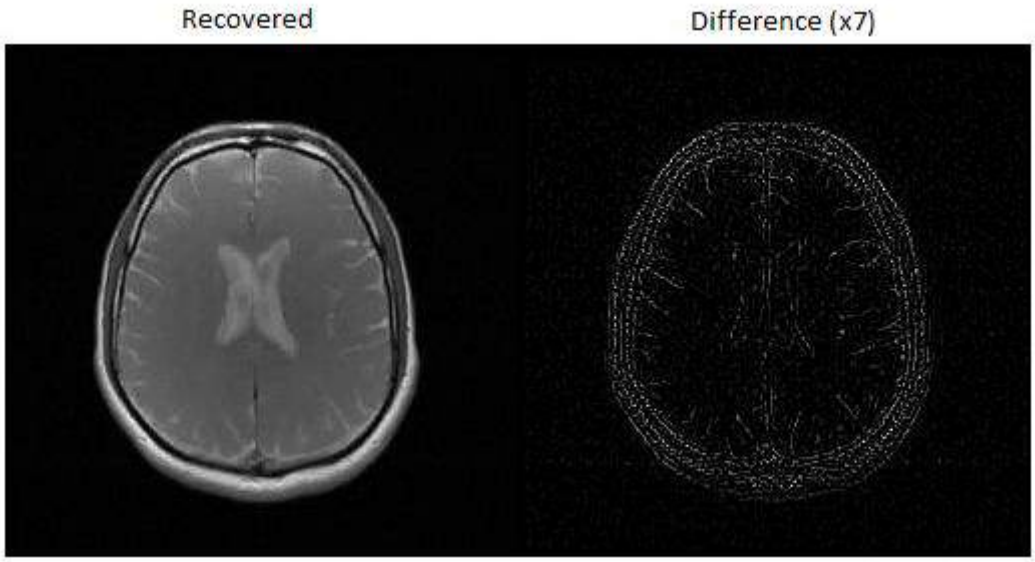

(b)

Fig. 5-5 Comparison of brain MR images in term of amplified difference between original and recovered images. a) Recovered image and magnified difference for the proposed method. b) Recovered image and magnified difference for the algorithm with fixed value threshold.

used for both algorithms to have better performance comparison. The improved PSNR for proposed algorithm in comparison with algorithm proposed in [93] is shown in

Fig. 5-6(a). Improvement in SSIM and correlation can be seen in

Fig. 5-6 (b) and (c) for the proposed algorithm with the adaptive threshold outperforms the algorithm with fixed threshold value used in [93].

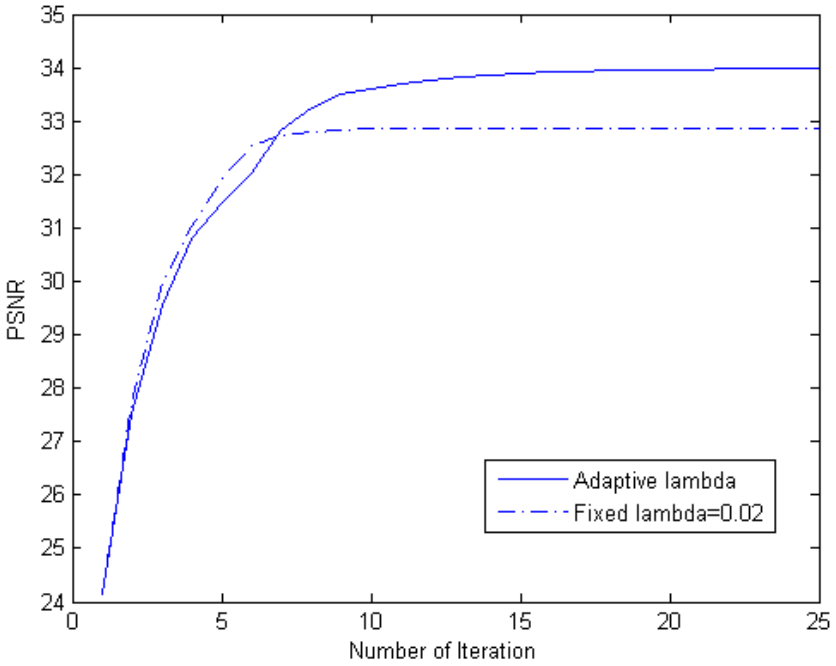

(a)

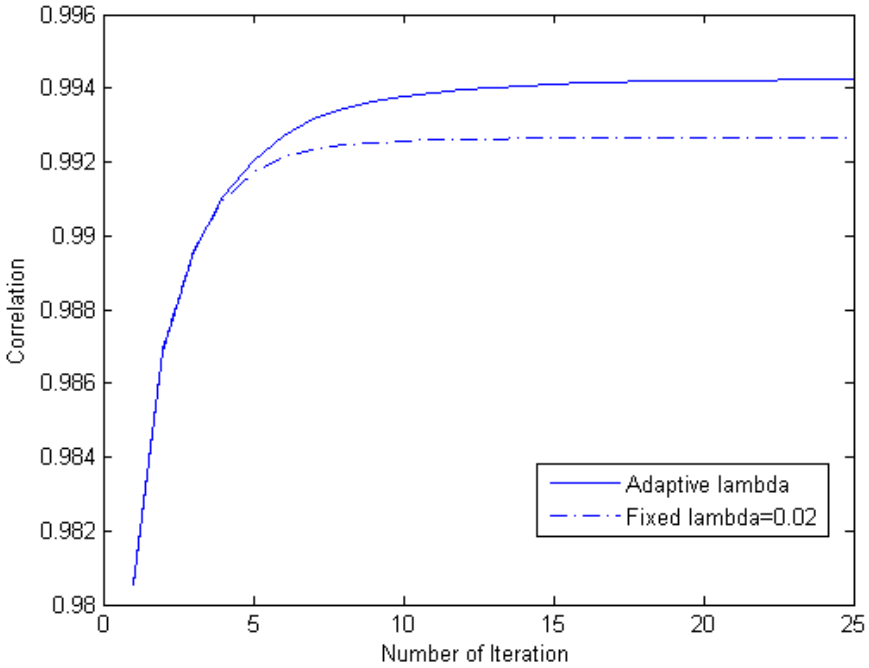

(b)

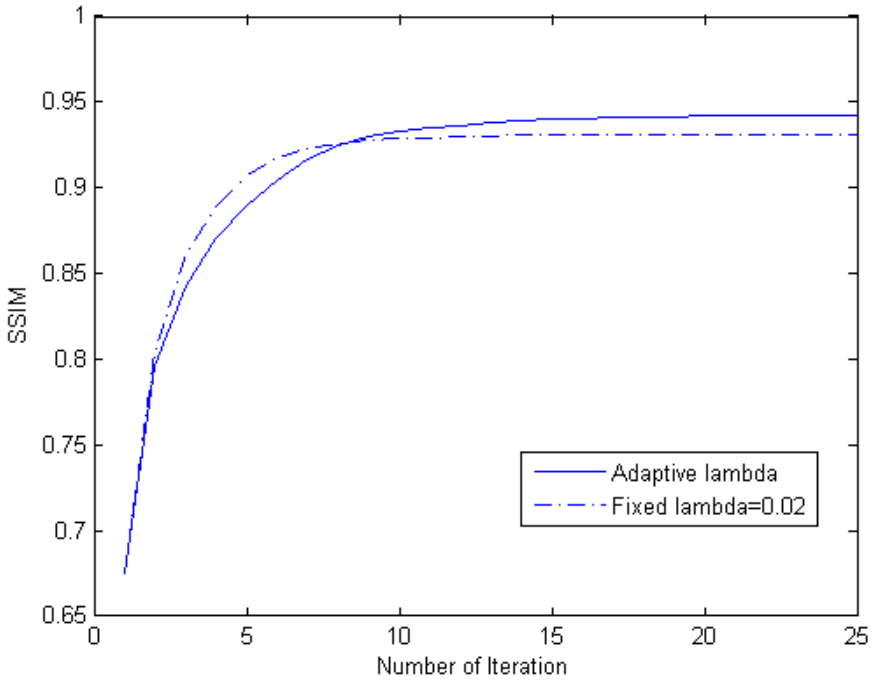

(c)

Fig. 5-6 Performance comparison between proposed method and an algorithm with fixed threshold. a) PSNR based comparison b) Correlation based comparison c) SSIM based comparison.

Decrease in λ value with the number of iteration is shown in Fig. 5-7. It can be seen from the figure that with the convergence of algorithm i.e. Improvement in MR image quality, the proposed algorithm suggests smaller values of λ which is intuitive.

In the second experiment we demonstrate the recovery of dynamic cardiac MR images using the proposed algorithm with λ_{adap} in shrinkage step. The Same cardiac cine data for volunteers taken from 1.5Tesla Philips scanneris used for testing as in [109].

The remaining parameters and sub-sampling mask required for algorithm are same as used for MR brain image. Variation in standard deviation of heart phases in a single cycle is shown in Fig. 5-8. This variation suggests the use of an adaptive threshold parameter during

the recovery process. Fig. 5-9 presents a reconstruction performance of proposed algorithm for three different heart phases at an acceleration rate of 8.

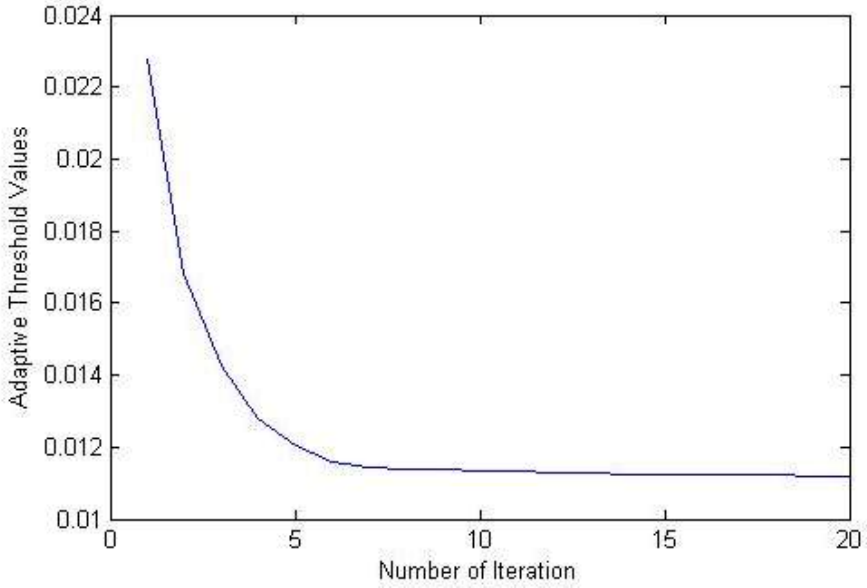

Fig. 5-7 Reduction in proposed threshold parameter values versus the number of iteration

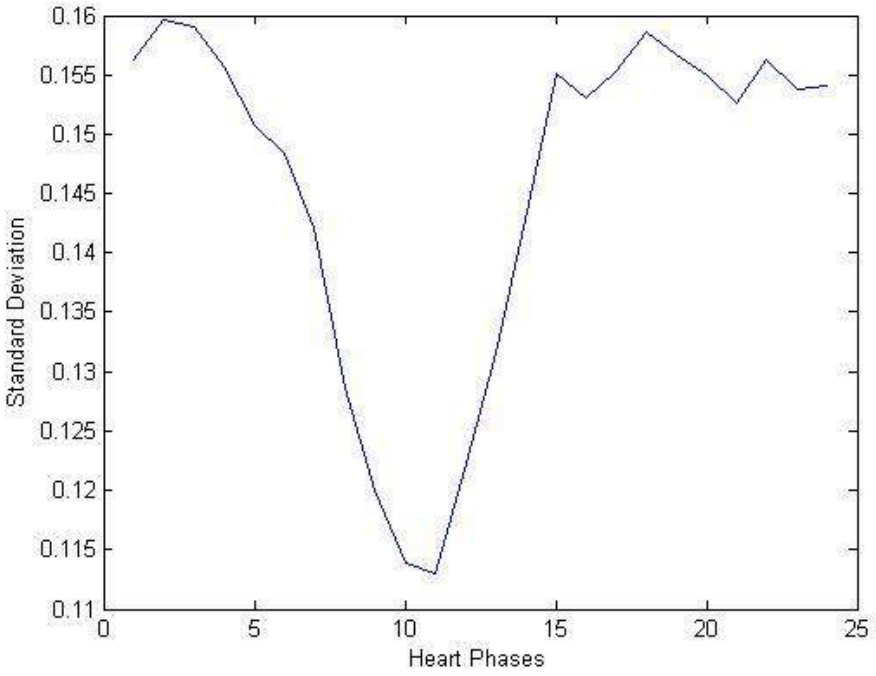

Fig. 5-8 Variations in standard deviation of heart phases

To visualize the details of the improved recovered images of proposed algorithm over fixed threshold value, the magnified difference (x12) is shown for each cardiac phase. From Fig. 5-9(b), (c) and (d), the adaptive threshold based algorithm has superior quality of recovery than fixed threshold based algorithm. The advantage of adaptive threshold value for 25 heart phases can be seen in Fig. 5-10 which provides comparison of PSNR and correlations for proposed algorithm. For all 25heart phases, the PSNR and correlations of recovered heart phases is higher for adaptive threshold algorithm. The improvement value is due to the adaptive capability of threshold parameter for the changing dynamics of heart. Correlation is taken between recovered images and ground truth for both adaptive and fixes threshold parameters.

Finally, the proposed algorithm is tested for the recovery of cardiac phases at different acceleration rates. Fig. 5-11 shows that the algorithm based on adaptive thresholding value outperforms as compared to the fixed values of threshold, taken as $\lambda = 0.02$ for brain image, at all acceleration rates.

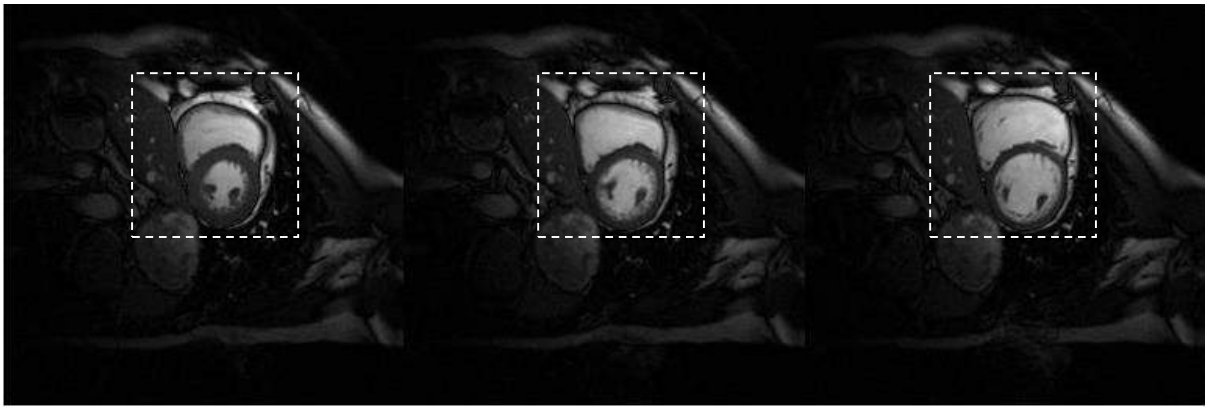

(a)

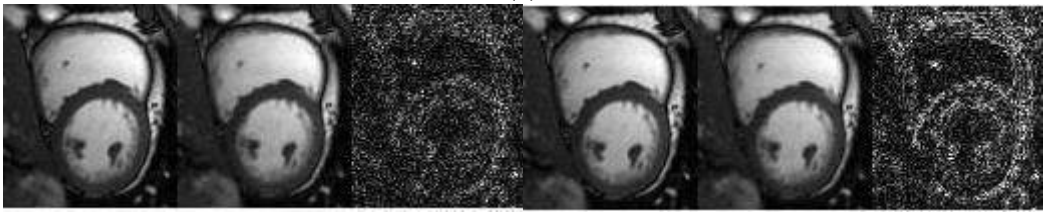

(b)

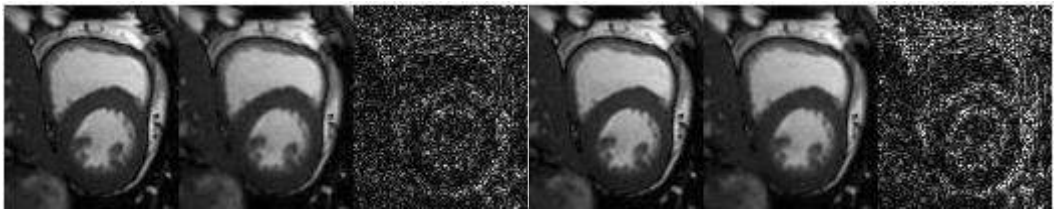

(c)

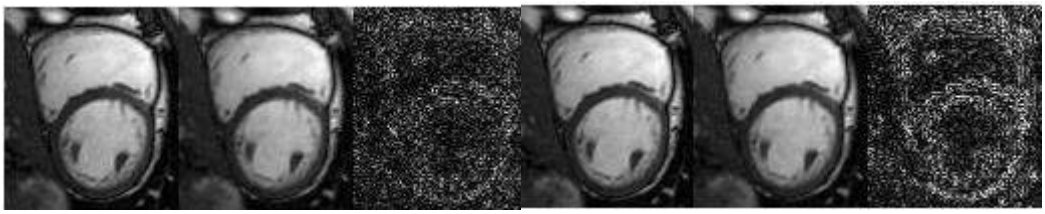

(d)

For the adaptive threshold value For fix threshold value

Fig. 5-9A comparison of the proposed and fixed value threshold based algorithms for the recovery of short axis cardiac MRI scan at the acceleration rate R=8.(a) Systolic, the middle of systolic and diastolic and diastolic phases (left to right). Ground truth images from full k-space data. White boxes show region of interest (ROI) (b)(c)and(d) enlarged ROI. Left column: Reconstructed heart phases with difference images magnified by 12 for proposed algorithm. Right column: Reconstructed heart phases with difference images magnified by 12 for the algorithm with fixed threshold value

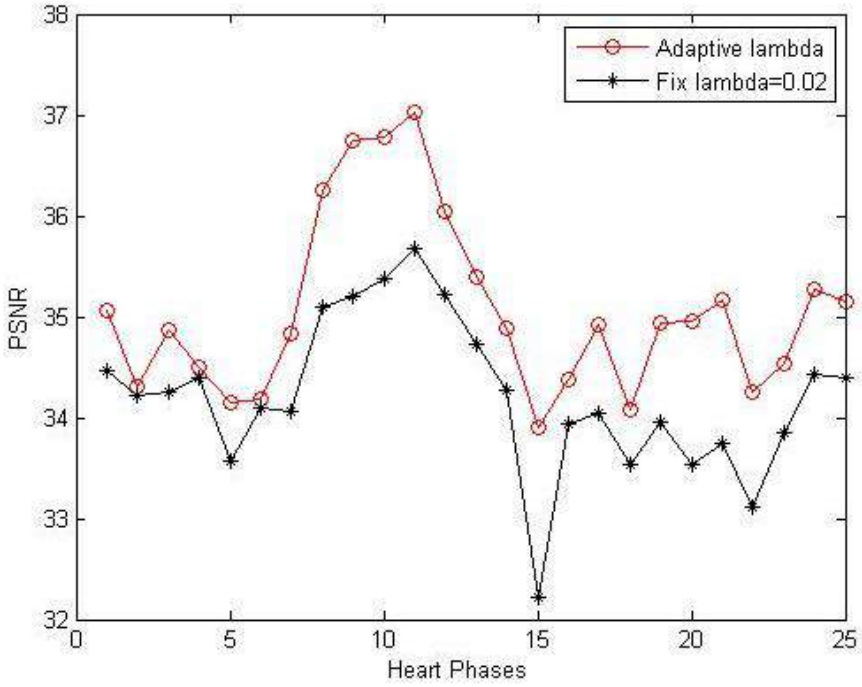

(a)

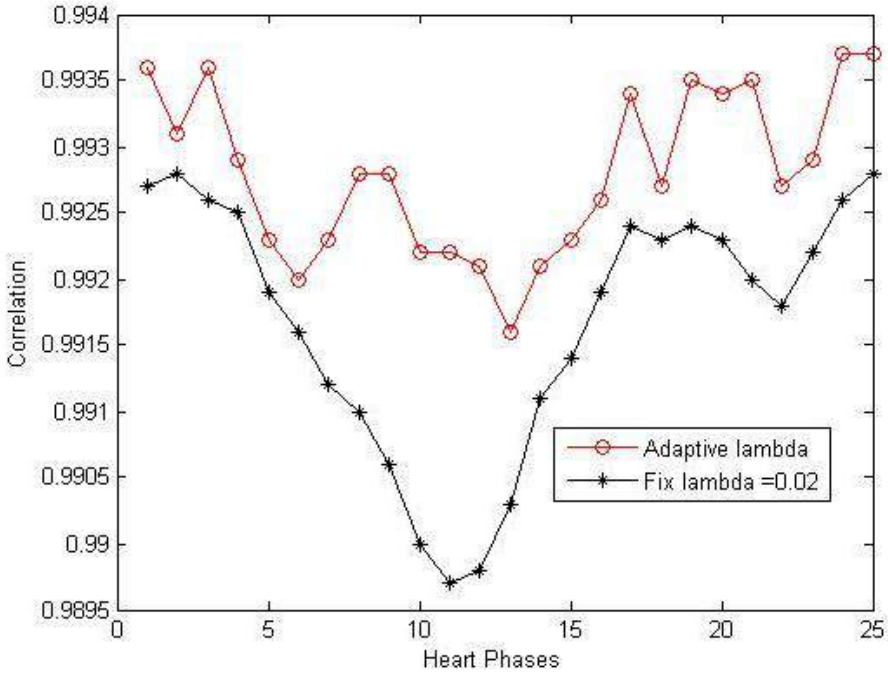

(b)

Fig. 5-10 Performance comparison between the proposed algorithm with adaptive threshold value and an algorithm with fixed threshold for cardiac phases a) PSNR based comparison b= Correlation comparison

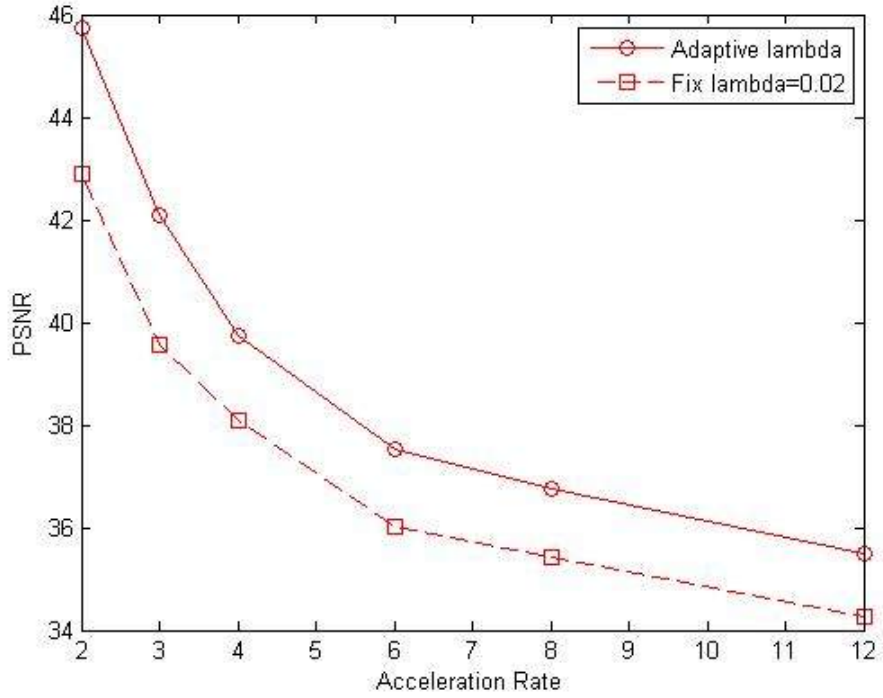

Fig. 5-11 PSNR at different acceleration rates for proposed and fixed value threshold algorithm

5.5 Summary

In this chapter, concept of image de noising in wavelet domain is extended to compress sensing. MAP estimation approach for de noising is used to derive an adaptive threshold parameter. The fixed threshold value, normally used in de noising as well as in IST for CS recovery, is made data driven and adaptively updated during recovery process. A soft threshold function based algorithm using adaptive threshold is proposed and tested for static and dynamic MR images. The adaptive threshold parameter adjusts its value according to the under-sampling artifacts and the changing dynamics of MR images. Simulation results validate that proposed algorithm with adaptive threshold perform better than fixed value threshold for different acceleration rates, and recovers the images with higher PSNR and correlation.

Chapter 6

Data Binning and RPCA Based Motion Artifacts Reduction in Compressively Sampled DCE MR Images

Respiratory motion produces ghosting and blurring artifacts in reconstructed MR images. Motion during scan process is more challenging in DCE MRI because motion effects and rapid intensity changes in contrast agent is difficult to distinguish from each other. In this chapter a new technique, based on data binning and robust principle component analysis (RPCA) or L+S matrix decomposition, is introduced to reduce the motion artifacts for DCE MRI. Under-sampled free breathing 3D liver and abdominal DEC MR data sets are used to validate the proposed technique. The performance of the technique is compared with standard RPCA method. The results show improved MR images with data binning as pre-processing step in free breathing scenario.

6.1 Automatic motion detection and data binning:

The basic strategy is to acquire DCE-MR images with respiratory motion and then reconstructs the images free from motion effects. To recover motion free images, acquired *k*-space samples must be grouped in such a way that each group (motion state) has very less respiratory motion. For grouping or binning of the data, two principle requirements are: a) reliable respiratory motion signal b) uniform coverage of *k*-space after data binning. Consecutive spokes of the golden angle radial sampling with an angle of approximately 111.25^{o},are used for data acquisition [110] . This sampling scheme samples the *k*-space

centre repeatedly that enables the extraction of respiratory motion state signals [111, 112] for data binning. It also provides consistent *k*-space coverage in all respiratory states with adequate randomness in sampling pattern for the application of compressed sensing. The 3D DCE-MRI *k*-space data can be represented in matrix form as follows:

$$\boldsymbol{y}_u = \boldsymbol{F}_{nu}\boldsymbol{C}\boldsymbol{x} \tag{6.1}$$

Where $\boldsymbol{x}$ is the 3D DCE image series to be recovered with $(x - y - z - N_c)$ dimensions,$\boldsymbol{F}_{nu}$ is the nonlinear fast Fourier transform operator (NUFFT), $\boldsymbol{C} = \begin{bmatrix} \boldsymbol{C_1} \\ \vdots \\ \boldsymbol{C}_{Nc} \end{bmatrix}$ represents the coil sensitivity maps for N_c number of coilsin $x - y$ space and $\boldsymbol{y}_u$ is the unsorted multicoil radially sampled *k*-space data with $(N_r - N_s - z - N_c)$ dimensions. z represents the linear slice dimension, N_r is the number samples along a spoke and N_s is the number of spokes.

A robust approach, for the detection of motion from *k*-space data, is to use projections along the slice dimension for 3D stack of star imaging [113]. In this approach, spokes for all slices along z direction are acquired and then 1D Fourier transform is computed to obtain the projection profiles for central points$(x, y = 0)$ and for all acquisition angles. Once the projection profile obtained for all coils, they are linked to form the following $(N_c \times N_r) - by - N_s$matrix:

$$A = \begin{bmatrix} U_1 \\ \vdots \\ U_{N_c} \end{bmatrix}, with\ U_\alpha = \begin{bmatrix} u_\alpha(a_1, b_1) & \dots & u_\alpha(a_1, b_{N_s}) \\ \vdots & \ddots & \vdots \\ u_\alpha(a_{N_r}, b_1) & \dots & u_\alpha(a_{N_r}, b_{N_s}) \end{bmatrix} for\ \alpha = 1,2 \dots N_c \tag{6.2}$$

As discussed in[112], PCA is used to estimate the motion signal from concatenated data matrix A of all coils. PCA is accomplished by computing the right singular vectors of A, or equivalently the eigen-vectors of the covariance matrix $Cov = A^T A$. Principle

component with highest peak in the range of respiratory signal frequency 0.1Hz to 0.5Hz is selected to represents breathing signal. Based on the estimated respiratory signal, the radially acquired data is first divided into consecutive contrast enhancement phases and every phase was then further divided into multiple motion states having the same number of spokes. This binning process provides the data $\boldsymbol{d}$ with dimension($N_r - N_s - N_{cont} - N_R$). Where N_{cont} shows the number of contrast phases and $N_R$represents number of respiratory states. The idea is shown in Fig. 6-1.

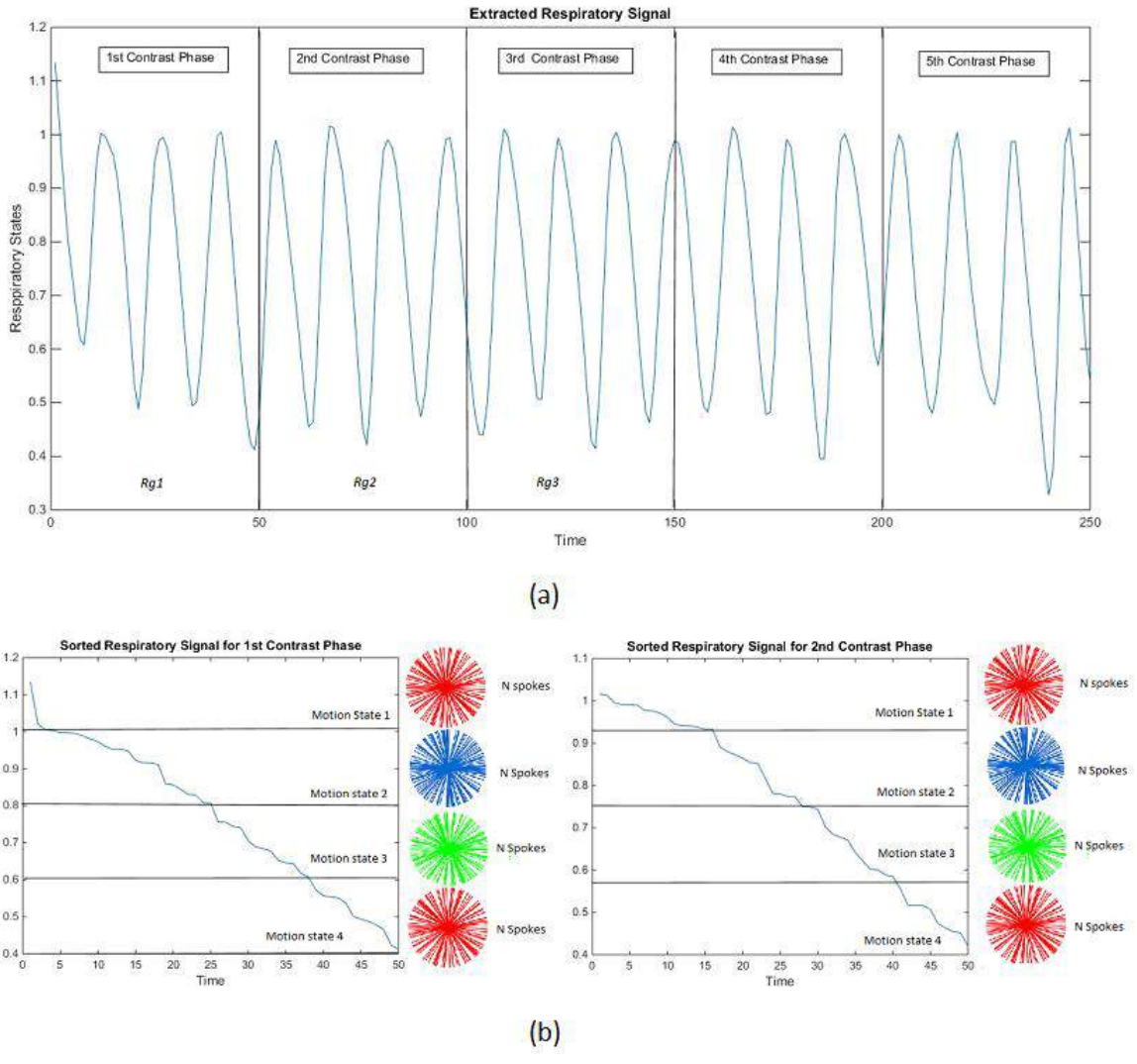

Fig. 6-1 For liver DCE-MRI, extraction and binning of respiratory signal **a)** Extracted

respiratory signal from k-space data. The signal is divided among different contrast phases. b) Binning procedure for the sorted respiratory motion signal carried out in every contrast enhancement phase separately. Distinct radially sampled patterns (shown in different colors) are used for different respiratory states and same number of spokes is used for each respiratory state.

Binning of radially sampled k-space date in different respiratory states clearly reduce the motion effects (can be observed by solid line in Fig. 6-2) but on the other hand introduces streaking artifacts (shown by white arrows). L+S decomposition in conjunction with compressed sensing is used to remove these under-sampling artifacts.

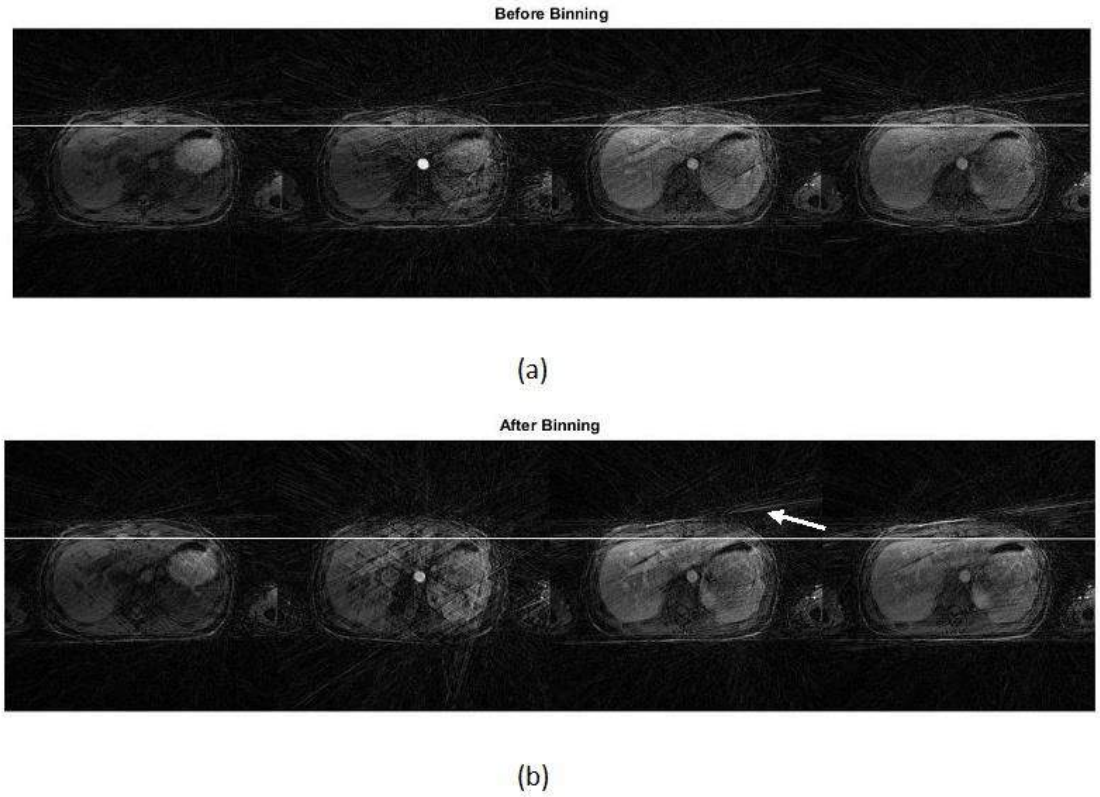

Fig. 6-2 Contrast enhancement phases before and after binning. a) Motion is present along with streaking artifacts. The solid line clearly shows the misalignment of different contrast phases. b) Respiratory motion is resolved after binning and phases are aligned

with each other. It can be observed along the solid line. White arrows show streaking artifacts.

6.2 L+S matrix decomposition:

The L+S matrix decomposition of DCE MR images decomposes it into a low rank component, containing smooth and slow variations and a sparse component comprising fast and local intensity changes. A necessary condition for this decomposition is incoherence between L and S components. It means that L component should not be sparse and sparse component should not have low rank [38, 39].

For the implementation of L+S decomposition method, the sequence of DCE MR Images is placed in a matrix form such that each column represents one temporal frame. This matrix is called Casorati matrix. The L+S decomposition is performed by solving the following convex optimization problem:

$$min\|\boldsymbol{L}\|_* + \lambda\|\boldsymbol{S}\|_1 \qquad s.t. \;\; \mathbb{M} = \boldsymbol{L} + \boldsymbol{S} \tag{6.3}$$

where $\boldsymbol{S}$ represents sparse matrix, $\boldsymbol{L}$ is the low rank matrix and $\mathbb{M}$ is the Casorati matrix.$\|L\|_*$is the nuclear norm (the sum of singular values of $\boldsymbol{L}$), $\|\boldsymbol{S}\|_1$ is the l_1-norm (the sum of absolute values of components of $\boldsymbol{S}$), and λ is a balancing parameter that defines the share of the l_1-norm relative to the nuclear norm.

Fig. 6-3 shows the L+S decomposition of DCE MRI data set after binning, where $\boldsymbol{L}$ captures the smooth and slow varying correlated background between frames and $\boldsymbol{S}$ captures the contrast-enhancement changes. Two features can be observed in Fig. 6-3(b) and (c). The first one is, the $\boldsymbol{S}$ component is sparser than $\mathbb{M}$ component for both data sets. The separation of smooth changes from contrast enhancements provides gain in sparsity

and in principle permit higher acceleration rates [90]. The second one is, the $\boldsymbol{S}$ component of the proposed method (Fig. 6-3b) is sparser than the S component for the data set without binning (Fig. 6-3 c). This increased sparsity is achieved by resolving the motion through the binning process. As a result, higher acceleration factors can be achieved with the proposed method.

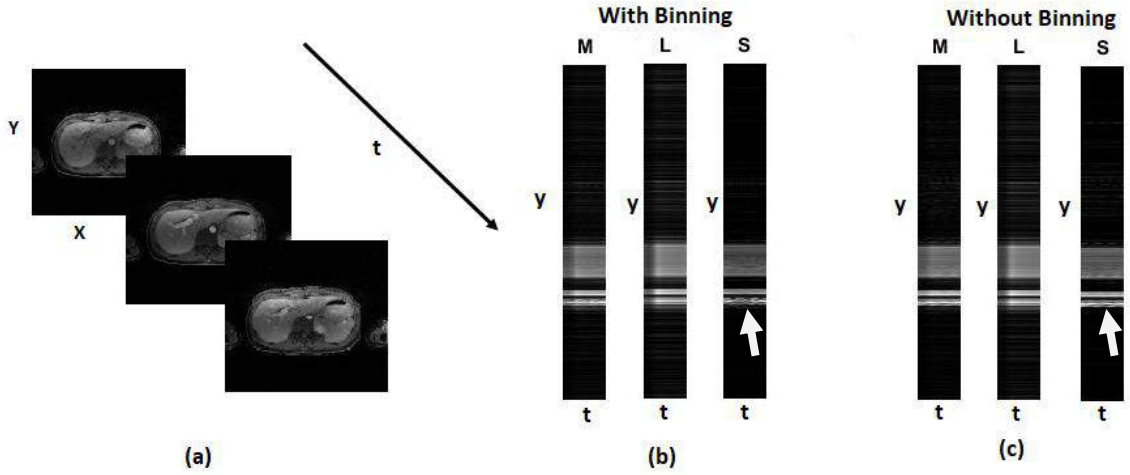

Fig. 6-3 L+S decomposition for DCE MRI with and without binning **a)** series of images along time. Decomposed components in y-t space b) for proposed method c) without binning. The $\boldsymbol{S}$ component is sparser in b) as compared to the $\boldsymbol{S}$ component in c).

6.3 Under sampled MR images reconstruction

The modified version of (6.3) for radially under-sampled liver DCE MR data set $\boldsymbol{d}$ can be written as

$$min\|\boldsymbol{L}\|_* + \lambda\|\boldsymbol{\Psi S}\|_1 \qquad s.t. \;\; \boldsymbol{d} = \boldsymbol{E}(\boldsymbol{L}+\boldsymbol{S}) \tag{6.4}$$

and the unconstrained version of equation (6.4) can be given as

$$min\frac{1}{2}\|\boldsymbol{E}(\boldsymbol{L}+\boldsymbol{S}) - \boldsymbol{d}\|_2^2 + \lambda_L\|\boldsymbol{L}\|_* + \lambda_S\|\boldsymbol{\psi S}\|_1 \tag{6.5}$$

Where $\boldsymbol{\psi}$ is sparsity inducing transform applied to $\boldsymbol{S}$, $\boldsymbol{d}$ is the radially under-sampled data obtained after binning process as discussed above. $\boldsymbol{E}$ is the multiple receiver coil encoding operator, which includes coil sensitivities $\boldsymbol{C}$ and under-sampled non-uniform Fourier

transformation $\boldsymbol{F}_{nu}$(NUFFT) [114]. These factors are multiplied to get $\boldsymbol{E}$, as described in SENSE algorithm[21]. The multi-coil reconstruction approach gives better performance due to the enforcement of joint multi-coil low rank and sparsity [83]. λ_L and λ_S is trade-off parameter and provides a balance between data consistency term and the other two terms (nuclear and l_1 norm terms). The optimization problem in (6.5) is solved by combining singular value threshold, a method used for matrix completion [115], and iterative soft threshold used for sparse signal recovery [116]. The shrinkage or soft threshold is defined as

$$T_{\lambda_S}(v) = \frac{v}{|v|}\max(|v| - \lambda_S, 0) \tag{6.6}$$

For matrices, the soft threshold is applied to every entry. Next, we define the singular value threshold (SVT) by,

$$SVT_{\lambda_L}(M) = U\mathrm{T}_{\beta}(\Sigma)V^H \tag{6.7}$$

where $U\Sigma V^H$ is singular value decomposition of Casorati matrix $\mathbb{M}$. Fig. 6-4 shows the proposed HL+S algorithm for the recovery of DCE MR Images.

Inputs:

$\boldsymbol{y}_u$: Multi coil radially sampled k-space data

$\boldsymbol{E}$: Multicoil encoding operator

$\boldsymbol{\psi}$: Sparsifying transform

λ_L: Singular-value thresholding parameter

λ_s: sparsity thresholding parameter

Phase 1: Respiratory signal extraction

Step 1: Find projection profiles using 1D Fourier transform along z-axis (slice dimension).

Step 2: Perform PCA for the matrix given in (6.2).

Step 3: Select the principle component to represent breathing signal R_g with highest peak in the range respiratory signal frequency

Phase 2: Data Binning

Step 4: Division of respiratory signal R_g among contrast phases to generate sub respiratory signals R_{g1}, R_{g2}, ... etc. as shown in Fig 6.1 (a)

Step 5: Sort R_{g1}, R_{g2}, ... for smooth transitions

Step 6: Divide sorted R_g in different respiratory states and assign equal number of spokes to each state as shown in Fig. 6-1(b) to generate data $\mathcal{d}$.

Phase 3: Recovery of motion free DCE MR images

Initialization $\mathbb{M}_o = \boldsymbol{E}^*\boldsymbol{\mathcal{d}}, \boldsymbol{S}_o = 0$

Iteration (Repeat until not converged)

Increment i by 1

Step 7: Singular value soft threshold

Compute $L_i = SVT_\lambda(\mathbb{M}_{i-1} - S_{i-1})$ using (6.7)

Step 8: Shrinkage in sparsifying domain

Compute $S_i = \Psi^{-1}(\Lambda_s(\Psi(\mathbb{M}_{i-1} - L_{i-1})))$ using T_{λ_S} given in (6.6)

Step 9: Data consistency

$$\mathbb{M}_i = L_i + S_i - E^*(E(L_i + S_i) - \mathcal{d})$$

Output

$\boldsymbol{L}, \boldsymbol{S}$ *and* $\mathbb{M} = \boldsymbol{L} + \boldsymbol{S}$

Fig. 6-4 Proposed hybrid L+S (HLS) reconstruction algorithm for DCE MRI

6.4 Methods

The performance of the proposed methodology was tested for under-sampled 3D liver and abdominal DCE-MRI with respiratory motion for a number of subjects. The Human imaging was performed after the approval from the institutional review board (IRB). Written informed consent was obtained from all subjects before imaging studies. Golden-angle radial sampling, given in Fig. 6-5 with 111.25^{o} angular increment between consecutive spokes [110], was used for data acquisition. MATLAB (Mathswork, Natik, MA) was used for image reconstruction. The multi coil encoding operator $\boldsymbol{E}$ was implemented using NUFFT [114]because of radial sampling. Adaptive coil combination method discussed in [23] was used to generate coil sensitivity maps.

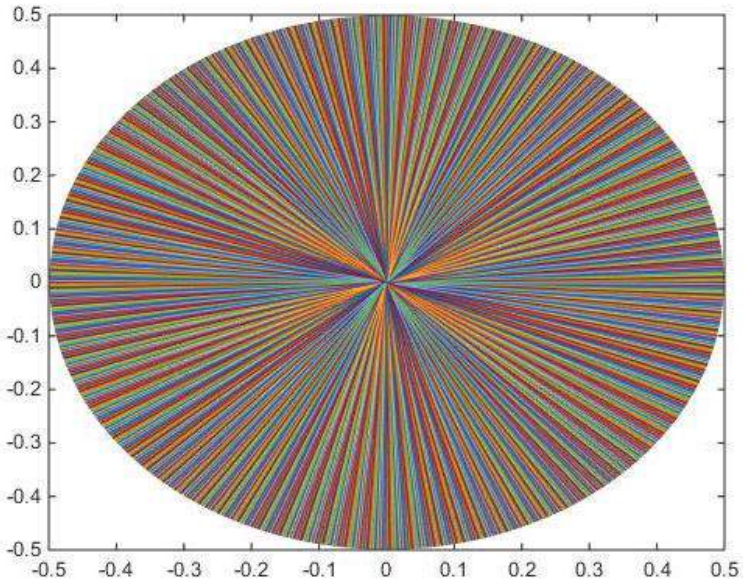

Fig. 6-5 Radial sampling mask

The balancing parameters λ_s and λ_L were chosen empirically by comparing reconstructed images for different values. Results for both data sets were generated using the modified version of nonlinear conjugate algorithm [4]. The performance of the proposed method was assessed qualitatively as well as by sharpness index (SI) and SSIM given in chapter 2.

6.4.1 Free breathing 3D abdominal DCE-MRI

3D abdominal imaging was carried out on an entire-body of a volunteer using 3.0T scanner (Siemens AG, Erlangen, Germany), having standard 12-element body matrix coil. The 3D stack-of-stars (radial sampling for $x, y = 0$ and Cartesian sampling for z) pulse sequence with golden-angle acquisition method was used to acquire data in transversal orientation. Intravenous injection of $10mL$ of gadopentetate dimeglumine (Gd-DTPA) (Magnevist; Bayer Healthcare, Leverkusen) was started at a time with the beginning of data acquisition. The process was completed by injecting $20mL$ saline for flushing purpose. Injection rate was $2mL/s$ for both contrast agent and saline. For a single scan, the imaging parameters for the volunteer were: repletion time TR/echo time TE= 3.52/1.41 ms, FOV = 360x360x240 mm^3, number of readout points in each spoke = 256, spatial resolution = 1.4x1.4x3 mm^3, number of partitions = 80, with 60% slice resolution reduction and 6/8 partial Fourier applied to the slice dimension. A total of 600 spokes were continuously acquired in each partition, for a total scan time of 95 s

6.4.2 Free breathing 3D liver DCE MRI

3D liver DCE-MRI was performed at four volunteers on an entire-body 3.0T scanner (Siemens AG, Erlangen, Germany) fitted with the standard 12-element body matrix coil. The 3D stack-of-stars (radial sampling for $x, y = 0$ and Cartesian sampling for z) pulse sequence with golden-angle acquisition method was used to acquire data in transversal

orientation. For each scan, a weight-based half-dose injection (0.1 mmol per kilogram of body weight) of Magnevist (Bayer Healthcare, Berlin, Germany) was performed 20s after the start of data acquisition, at a rate of 2*mL/s*. The imaging parameters were: repetition time (TR)/echo time (TE) = 3.6/1.6 ms, matrix size = 256x256x48, FOV= 350x350x240 mm^3, acquired voxel size=1.37x1.37x5.0 mm^3, flip angle=12^o. Eighty percent partial Fourier was applied to the slice dimension and a total of 1222 spokes were obtained for every partition, resulting in a total scan time of 190 s

6.5 Results

6.5.1 Free breathing 3D abdominal DCE-MRI

Fig 6-6 provides a comparison between HL+S method and CL+S. (a) is the reference image representing four contrast phases for a volunteer data set. This single slice data corresponds to early contrast phase, aorta, portal vein and liver. Structural similarity is measured with respect to this reference image.

Proposed technique presents improved reconstruction performance in all four phases as compared to L+S without binning, as pointed out by a better presentation of small structures that appear blurry in b)(white arrows). Vessels and tissue contrast improvement can also be observed in (c).

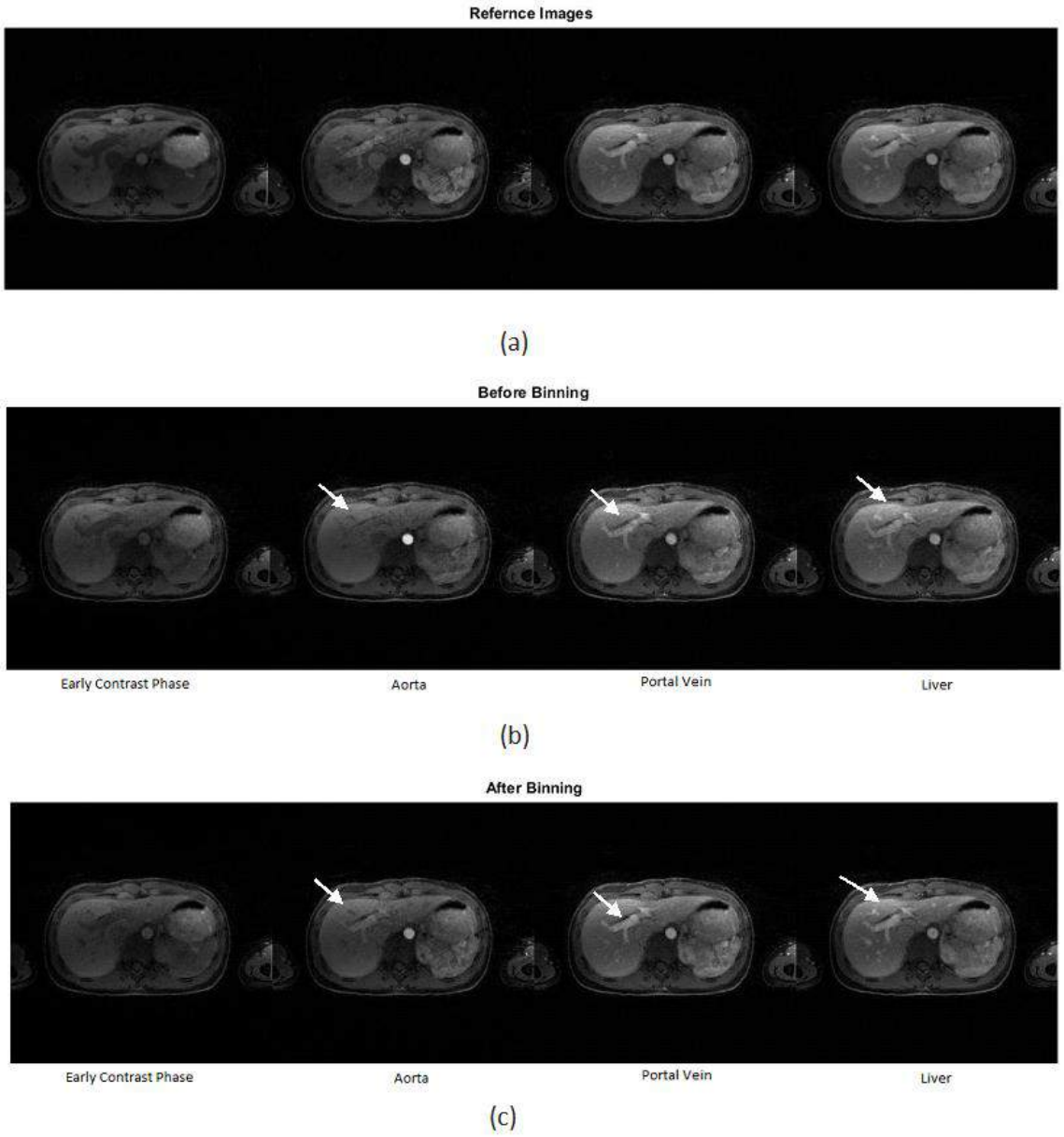

Fig. 6-6 Qualitative comparison: reference images a) HL+S images b) and CL+S images c) for abdominal DCE MRI. Improved vessels illustration and removal of blurring effects from contrast phases can be observed in c).

Fig. 6-7 presents the similarity of images, recovered before and after binning, with respect to the reference image given in Fig. 6.6 (a). Higher similarity index can be observed for the proposed method. This higher value of SSIM is achieved due to the pre-processing step of binning which reduces the motion effects in recovered images.

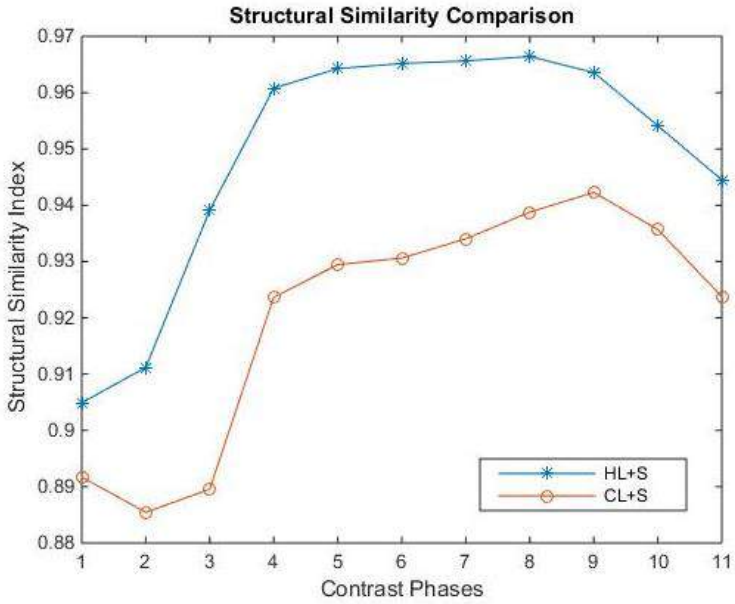

Fig. 6-7 Structural similarity based performance comparison for different contrast phases.

The sharpness comparison between conventional L+S method and proposed technique is given in Fig. 6-8. It is clear from the plot that proposed technique (HL+S) outperform the CL+S decomposition method.

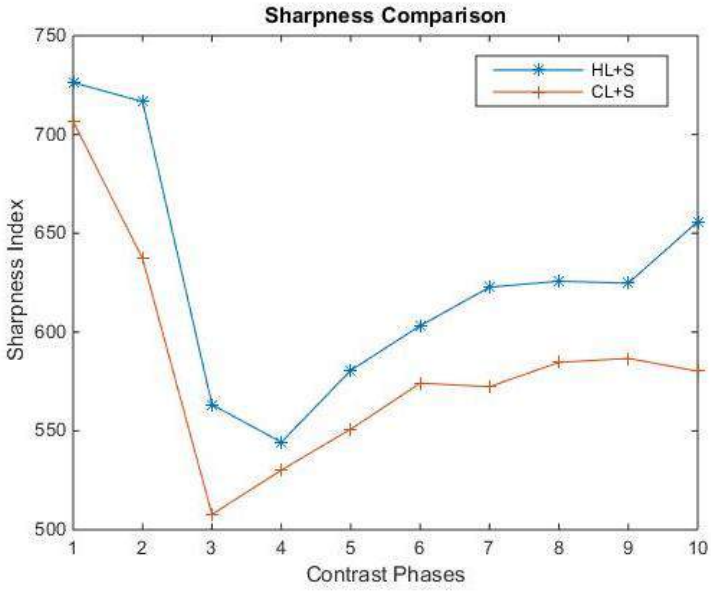

Fig. 6-8 Sharpness comparison of contrast phases recovered with and without binning. Higher sharpness index can be observed for the proposed method.

6.5.2 Free breathing liver DCE MRI:

Fig. 6-9 shows different contrast enhancement phases recovered by the proposed method and conventional L+S decomposition method along with reference images in a).

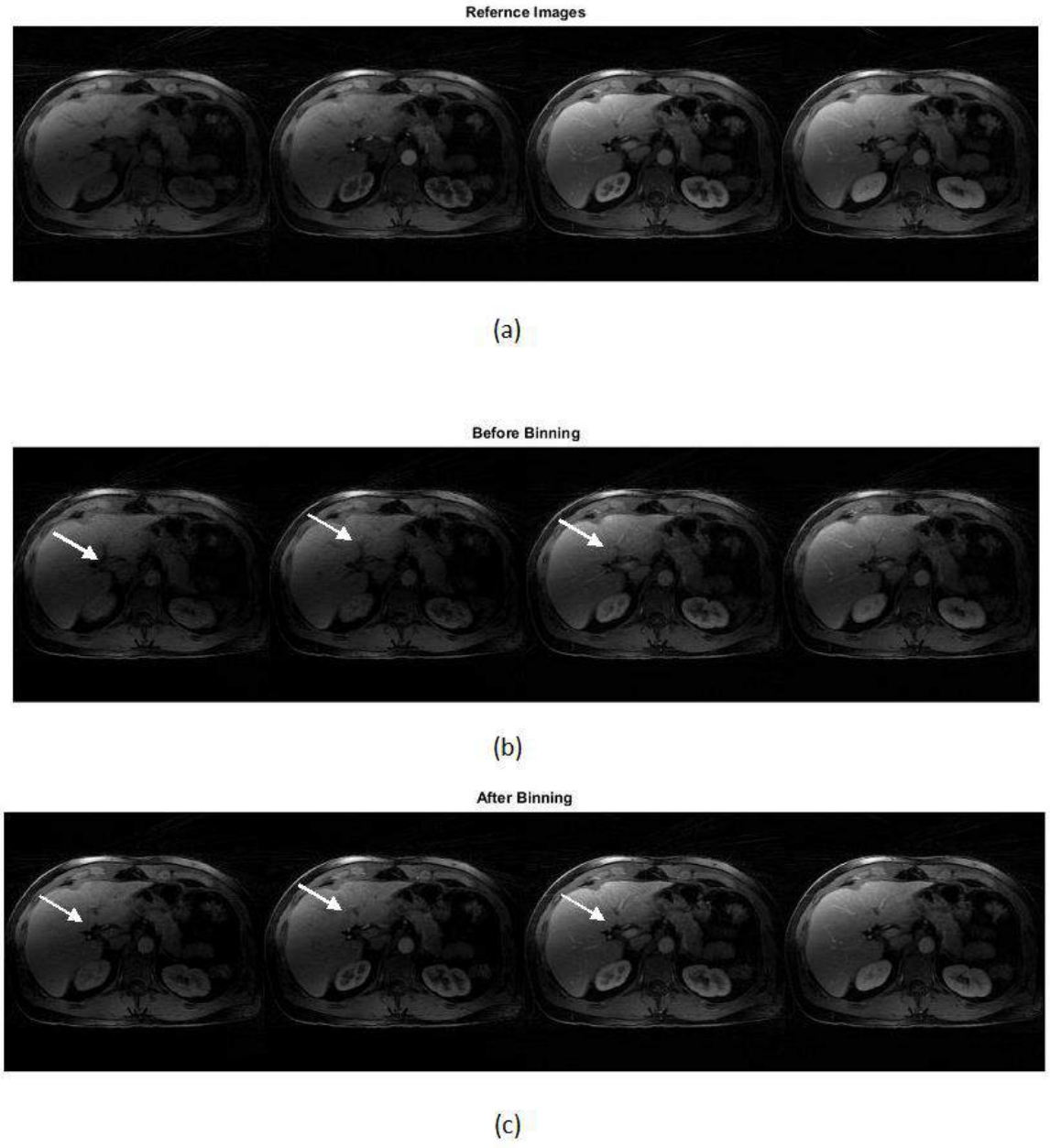

Fig. 6-9 Qualitative comparison: reference images a) HL+S images b) and CL+S images c) for liver DCE MRI. Without binning recovery suffered from respiratory motion blurring effects. In contrast, the proposed method enabled improved reconstruction of all phases, better capture of the arterial phases, higher vessel clarity and sharpness.

The pre-processing step improved the illustration of vessels and vessel-tissue contrast in the recovered images with the HL+S method as compared to the CL+S method. Comparison points are shown by White arrows in b) and c).

Fig. 6-10 provides structural similarity index comparison and Fig. 6-11 presents a sharpness comparison between HL+S and CL+S method. For parameters, sharpness and SSIM, the proposed HL+S method performs better as compared to CL+S method.

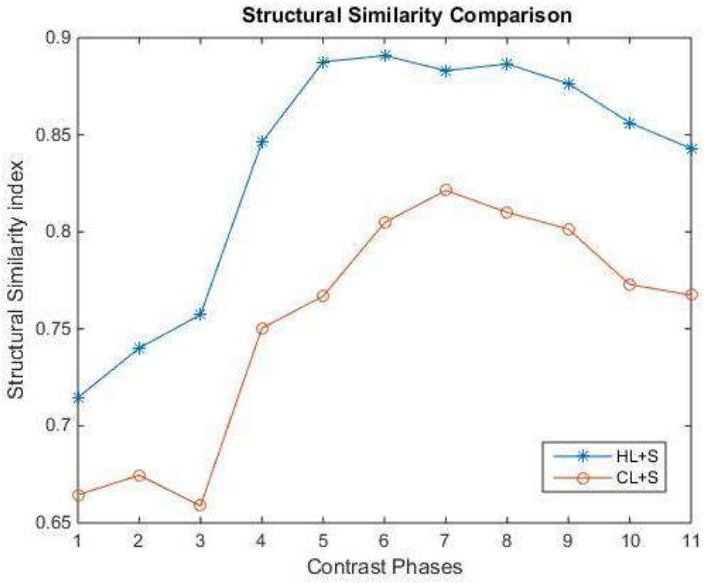

Fig. 6-10 Structural similarity based performance comparison for different contrast phases.

6.6 Discussion

Data binning provides a new method to deal respiratory motion in free-breathing DCE MRI. By sorting the data in similar motion state reduces most of the free breathing artifacts in recovered images. No interpolation errors are occurred in the proposed technique and provide a great advantage over the CS-based registration techniques [84, 117], which uses an image registration process in multiple respiratory states to correct motion.

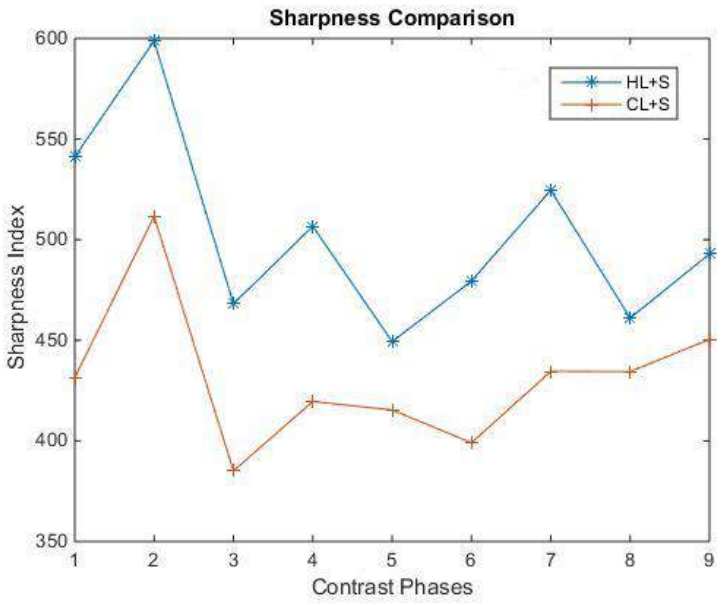

Fig. 6-11 Sharpness comparison of contrast phases recovered with and without binning. Higher sharpness index can be observed for the proposed method.

The number of motion states, to resolve the respiratory motion, is selected empirically. A trade-off must be adopted between visualization of breathing motion through binning and under-sampling artifacts. By increasing motion states, the number of radial spokes for each state will be reduced and hence increasing the under-sampling artifacts. On the other hand, we choose less number of motion states, the under-sampling artifacts will be reduced because more spokes are available for each state. But the motion is not resolved effectively in this case. Fig. 6-12 shows the effects of number of motion states on images recovered through conventional NUFFT without CS-based L+S decomposition method. Figure shows that respiratory motion is resolved better for 4 and 6 motion states as compared to 2 motion states, but the under-sampling artifacts for 2 motion states are very less in comparison with the other two states

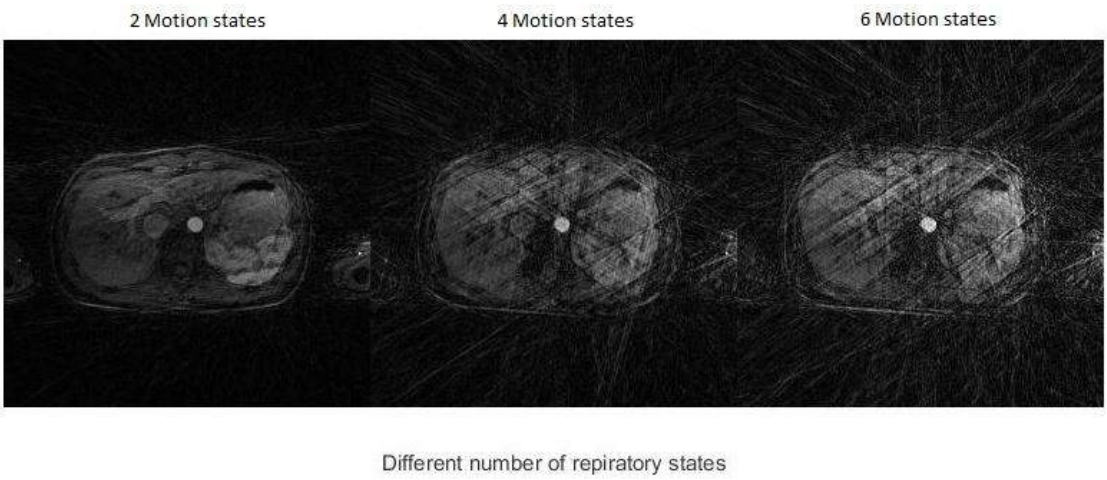

Fig. 6-12 Comparison of a few different respiratory states. 2 motion states have less streaking artifacts as compared to 4 and 6 respiratory motion states.

The golden angle radial under-sampling scheme for data binning increases the computational cost mainly due to the computation of NUFFT in forward and backward direction during each iteration. This problem can be resolved by parallel computational techniques. The reconstruction algorithm uses balancing parameter, λ_L and λ_S, and are selected empirically from a range of values that gives the best image quality. The selection process for these parameters is lengthy for dynamic imaging method, but once found, similar parameter values can be used for data sets having same dynamic information. Automatic selection of regularization parameter as discussed in[118] is also applicable to L+S decomposition method. λ_L and λ_S parameters balance the contribution of the L and S components. Since we are interested in overall reconstruction not in $\boldsymbol{L}$ or $\boldsymbol{S}$ separately, the technique is less sensitive to the selection of balancing parameters.

6.7 Summary:

In this chapter, data binning as a pre-processing step to reduce motion effects with conventional L+S decomposition is presented. The pre-processing provides $\boldsymbol{S}$ component

with greater sparsity which results in higher reconstruction performance. The separation of background and dynamic information, provided by L+S decomposition, is improved by proposed method without the need for motion correction. The recovered images have better sharpness, clarity and similarity with reference images as compared to conventional L+S decomposition method.

Chapter 7

Conclusions and Future Work

7.1 Conclusions

In this dissertation, we have proposed different techniques to mitigate the motion artifacts in the reconstruction of compressively sampled MR images for cardiac cine and DCE MRI. The proposed methods are the combination of compressed sensing and motion artifacts reduction techniques. The algorithms used in CS are modified and updated in novel way. A comparison of surrogate functions used to approximate l_1-norm is performed. It is concluded that the hyperbolic tangent based approximation is better as compared to previously used surrogate function in literature. We work out a new method for respiratory motion correction in ECG gated free breathing cardiac MRI. Inter-frame motion estimation was used to estimate the respiratory motion between the same cardiac phases, but at different respiratory states. The block matching algorithm was used for MEMC. A gradient decent algorithm based on flexible l_1-norm approximation was used for the recovery of MR images free from motion artifacts and close to the true MR images. The images recovered with proposed method were improved as compared to the images recovered without MEMC and with kt-FOCUSS.

The concept of image denoising in wavelet domain, extended to compress sensing, is discussed next. MAP estimation approach for denoising is used to derive an adaptive threshold parameter. The fixed threshold value normally exploited in denoising as well as in IST for CS recovery, is made data driven and adaptively updated during recovery

process. A soft thresholding function based algorithm using adaptive threshold is proposed and tested for static and dynamic MR images. The adaptive threshold parameter adjusts its value according to the under-sampling artifacts and the changing dynamics of MR images. Technique for motion artifacts reduction in free breathing DCE MRI is presented in the last of thesis. In this technique, data binning is used as a pre-processing step to reduce motion effects with conventional L+S decomposition. For binning, respiratory motion signal is extracted directly from radially sampled data. The pre-processing provides $\boldsymbol{S}$ component with greater sparsity which results in higher reconstruction performance. The separation of background and dynamic information, provided by L+S decomposition, is improved by proposed method without the need for motion correction.

7.2 Future work

Future directions for the research work presented in this dissertation are as follows

1. More flexible and data dependent surrogate functions to approximate the l_1-norm can be investigated that are robust not only for respiratory motion but for other body motions also.
2. In chapter 4, the proposed method requires higher computations due to an iterative nature of the algorithm. To estimate motion corrected image, the algorithm needs to compute motion operators $\boldsymbol{M}$ and refined image $\boldsymbol{x}$ alternatively multiple times. The ARPS introduces interpolation error during the prediction process of motion corrected image. There is a need to investigate motion estimation schemes with reduced interpolation error during the process of motion estimation and correction. In the presented scheme, motion corrected images are produced from a fixed reference frame. In the Future, motion estimation can be done from adjacent

frames in both forward and backward direction and other CS recovery approaches can be used. Further research might be required to find its usage in 3D dynamic cardiac MRI. The proposed method will require modification for arrhythmic patients because heart rate variability is not considered in this work. Similar cardiac phases at different respiratory states are chosen visually from a sequence of cardiac MRI frames. Data binning might be used for selection of cardiac phases at different respiratory states.

3. In chapter 5, we use exact Laplacian distribution for the derivation of adaptive threshold parameter but The wavelet domain coefficients of images peaked at zero do not follow exact Laplacian distribution. Some function or distribution that exactly models the coefficients will give better threshold adaptive parameter.
4. In chapter 6, the golden angle radial under-sampling scheme for data binning increases the computational cost mainly due to the computation of NUFFT in forward and backward direction during each iteration. This problem can be resolved by parallel computational techniques. The reconstruction algorithm uses balancing parameter, $\lambda_L$and λ_S, andis selected empirically from a range of values that gives the best image quality. Theselection process for these parameters is lengthy for dynamic imaging method, and methods for automatic selection of regularization parameter can be investigated.
5. A dynamic MRI reconstruction method from partial k-space measurements can be introduced that recovers and inherently separates the information in the dynamic scene. The reconstruction model can be based on a low-rank plus sparse decomposition prior, which can be related to robust principal component analysis.

An algorithm can be proposed to solve the convex optimization problem based on an alternating direction method of multipliers. The method can be validated with numerical phantom simulations and cardiac MRI data against state of the art dynamic MRI reconstruction methods. Results can suggest that using the proposed approach as a means of regularizing the inverse problem remains competitive with state of the art reconstruction techniques. Additionally, the decomposition induced by the reconstruction can be shown to help in the context of motion estimation in dynamic contrast enhanced MRI.

6. Respiratory motion correction remains a challenge in coronary MRI and current techniques, such as navigator gating, suffer from sub-optimal scan efficiency and ease-of-use. To overcome these limitations, an image-based self-navigation technique can be proposed that uses "sub-images" and CS to obtain translational motion correction in 2D. The method can be preliminarily implemented as a 2D technique and tested for feasibility for targeted coronary imaging.
7. A method that combines parallel imaging and CS can be developed to enable faster and/or higher spatial resolution MRI and show its feasibility in a pediatric clinical setting. A pseudorandom k-space under sampling pattern can be incorporated into a 3D gradient-echo sequence; aliasing then has an incoherent noise like pattern rather than the usual coherent fold-over wrapping pattern. This k-space-sampling pattern can be combined with a CS nonlinear reconstruction method that exploits the assumption of sparsity of medical images to permit reconstruction from under sampled k-space data and remove the noise like aliasing. Number of patients on the basis of gender and age can be selected who have been referred for cardiovascular, abdominal and knee MRI. Their problems can be scanned with this 3D gradient-echo sequence at high acceleration factors. Obtained k-space data

can be reconstructed with both a traditional parallel imaging algorithm and the nonlinear method. Both sets of images can be rated for image quality, radiologist preference and delineation of specific structures by at least two radiologists. Wilcoxon and symmetry tests can be performed to test the hypothesis that there is no significant difference in ratings for image quality, preference and delineation of specific structures.

8. Practically, to get better additional diagnostic information and better image quality Positron Emission Tomography (PET) and MRI can be combined along with respiratory motion. In this PET-MR strategy, information from one imaging modalities will be help full in other modality.
9. In this dissertation, the focus was to improve the quality of compressively sampled dynamic MR image in the presence of respiratory motion. However, the time required to get final results must be improved for practical application. For this propose, the stopping criteria must be selected carefully to avoid

   unnecessary iteration for the reconstruction of MR images. Computation time can also be reduced using optimized coding and parallel programming concepts along with GPU to make it feasible for clinical applications.

REFERENCES

1 Pruessmann, K.P., Weiger, M., Scheidegger, M.B., and Boesiger, P.: 'SENSE: sensitivity encoding for fast MRI', Magnetic resonance in medicine, 1999, 42, (5), pp. 952-962

2 Candès, E.J., Romberg, J., and Tao, T.: 'Robust uncertainty principles: Exact signal reconstruction from highly incomplete frequency information', IEEE Transactions on information theory, 2006, 52, (2), pp. 489-509

3 Donoho, D.L.: 'Compressed sensing', IEEE Transactions on information theory, 2006, 52, (4), pp. 1289-1306

4 Lustig, M., Donoho, D., and Pauly, J.M.: 'Sparse MRI: The application of compressed sensing for rapid MR imaging', Magnetic resonance in medicine, 2007, 58, (6), pp. 1182-1195

5 Lustig, M., Donoho, D.L., Santos, J.M., and Pauly, J.M.: 'Compressed sensing MRI', IEEE signal processing magazine, 2008, 25, (2), pp. 72-82

6 Haldar, J.P., Hernando, D., and Liang, Z.-P.: 'Compressed-sensing MRI with random encoding', IEEE transactions on Medical Imaging, 2011, 30, (4), pp. 893-903

7 Haacke, E.M., Brown, R.W., Thompson, M.R., and Venkatesan, R.: 'Magnetic resonance imaging: physical principles and sequence design' (Wiley-Liss New York:, 1999. 1999)

8 Blümich, B.: 'PT Callaghan. Principles of nuclear magnetic resonance microscopy. Oxford University Press, Oxford, 1993, 492 pp,£ 25. ISBN 0 198 53997 5', Magnetic Resonance in Chemistry, 1995, 33, (4), pp. 322-322

9 Liang, Z.-P., and Lauterbur, P.C.: 'Principles of magnetic resonance imaging: a signal processing perspective' (SPIE Optical Engineering Press, 2000. 2000)

10 McRobbie, D.W., Moore, E.A., Graves, M.J., and Prince, M.R.: 'MRI: Prom Picture to Proton', in Editor (Ed.)^(Eds.): 'Book MRI: Prom Picture to Proton' (UK, Cambridge: Cambridge University Press. Pg, 2006, edn.), pp.

11 Cooley, J.W., and Tukey, J.W.: 'An algorithm for the machine calculation of complex Fourier series', Mathematics of computation, 1965, 19, (90), pp. 297-301

12 Omer, H., and Dickinson, R.: 'Regularization in parallel MR image reconstruction', Concepts in Magnetic Resonance Part A, 2011, 38, (2), pp. 52-60

13 Lima Da Cruz, G.J.: 'Advanced motion corrected reconstruction techniques for magnetic resonance imaging', King's College London, 2016

14 Hestenes, M.R., and Stiefel, E.: 'Methods of conjugate gradients for solving linear systems' (NBS Washington, DC, 1952. 1952)

15 Bruckstein, A.M., Donoho, D.L., and Elad, M.: 'From sparse solutions of systems of equations to sparse modeling of signals and images', SIAM review, 2009, 51, (1), pp. 34-81

16 Candes, E.J., Romberg, J.K., and Tao, T.: 'Stable signal recovery from incomplete and inaccurate measurements', Communications on Pure and Applied Mathematics: A Journal Issued by the Courant Institute of Mathematical Sciences, 2006, 59, (8), pp. 1207-1223

17 Bach, F., Jenatton, R., Mairal, J., and Obozinski, G.: 'Optimization with sparsity-inducing penalties', Foundations and Trends® in Machine Learning, 2012, 4, (1), pp. 1-106

18 Youla, D.C., and Webb, H.: ‘Image Restoration by the Method of Convex Projections: Part 1 Theory’, IEEE transactions on medical imaging, 1982, 1, (2), pp. 81-94
19 Yin, W., Osher, S., Goldfarb, D., and Darbon, J.: ‘Bregman iterative algorithms for \ell_1-minimization with applications to compressed sensing’, SIAM Journal on Imaging sciences, 2008, 1, (1), pp. 143-168
20 Dai, Y.-H., and Yuan, Y.: ‘A nonlinear conjugate gradient method with a strong global convergence property’, SIAM Journal on optimization, 1999, 10, (1), pp. 177-182
21 Pruessmann, K.P., Weiger, M., Börnert, P., and Boesiger, P.: ‘Advances in sensitivity encoding with arbitrary k-space trajectories’, Magnetic resonance in medicine, 2001, 46, (4), pp. 638-651
22 McKenzie, C.A., Yeh, E.N., Ohliger, M.A., Price, M.D., and Sodickson, D.K.: ‘Self-calibrating parallel imaging with automatic coil sensitivity extraction’, Magnetic Resonance in Medicine, 2002, 47, (3), pp. 529-538
23 Walsh, D.O., Gmitro, A.F., and Marcellin, M.W.: ‘Adaptive reconstruction of phased array MR imagery’, Magnetic Resonance in Medicine, 2000, 43, (5), pp. 682-690
24 Sodickson, D.K., and Manning, W.J.: ‘Simultaneous acquisition of spatial harmonics (SMASH): fast imaging with radiofrequency coil arrays’, Magnetic resonance in medicine, 1997, 38, (4), pp. 591-603
25 Griswold, M.A., Jakob, P.M., Heidemann, R.M., Nittka, M., Jellus, V., Wang, J., Kiefer, B., and Haase, A.: ‘Generalized autocalibrating partially parallel acquisitions (GRAPPA)’, Magnetic Resonance in Medicine: An Official Journal of the International Society for Magnetic Resonance in Medicine, 2002, 47, (6), pp. 1202-1210
26 Lustig, M., and Pauly, J.M.: ‘SPIRiT: iterative self-consistent parallel imaging reconstruction from arbitrary k-space’, Magnetic resonance in medicine, 2010, 64, (2), pp. 457-471
27 Candès, E.J.: ‘Compressive sampling’, in Editor (Ed.)^(Eds.): ‘Book Compressive sampling’ (Madrid, Spain, 2006, edn.), pp. 1433-1452
28 Buccigrossi, R.W., and Simoncelli, E.P.: ‘Image compression via joint statistical characterization in the wavelet domain’, IEEE Transactions on Image Processing, 1999, 8, (12), pp. 1688-1701
29 Taubman, D., and Marcellin, M.: ‘JPEG2000 image compression fundamentals, standards and practice: image compression fundamentals, standards and practice’ (Springer Science & Business Media, 2012. 2012)
30 Olshausen, B.A., and Field, D.J.: ‘Sparse coding of sensory inputs’, Current opinion in neurobiology, 2004, 14, (4), pp. 481-487
31 Caballero, J., Price, A.N., Rueckert, D., and Hajnal, J.V.: ‘Dictionary learning and time sparsity for dynamic MR data reconstruction’, IEEE transactions on medical imaging, 2014, 33, (4), pp. 979-994
32 Elad, M., and Aharon, M.: ‘Image denoising via sparse and redundant representations over learned dictionaries’, IEEE Transactions on Image processing, 2006, 15, (12), pp. 3736-3745
33 Carpenter, T.K., Armitage, P.A., Bastin, M.E., and Wardlaw, J.M.: ‘DSC perfusion MRI—quantification and reduction of systematic errors arising in areas of reduced cerebral blood flow’, Magnetic Resonance in Medicine: An Official Journal of the International Society for Magnetic Resonance in Medicine, 2006, 55, (6), pp. 1342-1349

34 Hara, N., Okuizumi, M., Koike, H., Kawaguchi, M., and Bilim, V.: 'Dynamic contrast-enhanced magnetic resonance imaging (DCE-MRI) is a useful modality for the precise detection and staging of early prostate cancer', The Prostate, 2005, 62, (2), pp. 140-147
35 Bae, K.E., Kim, S.Y., Lee, S.S., Kim, K.W., Won, H.J., Shin, Y.M., Kim, P.N., and Lee, M.-G.: 'Assessment of hepatic function with Gd-EOB-DTPA-enhanced hepatic MRI', Digestive Diseases, 2012, 30, (6), pp. 617-622
36 Knopp, M.V., Giesel, F.L., Marcos, H., von Tengg-Kobligk, H., and Choyke, P.: 'Dynamic contrast-enhanced magnetic resonance imaging in oncology', Topics in Magnetic Resonance Imaging, 2001, 12, (4), pp. 301-308
37 Tofts, P.S.: 'T1-weighted DCE imaging concepts: modelling, acquisition and analysis', signal, 2010, 500, (450), pp. 400
38 Chandrasekaran, V., Sanghavi, S., Parrilo, P.A., and Willsky, A.S.: 'Rank-sparsity incoherence for matrix decomposition', SIAM Journal on Optimization, 2011, 21, (2), pp. 572-596
39 Peng, Y., Ganesh, A., Wright, J., Xu, W., and Ma, Y.: 'RASL: Robust alignment by sparse and low-rank decomposition for linearly correlated images', IEEE transactions on pattern analysis and machine intelligence, 2012, 34, (11), pp. 2233-2246
40 Blanchet, G., and Moisan, L.: 'An explicit sharpness index related to global phase coherence', in Editor (Ed.)^(Eds.): 'Book An explicit sharpness index related to global phase coherence' (IEEE, 2012, edn.), pp. 1065-1068
41 Weissler, A.M., Harris, W.S., and Schoenfeld, C.D.: 'Systolic time intervals in heart failure in man', Circulation, 1968, 37, (2), pp. 149-159
42 Jung, B., Föll, D., Böttler, P., Petersen, S., Hennig, J., and Markl, M.: 'Detailed analysis of myocardial motion in volunteers and patients using high-temporal-resolution MR tissue phase mapping', Journal of Magnetic Resonance Imaging: An Official Journal of the International Society for Magnetic Resonance in Medicine, 2006, 24, (5), pp. 1033-1039
43 Petersen, S.E., Jung, B.A., Wiesmann, F., Selvanayagam, J.B., Francis, J.M., Hennig, J., Neubauer, S., and Robson, M.D.: 'Myocardial tissue phase mapping with cine phase-contrast mr imaging: regional wall motion analysis in healthy volunteers', Radiology, 2006, 238, (3), pp. 816-826
44 Petitjean, C., Rougon, N., and Cluzel, P.: 'Assessment of myocardial function: a review of quantification methods and results using tagged MRI', Journal of Cardiovascular Magnetic Resonance, 2005, 7, (2), pp. 501-516
45 Al-Kwifi, O., Stainsby, J., Foltz, W.D., Sussman, M.S., Huang, Y., and Wright, G.A.: 'Characterizing coronary motion and its effect on MR coronary angiography—initial experience', Journal of Magnetic Resonance Imaging: An Official Journal of the International Society for Magnetic Resonance in Medicine, 2006, 24, (4), pp. 842-850
46 Wang, Y., Vidan, E., and Bergman, G.W.: 'Cardiac motion of coronary arteries: variability in the rest period and implications for coronary MR angiography', Radiology, 1999, 213, (3), pp. 751-758
47 Tangcharoen, T., Jahnke, C., Koehler, U., Schnackenburg, B., Klein, C., Fleck, E., and Nagel, E.: 'Impact of heart rate variability in patients with normal sinus rhythm on image quality in coronary magnetic angiography', Journal of Magnetic Resonance

Imaging: An Official Journal of the International Society for Magnetic Resonance in Medicine, 2008, 28, (1), pp. 74-79
48 Lenz, G.W., Haacke, E.M., and White, R.D.: 'Retrospective cardiac gating: a review of technical aspects and future directions', Magnetic resonance imaging, 1989, 7, (5), pp. 445-455
49 Bogren, H., Lantz, B., Miller, R., and Mason, D.: 'Effect of Respiration on Cardiac Motion Determined by Cineangiography: Implications concerning Three-Dimensional Heart Reconstruction Using Computer Tomography', Acta Radiologica. Diagnosis, 1977, 18, (6), pp. 609-620
50 Wang, Y., Riederer, S.J., and Ehman, R.L.: 'Respiratory motion of the heart: kinematics and the implications for the spatial resolution in coronary imaging', Magnetic resonance in medicine, 1995, 33, (5), pp. 713-719
51 McLeish, K., Hill, D.L., Atkinson, D., Blackall, J.M., and Razavi, R.: 'A study of the motion and deformation of the heart due to respiration', IEEE transactions on medical imaging, 2002, 21, (9), pp. 1142-1150
52 Shechter, G., Ozturk, C., Resar, J.R., and McVeigh, E.R.: 'Respiratory motion of the heart from free breathing coronary angiograms', IEEE transactions on medical imaging, 2004, 23, (8), pp. 1046
53 Maniam, S., and Szklaruk, J.: 'Magnetic resonance imaging: Review of imaging techniques and overview of liver imaging', World journal of radiology, 2010, 2, (8), pp. 309
54 Grimm, R.: 'Reconstruction Techniques for Dynamic Radial MRI'
55 Schultz, C.L., Alfidi, R., Nelson, A.D., Kopiwoda, S.Y., and Clampitt, M.E.: 'The effect of motion on two-dimensional Fourier transformation magnetic resonance images', Radiology, 1984, 152, (1), pp. 117-121
56 Axel, L., Summers, R., Kressel, H., and Charles, C.: 'Respiratory effects in two-dimensional Fourier transform MR imaging', Radiology, 1986, 160, (3), pp. 795-801
57 De Troyer, A., and Estenne, M.: 'Coordination between rib cage muscles and diaphragm during quiet breathing in humans', Journal of Applied Physiology, 1984, 57, (3), pp. 899-906
58 Konno, K., and Mead, J.: 'Measurement of the separate volume changes of rib cage and abdomen during breathing', Journal of applied physiology, 1967, 22, (3), pp. 407-422
59 West, J.B.: 'Respiratory physiology: the essentials' (Lippincott Williams & Wilkins, 2012. 2012)
60 Davies, S., Hill, A., Holmes, R., Halliwell, M., and Jackson, P.: 'Ultrasound quantitation of respiratory organ motion in the upper abdomen', The British journal of radiology, 1994, 67, (803), pp. 1096-1102
61 Hugo, G., Vargas, C., Liang, J., Kestin, L., Wong, J.W., and Yan, D.: 'Changes in the respiratory pattern during radiotherapy for cancer in the lung', Radiotherapy and oncology, 2006, 78, (3), pp. 326-331
62 Korin, H.W., Ehman, R.L., Riederer, S.J., Felmlee, J.P., and Grimm, R.C.: 'Respiratory kinematics of the upper abdominal organs: a quantitative study', Magnetic resonance in medicine, 1992, 23, (1), pp. 172-178
63 Seppenwoolde, Y., Shirato, H., Kitamura, K., Shimizu, S., Van Herk, M., Lebesque, J.V., and Miyasaka, K.: 'Precise and real-time measurement of 3D tumor motion in lung due to breathing and heartbeat, measured during radiotherapy',

International Journal of Radiation Oncology* Biology* Physics, 2002, 53, (4), pp. 822-834
64 Brandner, E.D., Wu, A., Chen, H., Heron, D., Kalnicki, S., Komanduri, K., Gerszten, K., Burton, S., Ahmed, I., and Shou, Z.: 'Abdominal organ motion measured using 4D CT', International Journal of Radiation Oncology* Biology* Physics, 2006, 65, (2), pp. 554-560
65 Steiner, R., Bydder, G., Selwyn, A., Deanfield, J., Longmore, D., Klipsten, R., and Firmin, D.: 'Nuclear magnetic resonance imaging of the heart. Current status and future prospects', Heart, 1983, 50, (3), pp. 202-208
66 Paling, M.R., and Brookeman, J.R.: 'Respiration artifacts in MR imaging: reduction by breath holding', Journal of computer assisted tomography, 1986, 10, (6), pp. 1080-1082
67 Rajaraman, S., Rodriguez, J.J., Graff, C., Altbach, M.I., Dragovich, T., Sirlin, C.B., Korn, R.L., and Raghunand, N.: 'Automated registration of sequential breath-hold dynamic contrast-enhanced MR images: a comparison of three techniques', Magnetic resonance imaging, 2011, 29, (5), pp. 668-682
68 Scott, A.D., Keegan, J., and Firmin, D.N.: 'Motion in cardiovascular MR imaging', Radiology, 2009, 250, (2), pp. 331-351
69 Lisanti, C.J., and Douglas, D.B.: 'Effects of breath-hold and cardiac cycle on the MRI appearance of the aorta and inferior vena cava in T2 abdominal imaging', American Journal of Roentgenology, 2009, 192, (5), pp. 1348-1358
70 Ehman, R.L., McNamara, M., Pallack, M., Hricak, H., and Higgins, C.: 'Magnetic resonance imaging with respiratory gating: techniques and advantages', American journal of Roentgenology, 1984, 143, (6), pp. 1175-1182
71 Uribe, S., Muthurangu, V., Boubertakh, R., Schaeffter, T., Razavi, R., Hill, D.L., and Hansen, M.S.: 'Whole-heart cine MRI using real-time respiratory self-gating', Magnetic Resonance in Medicine, 2007, 57, (3), pp. 606-613
72 Ehman, R.L., and Felmlee, J.P.: 'Adaptive technique for high-definition MR imaging of moving structures', Radiology, 1989, 173, (1), pp. 255-263
73 Wang, Y., Rossman, P.J., Grimm, R.C., Riederer, S.J., and Ehman, R.L.: 'Navigator-echo-based real-time respiratory gating and triggering for reduction of respiration effects in three-dimensional coronary MR angiography', Radiology, 1996, 198, (1), pp. 55-60
74 Feng, L., Srichai, M.B., Lim, R.P., Harrison, A., King, W., Adluru, G., Dibella, E.V., Sodickson, D.K., Otazo, R., and Kim, D.: 'Highly accelerated real-time cardiac cine MRI using k–t SPARSE-SENSE', Magnetic resonance in medicine, 2013, 70, (1), pp. 64-74
75 Uecker, M., Zhang, S., Voit, D., Karaus, A., Merboldt, K.D., and Frahm, J.: 'Real-time MRI at a resolution of 20 ms', NMR in Biomedicine, 2010, 23, (8), pp. 986-994
76 Glover, G.H., and Pauly, J.M.: 'Projection reconstruction techniques for reduction of motion effects in MRI', Magnetic resonance in medicine, 1992, 28, (2), pp. 275-289
77 Liao, J.R., Pauly, J.M., Brosnan, T.J., and Pelc, N.J.: 'Reduction of motion artifacts in cine MRI using variable-density spiral trajectories', Magnetic resonance in medicine, 1997, 37, (4), pp. 569-575

78 Larson, A.C., White, R.D., Laub, G., McVeigh, E.R., Li, D., and Simonetti, O.P.: 'Self-gated cardiac cine MRI', Magnetic Resonance in Medicine: An Official Journal of the International Society for Magnetic Resonance in Medicine, 2004, 51, (1), pp. 93-102
79 Henningsson, M., Smink, J., Razavi, R., and Botnar, R.M.: 'Prospective respiratory motion correction for coronary MR angiography using a 2D image navigator', Magnetic resonance in medicine, 2013, 69, (2), pp. 486-494
80 Scott, A.D., Keegan, J., and Firmin, D.N.: 'Beat-to-beat respiratory motion correction with near 100% efficiency: a quantitative assessment using high-resolution coronary artery imaging', Magnetic resonance imaging, 2011, 29, (4), pp. 568-578
81 Doneva, M., Stehning, C., Nehrke, K., and Börnert, P.: 'Improving scan efficiency of respiratory gated imaging using compressed sensing with 3D Cartesian golden angle sampling', in Editor (Ed.)^(Eds.): 'Book Improving scan efficiency of respiratory gated imaging using compressed sensing with 3D Cartesian golden angle sampling' (2011, edn.), pp. 641
82 Ahmed, A.H., Qureshi, I.M., Shah, J.A., and Zaheer, M.: 'Motion correction based reconstruction method for compressively sampled cardiac MR imaging', Magnetic resonance imaging, 2017, 36, pp. 159-166
83 Otazo, R., Kim, D., Axel, L., and Sodickson, D.K.: 'Combination of compressed sensing and parallel imaging with respiratory motion correction for highly-accelerated cardiac perfusion MRI', Journal of Cardiovascular Magnetic Resonance, 2011, 13, (1), pp. O98
84 Usman, M., Atkinson, D., Odille, F., Kolbitsch, C., Vaillant, G., Schaeffter, T., Batchelor, P.G., and Prieto, C.: 'Motion corrected compressed sensing for free-breathing dynamic cardiac MRI', Magnetic resonance in medicine, 2013, 70, (2), pp. 504-516
85 Chen, Y., Lee, G.R., Wright, K.L., Griswold, M.A., Seiberlich, N., and Gulani, V.: '3D High spatiotemporal resolution quantitative liver perfusion imaging using a stack-of-spirals acquisition and through-time non-cartesian GRAPPA acceleration', in Editor (Ed.)^(Eds.): 'Book 3D High spatiotemporal resolution quantitative liver perfusion imaging using a stack-of-spirals acquisition and through-time non-cartesian GRAPPA acceleration' (2013, edn.), pp. 0601
86 Sullivan, G.J., and Wiegand, T.: 'Video compression-from concepts to the H. 264/AVC standard', Proceedings of the IEEE, 2005, 93, (1), pp. 18-31
87 Wiegand, T., Sullivan, G.J., Bjontegaard, G., and Luthra, A.: 'Overview of the H. 264/AVC video coding standard', IEEE Transactions on circuits and systems for video technology, 2003, 13, (7), pp. 560-576
88 Barjatya, A.: 'Block matching algorithms for motion estimation', IEEE Transactions Evolution Computation, 2004, 8, (3), pp. 225-239
89 Asif, M.S., Hamilton, L., Brummer, M., and Romberg, J.: 'Motion-adaptive spatio-temporal regularization for accelerated dynamic MRI', Magnetic Resonance in Medicine, 2013, 70, (3), pp. 800-812
90 Otazo, R., Candès, E., and Sodickson, D.K.: 'Low-rank plus sparse matrix decomposition for accelerated dynamic MRI with separation of background and dynamic components', Magnetic Resonance in Medicine, 2015, 73, (3), pp. 1125-1136
91 Gao, H., Rapacchi, S., Wang, D., Moriarty, J., Meehan, C., Sayre, J., Laub, G., Finn, P., and Hu, P.: 'Compressed sensing using prior rank, intensity and sparsity model (PRISM): applications in cardiac cine MRI', in Editor (Ed.)^(Eds.): 'Book Compressed

sensing using prior rank, intensity and sparsity model (PRISM): applications in cardiac cine MRI' (2012, edn.), pp. 2242
92 Cui, Z., Zhang, H., and Lu, W.: 'An improved smoothed l0-norm algorithm based on multiparameter approximation function', in Editor (Ed.)^(Eds.): 'Book An improved smoothed l0-norm algorithm based on multiparameter approximation function' (IEEE, 2010, edn.), pp. 942-945
93 Shah, J., Qureshi, I., Deng, Y., and Kadir, K.: 'Reconstruction of Sparse Signals and Compressively Sampled Images Based on Smooth l1-Norm Approximation', Journal of Signal Processing Systems, 2016, pp. 1-12
94 Wang, W., and Wang, Q.: 'Approximated function based spectral gradient algorithm for sparse signal recovery', Statistics, Optimization & Information Computing, 2014, 2, (1), pp. 10-20
95 Wissmann, L., Santelli, C., Segars, W.P., and Kozerke, S.: 'MRXCAT: Realistic numerical phantoms for cardiovascular magnetic resonance', Journal of Cardiovascular Magnetic Resonance, 2014, 16, (1), pp. 63
96 Wang, Z., Bovik, A.C., Sheikh, H.R., and Simoncelli, E.P.: 'Image quality assessment: from error visibility to structural similarity', IEEE transactions on image processing, 2004, 13, (4), pp. 600-612
97 Moratal, D., Valles-Luch, A., Martí-Bonmatí, L., and Brummer, M.E.: 'k-Space tutorial: an MRI educational tool for a better understanding of k-space', Biomedical imaging and intervention journal, 2008, 4, (1)
98 Chang, T.-C., He, L., and Fang, T.: 'MR image reconstruction from sparse radial samples using Bregman iteration', in Editor (Ed.)^(Eds.): 'Book MR image reconstruction from sparse radial samples using Bregman iteration' (2006, edn.), pp. 482
99 Beck, A., and Teboulle, M.: 'A fast iterative shrinkage-thresholding algorithm for linear inverse problems', SIAM journal on imaging sciences, 2009, 2, (1), pp. 183-202
100 Zibulevsky, M., and Elad, M.: 'L1-L2 optimization in signal and image processing', IEEE Signal Processing Magazine, 2010, 27, (3), pp. 76-88
101 Elad, M., Matalon, B., Shtok, J., and Zibulevsky, M.: 'A wide-angle view at iterated shrinkage algorithms', in Editor (Ed.)^(Eds.): 'Book A wide-angle view at iterated shrinkage algorithms' (International Society for Optics and Photonics, 2007, edn.), pp. 670102-670102-670119
102 Chang, S.G., Yu, B., and Vetterli, M.: 'Image denoising via lossy compression and wavelet thresholding', in Editor (Ed.)^(Eds.): 'Book Image denoising via lossy compression and wavelet thresholding' (IEEE, 1997, edn.), pp. 604-607
103 Chang, S.G., Yu, B., and Vetterli, M.: 'Spatially adaptive wavelet thresholding with context modeling for image denoising', IEEE Transactions on image Processing, 2000, 9, (9), pp. 1522-1531
104 Chang, S.G., Yu, B., and Vetterli, M.: 'Adaptive wavelet thresholding for image denoising and compression', IEEE Transactions on image processing, 2000, 9, (9), pp. 1532-1546
105 Shah, J., Qureshi, I., Proano, J., and Deng, Y.: 'Compressively Sampled MR Image Reconstruction Using Hyperbolic Tangent-Based Soft-Thresholding', Applied Magnetic Resonance, 2015, 46, (8), pp. 837-851

106 Shah, J.A., Qureshi, I.M., Omer, H., Khaliq, A.A., and Deng, Y.: 'Compressively sampled magnetic resonance image reconstruction using separable surrogate functional method', Concepts in Magnetic Resonance Part A, 2014, 43, (5), pp. 157-165
107 Mallat, S.G.: 'A theory for multiresolution signal decomposition: the wavelet representation', IEEE transactions on pattern analysis and machine intelligence, 1989, 11, (7), pp. 674-693
108 Westerink, P., Biemond, J., and Boekee, D.: 'An optimal bit allocation algorithm for sub-band coding', in Editor (Ed.)^(Eds.): 'Book An optimal bit allocation algorithm for sub-band coding' (IEEE, 1988, edn.), pp. 757-760
109 Jung, H., Sung, K., Nayak, K.S., Kim, E.Y., and Ye, J.C.: 'k-t FOCUSS: a general compressed sensing framework for high resolution dynamic MRI', Magnetic resonance in medicine, 2009, 61, (1), pp. 103-116
110 Winkelmann, S., Schaeffter, T., Koehler, T., Eggers, H., and Doessel, O.: 'An optimal radial profile order based on the Golden Ratio for time-resolved MRI', IEEE transactions on medical imaging, 2007, 26, (1), pp. 68-76
111 Pang, J., Sharif, B., Fan, Z., Bi, X., Arsanjani, R., Berman, D.S., and Li, D.: 'ECG and navigator-free four-dimensional whole-heart coronary MRA for simultaneous visualization of cardiac anatomy and function', Magnetic resonance in medicine, 2014, 72, (5), pp. 1208-1217
112 Liu, J., Spincemaille, P., Codella, N.C., Nguyen, T.D., Prince, M.R., and Wang, Y.: 'Respiratory and cardiac self-gated free-breathing cardiac CINE imaging with multiecho 3D hybrid radial SSFP acquisition', Magnetic resonance in medicine, 2010, 63, (5), pp. 1230-1237
113 Spincemaille, P., Liu, J., Nguyen, T., Prince, M.R., and Wang, Y.: 'Z intensity-weighted position self-respiratory gating method for free-breathing 3D cardiac CINE imaging', Magnetic resonance imaging, 2011, 29, (6), pp. 861-868
114 Fessler, J.A., and Sutton, B.P.: 'Nonuniform fast Fourier transforms using min-max interpolation', IEEE Transactions on Signal Processing, 2003, 51, (2), pp. 560-574
115 Cai, J.-F., Candès, E.J., and Shen, Z.: 'A singular value thresholding algorithm for matrix completion', SIAM Journal on Optimization, 2010, 20, (4), pp. 1956-1982
116 Daubechies, I., Defrise, M., and De Mol, C.: 'An iterative thresholding algorithm for linear inverse problems with a sparsity constraint', Communications on pure and applied mathematics, 2004, 57, (11), pp. 1413-1457
117 Hansen, M.S., Sørensen, T.S., Arai, A.E., and Kellman, P.: 'Retrospective reconstruction of high temporal resolution cine images from real-time MRI using iterative motion correction', Magnetic resonance in medicine, 2012, 68, (3), pp. 741-750
118 Candes, E.J., Sing-Long, C.A., and Trzasko, J.D.: 'Unbiased risk estimates for singular value thresholding and spectral estimators', IEEE transactions on signal processing, 2013, 61, (19), pp. 4643-4657